DRAFT: SEPTEMBER 22, 2014
Preprint typeset using LaTeX style emulateapj v. 05/12/14

arXiv:1405.5473v2 [astro-ph.GA] 19 Sep 2014

STRONG NEBULAR LINE RATIOS IN THE SPECTRA OF $Z \sim 2-3$ STAR-FORMING GALAXIES: FIRST RESULTS FROM KBSS-MOSFIRE[1]

CHARLES C. STEIDEL[2], GWEN C. RUDIE[2,3,4], ALLISON L. STROM[2], MAX PETTINI[5], NAVEEN A. REDDY[6,11], ALICE E. SHAPLEY[7], RYAN F. TRAINOR[2], DAWN K. ERB[8], MONICA L. TURNER[9], NICHOLAS P. KONIDARIS[2], KRISTIN R. KULAS[7,10], GREGORY MACE[7], KEITH MATTHEWS[2], IAN S. MCLEAN[7]

DRAFT: September 22, 2014

ABSTRACT

We present initial results of a deep near-IR spectroscopic survey covering the 15 fields of the Keck Baryonic Structure Survey (KBSS) using MOSFIRE on the Keck 1 telescope, focusing on a sample of 251 galaxies with redshifts $2.0 < z < 2.6$, star-formation rates $2 \lesssim \mathrm{SFR} \lesssim 200$ $\mathrm{M}_\odot$ yr^{-1}, and stellar masses $8.6 < \log(\mathrm{M}_*/\mathrm{M}_\odot) < 11.4$, with high-quality spectra in both H- and K-band atmospheric windows. We show unambiguously that the locus of $z \sim 2.3$ galaxies in the "BPT" nebular diagnostic diagram exhibits a disjoint, yet similarly tight, relationship between the ratios [NII]λ6585/Hα and [OIII]/Hβ as compared to local galaxies. Using photoionization models, we argue that the offset of the $z \sim 2.3$ locus relative to $z \sim 0$ is explained by a combination of harder ionizing radiation field, higher ionization parameter, and higher N/O at a given O/H than applies to most local galaxies, and that the position of a galaxy along the $z \sim 2.3$ star-forming BPT locus is surprisingly *insensitive* to gas-phase oxygen abundance. The observed nebular emission line ratios are most easily reproduced by models in which the net ionizing radiation field resembles a blackbody with effective temperature $T_{\rm eff} = 50000-60000$ K and N/O close to the solar value at all O/H. We critically assess the applicability of commonly-used strong line indices for estimating gas-phase metallicities, and consider the implications of the small intrinsic scatter in the empirical relationship between excitation-sensitive line indices and M_* (i.e., the "mass-metallicity" relation), at $z \simeq 2.3$.

Subject headings: cosmology: observations — galaxies: evolution — galaxies: high-redshift — galaxies: abundances – galaxies: starburst — galaxies: fundamental parameters

1. INTRODUCTION

In principle, deep near-IR spectroscopy of high-z galaxies offers the possibility of applying the wealth of locally-calibrated and tested rest-frame optical nebular emission line diagnostics to directly probe H II region physics in galaxies as they were forming. In practice, however, this potentially-powerful method– building on well-established techniques developed over the course of several decades for nearby galaxies– has been relatively slow to develop. In spite of substantial observational effort (e.g., Pettini et al. 1998, 2001; Erb et al. 2004; Shapley et al. 2004; Erb et al. 2006c; Kriek et al. 2008; Maiolino et al. 2008; Förster Schreiber et al. 2009; Mannucci et al. 2010; Henry et al. 2013; Cullen et al. 2014; Troncoso et al. 2014; Wuyts et al. 2014), samples of high redshift galaxies for which a reasonably complete set of strong lines has been measured remain very small. Moreover, except for gravitationally-lensed examples (e.g., Teplitz et al. 2000; Hainline et al. 2009; Finkelstein et al. 2009; Jones et al. 2010; Richard et al. 2011; Rigby et al. 2011; Wuyts et al. 2012; Christensen et al. 2012; Jones et al. 2013; Amorín et al. 2014; James et al. 2014), the low S/N of the near-IR spectra has limited both the dynamic range and the significance of observed line ratios for individual objects. The advent of efficient multi-object near-IR spectrographs on 8-10m class telescopes has long promised to revolutionize nebular spectroscopy of high-redshift galaxies by vastly enlarging the sample sizes and making very deep spectroscopy observationally practical.

The suite of nebular emission lines available in the rest-frame optical (i.e., $0.3 \lesssim \lambda \lesssim 1$ μm) includes probes of density ([OII]$\lambda\lambda$3727,3729 and [SII] $\lambda\lambda$6718,6732), electron temperature ([O III]$\lambda\lambda$4960,5008/[O III]λ4364) and ionization state (e.g., [O III]$\lambda\lambda$4960,5008/[O II]$\lambda\lambda$3727,3729) as well as the so-called "strong-line" metallicity indicators, e.g. those based on ([OIII]+[OII])/Hβ ("R23"; Pagel et al. 1979; Kewley & Dopita 2002), [NII]λ6585/Hα ("N2") and ([OIII]λ5008/Hβ)/([NII]λ6585/Hα) ("O3N2"; Pettini & Pagel (2004) [PP04]). In addition, the Baldwin et al. (1981) (see also Veilleux & Osterbrock 1987) diagnostic line ratios ("BPT": [N II]/Hα and [O III]/Hβ) are commonly used to establish the dominant excitation mechanism of nebular emission in galaxies, providing a relatively "clean" separation of galaxies whose spectra are dominated by AGN-ionized gas from those ionized primarily by the UV radiation field

[1] Based on data obtained at the W.M. Keck Observatory, which is operated as a scientific partnership among the California Institute of Technology, the University of California, and NASA, and was made possible by the generous financial support of the W.M. Keck Foundation.

[2] Cahill Center for Astronomy and Astrophysics, California Institute of Technology, 1216 E. California Blvd., MS 249-17, Pasadena, CA 91125, USA
[3] Carnegie Observatories, 813 Santa Barbara Street, Pasadena, CA 91101, USA
[4] Carnegie-Princeton Fellow
[5] Institute of Astronomy, Madingley Road, Cambridge CB3 0HA, UK
[6] Department of Physics and Astronomy, University of California, Riverside, 900 University Avenue, Riverside, CA 92521, USA
[7] University of California, Los Angeles, Department of Physics and Astronomy, 430 Portola Plaza, Los Angeles, CA 90095, USA
[8] Center for Gravitation, Cosmology, and Astrophysics, Department of Physics, University of Wisconsin-Milwaukee, 1900 E. Kenwood Blvd., Milwaukee, WI 53211, USA
[9] Leiden Observatory, Leiden University, PO Box 9513, 2300 RA Leiden, The Netherlands
[10] NASA Postdoctoral Program Fellow, Ames Research Center, MS 211-1, Moffett Field, CA 94035
[11] Alfred P. Sloan Foundation Research Fellow

of young stars (e.g., Kewley et al. 2001; Kauffmann et al. 2003; Brinchmann et al. 2008). Using large samples, primarily drawn from the SDSS spectroscopic database, it has been shown that star-forming galaxies occupy a relatively tight locus in the BPT plane. As the earliest samples of high-redshift galaxies with the relevant measurements became available, however, there were already indications that distant star-forming galaxies occupy a region of the BPT plane distinct from that of the vast majority of star-forming galaxies in the local universe (Shapley et al. 2005a; Erb et al. 2006a; Liu et al. 2008; Brinchmann et al. 2008). If the initial observations were to hold up when confronted with much larger samples, it would suggest that using nebular line ratios to measure metallicity and other physical properties of the high-z H II regions may be more complex than might have been hoped.

It is well-known that various nebular diagnostics using strong optical emission lines in galaxy spectra can differ substantially– the most obvious example is systematic differences of up to ~ 0.77 dex in oxygen abundance for ostensibly the same set of low-redshift galaxies (see e.g. Kewley & Ellison 2008; Maiolino et al. 2008.) The very different abundance scales depend to a large extent on whether the calibration has been done using theoretical models (which tend to infer higher O abundances) or empirically, using sensitive observations of weak electron temperature sensitive emission lines– the so-called "direct", or "T_e" method. The direct method is generally considered to provide more reliable results when available, but has the practical disadvantage that it requires the detection of very weak emission lines, already challenging for nearby galaxies, becoming rapidly more difficult with increasing redshift as the lines become apparently fainter and are redshifted into spectral regions plagued by much higher terrestrial background. It has also been argued that T_e-based metallicities may be biased low due to temperature gradients and/or by the details of the electron energy distribution (e.g., Stasińska 2005; Dopita et al. 2013).

To place the situation for the determination of nebular oxygen abundances in context, at the highest stellar masses, the asymptotic (i.e., maximum) gas-phase metallicity of star-forming galaxies ranges from below solar to nearly 3 times solar (see Kewley & Ellison 2008). Given the problematic differences in metallicity scale among the many locally-calibrated and/or theoretically derived "strong-line" indicators, attempts have been made to implement new calibrations for which all of the various strong-line methods yield consistent metallicities when applied to large samples of local galaxies (Kewley & Ellison 2008; Maiolino et al. 2008). The results have been successful, in the sense that it is possible to force the calibrations to give the same results (to within $\simeq 0.03$ dex) for the same sample of galaxies (Kewley & Ellison 2008), thus providing confidence that one can at least measure *relative* oxygen abundances at $z \simeq 0$. However, even putting aside our ignorance of the "correct" H II region abundance scales at $z \simeq 0$, it is a separate issue as to whether the "renormalization" of the strong-line techniques can (or should) be applied to samples of high redshift galaxies– clearly this is a desirable possibility, but it has not yet been demonstrated. The root of the problem, which is the main topic of this paper, is that measuring line ratios and then applying regression formulae established at $z \simeq 0$ will work only if the physics of high-z H II regions resembles that of local star-forming galaxies. If there are substantive physical differences, blind application of local calibrations will introduce systematics in inferred metallicity; the origins of any systematics are likely to be fundamental to understanding what drives star formation in rapidly-evolving galaxies at high redshifts.

At most redshifts $z > 1$, only a subset of optical emission lines used by the so-called "strong-line" techniques in the local universe are accessible to ground-based spectroscopy due to significant gaps in the near-IR atmospheric transmission as well as the increasingly prohibitive thermal background at observed wavelengths of $\gtrsim 2.3-2.4$ μm. Potentially most-problematic is comparison of metallicities inferred from one set of strong-line indicators for a sample in a particular redshift range, with those based on a different set of lines at a second redshift. In such a case, it would be impossible to distinguish between evolution of gas-phase metallicities and changes (for other physical reasons) in the dependence of the measured line intensity ratios on metallicity.

A better statistical lever-arm, initially independent of the low-redshift calibrations, can be constructed using observations of high redshift galaxies selected in special redshift intervals for which a relatively complete set of the rest-optical nebular lines falls fortuitously within the near-IR atmospheric windows for ground-based spectroscopy. Perhaps the best such interval is $2.0 \lesssim z \lesssim 2.6$ (e.g., Erb et al. 2006c), where Hα, [NII], and [SII] fall in the K band, [OIII] and Hβ fall in H, and [OII] and [NeIII] in J. In large part for this reason, the Keck Baryonic Structure Survey (KBSS; see Rudie et al. 2012; Trainor & Steidel 2012; Rakic et al. 2012) has focused on galaxies in this redshift range over the past several years (e.g., Adelberger et al. 2004; Steidel et al. 2004; Erb et al. 2006a,c,b; Shapley et al. 2005b; Reddy et al. 2008). Figure 1 shows the current KBSS spectroscopic redshift distribution and schematically illustrates the high priority redshift ranges targeted by the current work.

KBSS provides a wealth of multi-wavelength ancillary data as well as a large sample of spectroscopically-identified galaxies (primarily using Keck/LRIS-B) with $1.5 \lesssim z \lesssim 3.5$. In this paper, we present initial results based on new multiplexed near-IR (rest-frame optical) spectroscopy obtained in the KBSS survey regions, focusing on $2.0 \leq z \leq 2.6$, for the reasons outlined above and summarized in Figure 1.

The paper is organized as follows: section 2 describes the new observations and the properties of the initial KBSS-MOSFIRE sample; section 3 compares the locus of relative emission line intensities of $z \sim 2.3$ galaxies with samples of galaxies in the local universe, showing very distinct differences between the two. Section 4 attempts to explain the principal cause of the change in the diagnostics, with the aid of photoionization models. Section 5 briefly examines the extent to which the observed strong emission line ratios (the "BPT" diagram) can be used at high redshift to discriminate between hot young stars and AGN as ionizing sources; Section 6 identifies likely local analogs of the high-redshift sources and compares them to the most extreme galaxies in the high redshift sample, as a means of forecasting what more sensitive observations might yield. Section 7 revisits the relationship between stellar mass and inferred metallicity (the "Mass-Metallicity" relation, or "MZR") at $z \sim 2.3$, and briefly addresses the extent to which the new KBSS-MOSFIRE sample supports the concept of a "fundamental metallicity relation" similar to that observed in the local universe. Finally, section 8 summarizes the main results, and discusses their implications for metal enrichment and star formation in galaxies near the peak of the galaxy formation epoch.

Throughout the paper, we assume a Λ–CDM cosmology

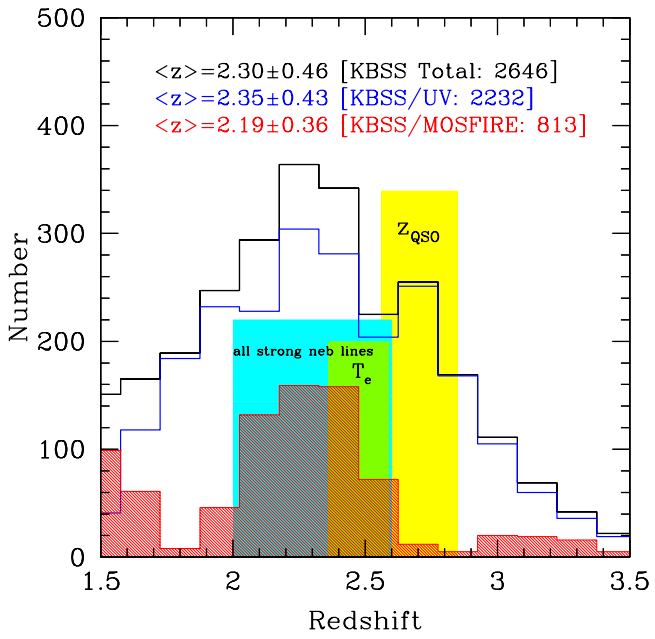

FIG. 1.— Redshift histogram in the KBSS survey regions as of 2014 June. The unshaded black histogram shows the redshift distribution of 2646 spectroscopically confirmed (using MOSFIRE and/or LRIS-B) galaxies in the 15 KBSS survey fields; the blue histogram shows the redshift distribution of the subset with rest-UV spectra from Keck/LRIS-B, the (red) shaded histogram shows the distribution of nebular redshifts obtained with MOSFIRE, and the black unshaded histogram is the KBSS total with spectroscopic redshifts. The cyan-shaded region schematically illustrates the redshift range over which the targeted suite of strong nebular emission lines falls within the ground-based near-IR atmospheric windows ($2 \lesssim z \lesssim 2.6$); the green shading (labeled "T_e") corresponds to the subset of the cyan region over which the electron temperature sensitive [OIII]λ4364 line is accessible in H band ($2.36 \leq z \leq 2.57$; see section 2). The yellow shading shows the redshift range of the very bright background QSOs in the KBSS fields; while these are not directly relevant to the topic of this paper, their lines of sight provide extremely sensitive measurements of H I and metals in the circum-galactic (CGM) and intergalactic medium (IGM) surrounding KBSS survey galaxies (see Rudie et al. 2012; Rakic et al. 2012; Trainor & Steidel 2012; Turner et al. 2014).

with $H_0 = 70$ km s^{-1} Mpc^{-1}, $\Omega_\Lambda = 0.7$, and $\Omega_m = 0.3$, a Chabrier (2003) stellar initial mass function (IMF), and the solar metallicity scale of Asplund et al. (2009), for which $12+\log(O/H) = 8.69$

2. OBSERVATIONS AND DATA

All near-IR spectroscopic observations described in this paper were obtained using the Multi-Object Spectrometer for InfraRed Exploration (MOSFIRE; McLean et al. 2010, 2012), the recently commissioned near-IR imaging spectrometer on the Keck 1 10m telescope at the W.M. Keck Observatory on Mauna Kea. Some of the data were obtained during MOSFIRE commissioning science verification in 2012 May and June, with the remainder obtained during early science observations in 2012 September and October and 2013 March, May, June, and November.

2.1. *Target Selection and Survey Strategy*

Over the course of MOSFIRE commissioning and early science observations, we developed an observing strategy that takes advantage of the unique capabilities of the instrument in order to achieve multiple scientific goals. The combination of the compact KBSS field geometry (typically 7.′5 by 5.′5) with the flexibility of MOSFIRE's electronically re-configurable cryogenic focal plane mask (the "Configurable Slit Unit", or CSU) lends itself to a "tiered" approach to the near-IR survey, combining routine and difficult observations on the same masks. Because most of the KBSS fields are only slightly larger than the $6.'1 \times 6.'1$ MOSFIRE field of view, there is significant spatial overlap of every mask within a given field. By repeatedly observing masks with similar footprint but distinct sets of objects, we ensure that all high priority targets are observed and that the geometrical constraints imposed by slitmasks do not limit the sampling of targets on small angular scales. At the same time, if very deep spectra are required to detect weak emission lines (e.g., auroral [OIII] λ4364, or [NII]λ6585 in galaxies with very low metallicity), the same target is repeated on multiple masks, thereby accumulating much longer total total integration times (more than 10 hours in some cases).

The objects in the parent catalog for each KBSS field were assigned numerical priorities based on multiple criteria: the highest priorities were given to galaxies known from previous spectroscopic observations to lie in narrow redshift range $2.36 \leq z \leq 2.57$ – the range over which the set of strong emission lines (including [S II]$\lambda\lambda$6718, 6732) as well as [OIII]λ4364 are all accessible within the near-IR atmospheric windows (Figure 1). These would be the initial candidates to appear on multiple masks, since (for example) the flux of the T_e-sensitive [OIII]λ4364 line is expected to be $\gtrsim 50$ times smaller than that of [OIII]λ5008. The design of a series of masks in a given field proceeded by keeping the highest priority targets on each, and assigning the rest of the available slit "real estate" to different targets according to their relative numerical priorities. A typical mask included 10-15 such fixed targets, out of a total $\simeq 30-35$ slits.

For the other 20-25 targets on each mask, initial priorities were assigned based on the following criteria, from highest to lowest: (1) those with existing high quality UV spectra and known redshifts $2 \lesssim z \lesssim 2.6$, weighted according to their angular separation from the central QSO sightline (2) those flagged as probable high-stellar-mass targets in the redshift range $1.5 \leq z \leq 2.5$, selected using joint optical/near-IR photometric criteria (3) $\mathcal{R} \leq 25.5$ UV color selected galaxies expected to have redshifts within the optimal $2 \lesssim z \lesssim 2.6$ range (in practice, these are the "BX" and "MD" objects defined by Adelberger et al. (2004); Steidel et al. (2004) and Steidel et al. (2003)) (4) rest-UV color-selected galaxies judged likely to have redshifts $z < 2$ or $z > 2.6$ from their rest-UV colors, but not yet confirmed spectroscopically, and (5) UV color-selected galaxies with $\mathcal{R} > 25.5$ (when the depth of the optical photometry allows). Note that category (2) includes galaxies that satisfy the UV color selection criteria and have red optical/IR colors $(\mathcal{R}-K_s)_{AB} > 2$, as well as those with UV colors redder than those of BX/MD galaxies and $(\mathcal{R}-K_s)_{AB} > 2$. Empirically, we have found that the latter criteria, indicated with the prefix "RK", identify more heavily-reddened galaxies, with relatively large M_* and $1.4 \lesssim z \lesssim 2.5$, that would otherwise not be included in our spectroscopic samples. The "RK" sample and its statistical properties are discussed in more detail by Strom et al (in prep.) The main purpose of including category (2) targets is to improve the sample statistics for galaxies with $\log(M_*/M_\odot) > 10.5$.

Since MOSFIRE mask configurations can be updated easily (and electronically) during an observing run, and the MOSFIRE-DRP (developed by us) produces pipeline-processed 2-D "stacks" in nearly-real-time, the overall efficiency and scientific return of the survey is optimized through

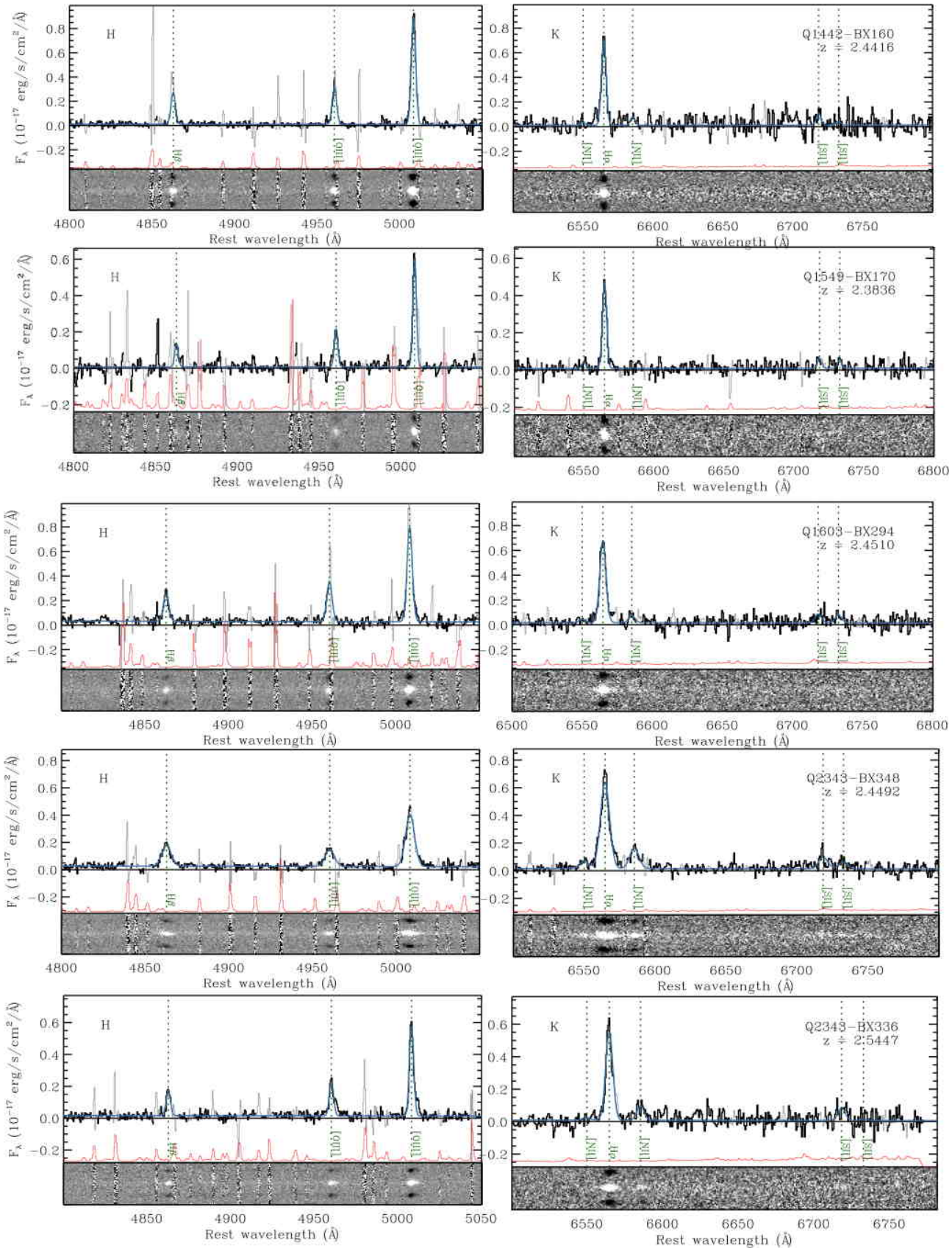

FIG. 2.— Portions of MOSFIRE H-band (left) and K-band (right) spectra for 10 of the KBSS galaxies listed in Tables 1 and 2. The flux-calibrated spectra are presented *unsmoothed*, with their original pixel sampling, with the wavelength scale shifted to each galaxy's rest frame. The best-fit line profiles are superposed (blue), while the 1σ error spectrum (red) is offset, but on the same flux scale, as its corresponding galaxy spectrum. The stacked two-dimensional spectra from which the 1-d spectra were extracted are shown in grayscale, over the same range of rest-wavelength. Each reduced 2-D spectrogram exhibits a positive (central) image and 2 flanking negative images due to the differencing of spatially dithered exposures (see section 2.2.1) that is part of the background subtraction procedure.

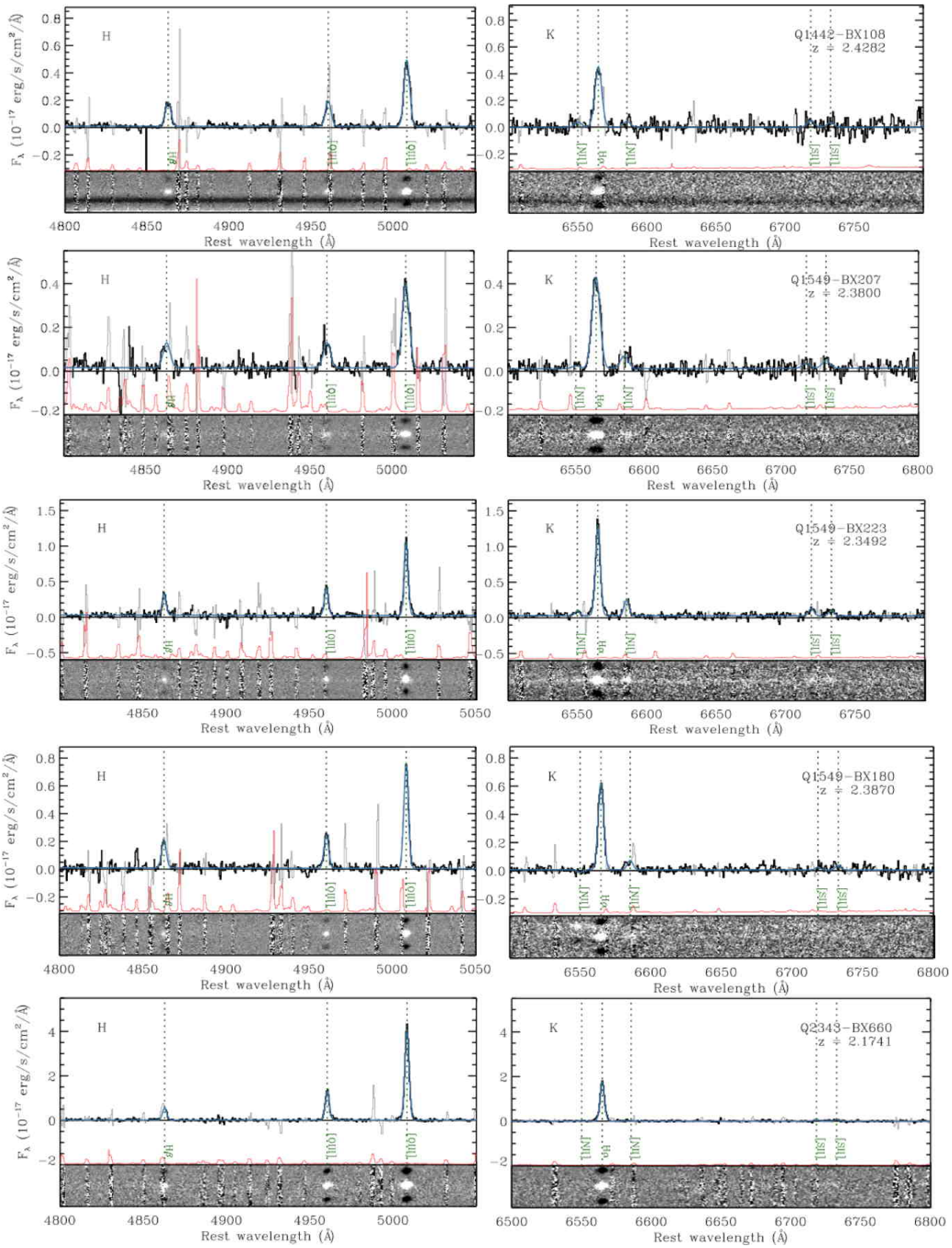

FIG. 2.— (Continued)

quantitative assessment of the data immediately after an observing sequence has completed (generally 20x180s for K band, 30x120s for J or H-band). The results are then used to modify target lists for subsequent masks, performing a running "triage", in which we remove objects with $z < 2$ or $z > 3$ after they have been successfully identified (replacing them with a new set of targets according to the aforementioned priorities), and evaluate the need for additional integration time for targets in the optimal redshift range.

A significant fraction of targets (both within and outside of the optimal redshift range $2.0 \lesssim z \lesssim 2.6$) requires only 1 hour total integration in a given band to produce spectra of sufficient quality to yield precise nebular redshifts, line widths, and strong-line ratios. However, many targets prove more difficult; our unique iterative procedure is used to ensure that the highest priority or most difficult targets receive the longest total integration times (up to $\gtrsim 10$ hours), that galaxies having useful diagnostics in multiple atmospheric bands are observed in multiple bands, and that minimal time is spent observing objects that do not further the scientific goals. Thus, the total integration times for observations presented here span a wide range: $3578\text{s} < \text{t}_{\text{exp}} < 29100\text{s}$ in H-band and $3578\text{s} < \text{t}_{\text{exp}} < 43700\text{s}$ in K-band. The median (average) total integration times for galaxies appearing in Tables 1 and 2 were 8350s (10780s) and 8950s (11520s) in H and K bands, respectively; objects listed in Table 3 have median (average) K-band integration times of 5368s (6810s).

MOSFIRE observations have been acquired in all 15 KBSS survey regions, though at the time the current sample was finalized a few of the fields had been observed to the desired depth in only 1 band, usually H[12].

2.2. *MOSFIRE Instrumental Details*

2.2.1. *Overview*

MOSFIRE obtains spectra of up to 46 objects simultaneously within a 6.′1 x 6.′1 field of view at the f/15 Cassegrain focus of the Keck 1 10m telescope. For H and K band spectroscopic observations, a custom made gold-coated reflection grating with 110.5 lines mm^{-1} is used in orders 4 and 3, respectively, providing wavelength coverage of $1.465-1.799\mu$m (H) and $1.953-2.398\mu$m (K) for slits in the center of the field of view. Although the MOSFIRE CSU can configure up to 46 slits anywhere across the 6.′1 field, in practice masks observed for our program included $28-34$ targets distributed within the central 6.′1 by 3.′0 field of view of the instrument, in order to ensure a large swath of common wavelength coverage for each slit. All masks were designed with slit widths of 0.″7, with lengths in the range 7.″0–23.″0[13]. With 0.″7 slits, MOSFIRE achieves spectral resolution of $R = 3690$ (3620) in the K (H) atmospheric bands, sampled with 2.172 (1.629) Å pix^{-1} in the dispersion direction, and 0.″18 pix^{-1} spatially. The anamorphic magnification of the spectrometer layout is such that a spectral resolution element is sampled with ~ 2.7 pixels at the MOSFIRE detector.

MOSFIRE observations were acquired using a 2-position nod sequence separated by 3.″0 along slits; individual integrations were 180s and 120s for K and H band, respectively, usually obtained in sequences of $\sim$ one hour total integration time. MOSFIRE's Hawaii-2RG detector was read out using Fowler sampling with 16 read pairs, resulting in effective read noise of $\simeq 5.3$ electrons (rms). The decision to use 2-3 minute individual integration times between nods was based on significant experimentation with temporal sampling, readout modes, and dither strategies optimized for faint-object spectroscopy; we have recommended the same strategy to other MOSFIRE users via the MOSFIRE web documentation[14].

By design, the integration times used for individual MOSFIRE exposures are sufficient to yield background-limited performance in spectral regions free of strong OH night sky lines, but are short enough to mitigate the effects of the strong and highly-variable OH emission lines on accurate background subtraction. The dark current of the MOSFIRE detector is negligible (< 0.008 electrons s^{-1} pixel^{-1}) relative to the inter-OH background ($\simeq 0.2-0.3$ electrons s^{-1} pixel^{-1}.) Using the ABAB dither sequence of short individual exposures and combining frames taken in positions A and B separately, quite good background subtraction is obtained by simple subtraction (i.e., A-B or B-A) because they have been obtained quasi-simultaneously; residuals are generally seen only in the OH emission lines, which vary significantly on timescales shorter than the 120s (or 180s) nod time. The differencing has the advantage of removing many systematics that would otherwise cause problems for background subtraction, and requires no fitting or re-sampling of the data. In spite of its Cassegrain location, MOSFIRE is very stable thanks to active flexure compensation that maintains the spectral format fixed with respect to the detector at the level of better than 0.05 pixels (rms) over the course of a typical 1-2 hour exposure sequence.

2.2.2. *Pipeline Data Reduction*

The MOSFIRE data reduction pipeline (DRP; described in more detail below) performs the background subtraction in two stages, of which the first is the simple pairwise subtraction of the interleaved, dis-registered stacks just described. This is followed by fitting a 2-D b-spline model to the background residuals only, using a method similar to that described by Kelson (2003). We have found that the combination yields background residual errors consistent with counting statistics even in the vicinity of strong OH emission lines.

MOSFIRE data were reduced using the publicly-available data reduction pipeline (DRP) developed by the instrument team[15]. The MOSFIRE DRP produces flat-fielded, wavelength calibrated, rectified, and stacked 2-D spectrograms for each slit on a given mask. The 2-D wavelength solutions in H band were obtained from the night sky OH emission lines for each slit, while in K band a combination of night sky and Ne arc lamp spectra was used. The typical wavelength solution residuals were 0.08 Å (K) and 0.06 Å (H), or $\simeq 1.1$ km s^{-1} (rms). All spectra were reduced to vacuum wavelengths and corrected for the heliocentric velocity at the start of each exposure sequence prior to being combined using inverse-variance weighting to form the final 2-D spectra. One-dimensional (1-D) spectra, together with their associated 1σ error vectors, were extracted from the final background-

[12] Experience has shown that H-band observations, in addition to having the best sensitivity per unit integration time, are most likely to yield spectroscopic redshifts for galaxies without previous spectroscopic identifications, since Hα falls in the band for $1.2 \lesssim z \lesssim 1.74$, [O III]$\lambda$5008 for $1.85 \lesssim z \lesssim 2.59$, and [OII]$\lambda\lambda$3727,3729 for $2.92 \lesssim z \lesssim 3.83$.

[13] MOSFIRE slit lengths are quantized, with lengths $(8.0 \times N - 1.0)$ arcsec, where N is the integer number of masking bars comprising the slit.

[14] http://www2.keck.hawaii.edu/inst/mosfire/exposure_recipes.html

[15] See http://code.google.com/p/mosfire/

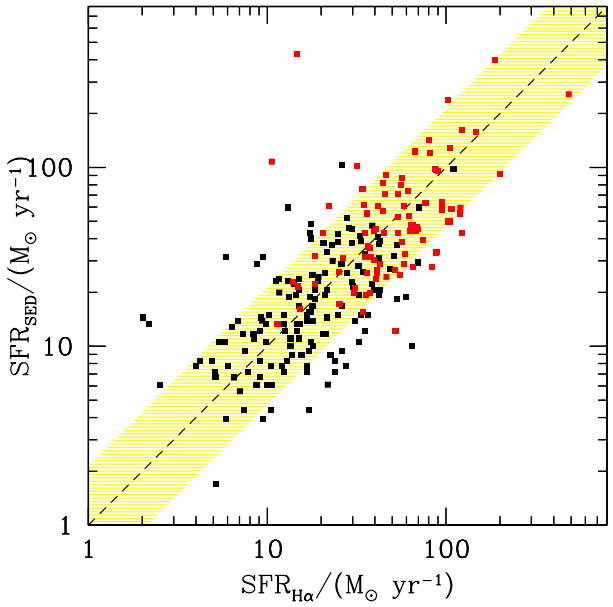

FIG. 3.— Comparison of star formation rates estimated from SED fitting (SFR_{SED}) with those based on the Hα luminosity ($SFR_{H\alpha}$). The dashed line indicates equality between $SFR_{H\alpha}$ and SFR_{SED}. Both estimates assume a Chabrier (2003) IMF, with Calzetti et al. (2000) attenuation for the stellar continuum and nebular extinction as given in equations 6 and 7. Galaxies with $E(B-V)_{cont} > 0.2$ are shown with red points. The median SFR_{sed} and $SFR_{H\alpha}$ agree to within $\sim 5\%$, with a median absolute deviation of $\simeq 0.20$ dex (indicated with the shaded region).

subtracted, rectified spectrograms using "MOSPEC", an IDL-based 1-D spectral analysis tool developed specifically for analysis of MOSFIRE spectra of faint galaxies (see Strom et al., in prep., for a full description.) Figure 2 shows relevant portions of reduced 1-D and 2-D spectra for 10 of the galaxies in the KBSS-MOSFIRE sample discussed below, chosen to span the range of line flux, excitation, and total integration time among the full sample discussed below.

2.2.3. *Extraction and 1-D Spectral Analysis*

In brief, MOSPEC extracts the 1-D spectrum and its associated 1σ error spectrum, applying flux calibration and telluric correction based on wide-slit and narrow-slit observations, respectively, of A0V stars (i.e., Vega analogs). Continuum levels were estimated using the best-fit stellar population synthesis model spectrum after re-normalizing it to match the median observed continuum level; in cases where continuum was not significantly detected, a low-order polynomial fit excluding the positions of known emission lines was used instead. The advantage of the first method is that the contribution of stellar Balmer absorption features coincident with Balmer emission lines is accounted for consistently, since the emission line intensities are measured relative to the continuum level including the suppression by stellar absorption features. The typical effect of including the Balmer absorption on the measurement of the Hβ emission line strength is to increase it by $< 10\%$, and is generally negligible for objects having strong emission lines but very weak continua. Once the continuum level is established, MOSPEC performs a simultaneous fit to a user-specified set of emission lines; outputs include redshift, line flux, line width, and the associated uncertainties. The relative intensities of the [NII]$\lambda\lambda$6549, 6585 and [OIII]$\lambda\lambda$4960, 5008 were held fixed at 1:3. The fitted line profiles within a given observed band were constrained to have the same redshift and velocity width; Gaussian profiles were found to provide good fits to the data except in cases with very high S/N ($\gtrsim 50$), where small departures of line shapes from Gaussian may yield statistically significant residuals relative to the models. In such cases, the line intensities and significance were also estimated from direct integration of the line profiles and error vectors within $\pm 3.0\sigma$ of the line center derived from the Gaussian fit. In most such cases, the best-fit Gaussian line profile and direct integration yield line intensities that agree to better than a few percent. For well-detected objects, the statistical uncertainty on measured redshifts was $\sigma_z \simeq 1-10$ km s^{-1} (depending on line width and S/N), and the agreement in redshift between the independently-fitted H and K-band spectra was typically $\Delta z \lesssim 0.0001$, i.e., $\Delta v \lesssim 10$ km s^{-1} (rms). Similarly, the independently-fitted line widths in the H and K bands agree with one another to within $5-10$ km s^{-1} for typical line widths $\sigma_v \simeq 100$ km s^{-1}.

2.2.4. *Sensitivity*

The sensitivity of the MOSFIRE spectra for detection of relatively narrow nebular emission lines is of course strongly wavelength-dependent even when sky subtraction systematics have been eliminated; the detection sensitivity for a given spectral feature can also be time-dependent, as the intensity of OH emission lines can vary by up to an order of magnitude over the course of an observing night, and a line's velocity with respect to OH emission lines changes with variations in the heliocentric velocity at the time of the observations. MOSFIRE's relatively high spectral resolution, dark inter-line background (0.2-0.3 e$^-$ pix^{-1}), high system throughput ($\simeq 40\%$ on the grating blaze in H and K bands), and fast optics (so that background-limited observations are achieved in short integrations times) have all been optimized by design for spectroscopy of faint objects. Thus, we find that, in spectral regions free of strong OH emission and under typical observing conditions, the limiting (5σ, 1 hour) emission line flux (assuming the median line width of FWHM$\simeq$ 240 km s^{-1} and a typical spatial extraction aperture of 7-9 pixels [$\simeq 1\farcs25-1\farcs62$]) is 3.5×10^{-18} ergs s^{-1} cm^{-2} ($4.5-14\times10^{-18}$ ergs s^{-1} cm^{-2}) in H-band (K-band[16]). The corresponding limiting fluxes for the median total integration times discussed above (~ 2.3 and ~ 2.5 hours in H, K, respectively) are $\simeq 2.6\times10^{-18}$ (H-band) and $\simeq 2.7-8.5\times10^{-18}$ ergs s^{-1} cm^{-2} (K-band). These sensitivities are within $\simeq 10\%$ of those predicted by the MOSFIRE exposure time calculator XTcalc[17] which we developed during commissioning and subsequently made publicly available.

2.2.5. *Spectroscopic Sample Definition*

In this paper, we focus on the subset of KBSS-MOSFIRE galaxies with nebular redshifts $1.95 \lesssim z \lesssim 2.65$ and sufficiently deep K- and H-band spectra to allow significant detections or useful limits for a minimum set of emission lines[18]: Hα λ6564.61, [NII] λ6585.27 (in the K band), and Hβ λ4862.72, [OIII] $\lambda\lambda$4960.30, 5008.24 (in the H-band).

[16] In K-band, the sky continuum level rises monotonically for $\lambda \gtrsim 2.2\mu$m; the brighter limiting flux is appropriate to the red edge of the band, near 2.4μm.

[17] http://www2.keck.hawaii.edu/inst/mosfire/etc.html.

[18] All wavelengths are in vacuum.

A measurement was considered a "detection" when the statistical significance of both [OIII]λ5008 and Hα was $> 5\sigma$, and that of both Hβ and [NII]λ6585 $> 2\sigma$. Undetected Hβ and/or [NII] lines were flagged as limits and assigned a flux upper limit of $+2\sigma$. The 168 galaxies in the targeted redshift range for which all features satisfy the criteria for detection are listed in Table 1.

In practice, the most difficult of the BPT lines to detect is the [NII]λ6585 feature, whose intensity is typically only 10% that of Hα, and can be substantially weaker in the most metal-poor galaxies (e.g., Erb et al. 2006a; see Figure 5). Because of this, the KBSS-MOSFIRE sample contains a significant number of galaxies for which [OIII], Hα, and Hβ are well-detected according to the above criteria, but only upper limits have been measured for [NII]λ6585. These 51 galaxies are listed in Table 2.

For some purposes in what follows below, we have made use of additional KBSS-MOSFIRE galaxies with $1.95 \lesssim z \lesssim 2.65$ and measurements of Hα and [N II] from MOSFIRE K-band observations, for which comparable H-band observations have not yet been obtained. These 32 galaxies are listed separately in Table 3.

2.3. *Stellar Masses and Star Formation Rates*

We assigned stellar masses (M_*) to the KBSS-MOSFIRE galaxies using population synthesis SED fits based on photometry in the optical ($U_nG\mathcal{R}$), near-IR (K_s, J, and, for a subset, WFC3-IR F160W), and *Spitzer*/IRAC (3.6μm and/or 4.5μm, for all but one of the KBSS fields) bands. Prior to performing the SED fits, the near-IR photometry was corrected for the contribution of Hα and [OIII] emission lines to the broadband fluxes using the spectroscopically measured values. The population synthesis method used is described in detail by (e.g.) Shapley et al. (2005b); Erb et al. (2006c); Reddy et al. (2012b); for the current sample we adopted the best-fit stellar masses using the Bruzual & Charlot (2003) models assuming constant SFR and extinction according to Calzetti et al. (2000). As discussed in detail by Shapley et al. (2005b) and Erb et al. (2006c), typical uncertainties in $\log(M_*/M_\odot)$ are estimated to be $\pm 0.1-0.2$ dex. Inferred stellar masses and SFRs throughout this paper assume a Chabrier (2003) IMF for ease of comparison with the majority of other galaxy samples considered. For a Salpeter (1955) IMF, both values would be larger by a factor of 1.8. SFRs were derived from the observed Hα line fluxes after correcting for slit losses and nebular extinction, as described below.

2.3.1. *Slit Loss Corrections*

The typical galaxy in our spectroscopic sample has an intrinsic half-light radius $r_e \simeq 1.6$ kpc, or $\simeq 0\farcs2$ at $z \simeq 2.3$ (Law et al. 2012), so that light losses at the $0\farcs7$ MOSFIRE entrance slits are modulated primarily by the seeing during an observation, which was generally in the range $0\farcs35-0\farcs7$, with a median value of $\simeq 0\farcs6$ (FWHM). For a point source centered in a $0\farcs7$ slit, the fraction of light falling outside the slit is $\simeq 20\%$ for Gaussian seeing with FWHM= $0\farcs6$, assuming that the extraction aperture in the slit direction is sized to include the whole spatial profile. In practice, most of the $z \simeq 2.3$ galaxies are only marginally resolved in $\simeq 0\farcs6$ seeing, with spatial profiles that may be both non-Gaussian and asymmetric, so that slit losses for galaxies are expected to be larger than for true point sources. Wherever possible, two estimates of the slit loss correction (SC) were made for each object; the first, which we call the "2-D profile method", used a Gaussian fit to the observed spatial profile of Hα emission along the slit to calculate the fraction of the total contained within the aperture defined by the slit width of $0\farcs7$ and the extraction aperture, which was adjusted interactively to include the full spatial profile along the slit, with a median value of 8 pixels ($\simeq 1\farcs44$). The 2-D profile method has the advantage that it accounts for the actual size of the galaxy image at the slit, averaged over the full duration of an observation, but has the disadvantage that the true 2-D spatial profile of Hα emission is generally unknown and may not be symmetric as assumed. A second estimate of the slit loss was made for objects having significant continuum flux measured in the spectra ($\sim 70\%$ of the sample). In this case, the slit loss correction SC_{sed} was was obtained using the scale factor between the observed spectroscopic K band continuum level and the median flux density of the best-fit stellar population synthesis model over the same spectral range, measured in the continuum fitting procedure described above. This method of measuring slit losses (essentially, by comparing to external photometry) accounts for both slit losses and (if relevant) any differences in observing conditions between the science observations and the spectrophotometric calibration star, whereas the 2-D profile method alone provides only a relative, "geometric" correction to the observed flux. However, SC_{sed} explicitly assumes that the spatial distribution of line emission (the quantity one is interested in correcting) is the same as that of the near-IR continuum starlight (to which one is fitting the SED models), which need not be the case. In addition, for continuum-faint galaxies, the determination of SC_{sed} can be quite noisy in the face of systematics in the background subtraction on a given slit.

For objects yielding measurements of both "geometric" and "absolute" slit correction estimates, they agree reasonably well, with median values $\langle SC_{2D}\rangle = 1.54 \pm 0.24$ and $\langle SC_{sed}\rangle = 2.11 \pm 0.56$, and $\langle SC_{sed}/SC_{2D}\rangle = 1.33 \pm 0.26$ (errors are the inter-quartile range). Not surprisingly, the slit loss correction factor depends on near-IR luminosity (i.e., stellar mass, to zeroth order), with brighter galaxies requiring larger slit loss corrections due to their generally larger r_e. For example, galaxies with continuum detections and $\log(M_*/M_\odot) < 9.5$ have $\langle SC_{sed}\rangle = 1.71 \pm 0.74$[19], whereas those with $\log(M_*/M_\odot) > 10.5$ have $\langle SC_{sed}\rangle = 2.25 \pm 0.39$; here the error in the low-mass sub-sample is dominated by noise associated with the spectroscopic continuum measurements. The values of SC_{2D} are generally much less noisy than SC_{sed} for continuum-faint objects, since they rely only on the detection of the Hα emission line. Clearly, slit loss corrections remain a significant source of uncertainty in measuring SFR, probably at the $\pm 25\%$ level for individual galaxies. However, we argue below that they are probably small compared to the uncertainties associated with extinction estimates.

For the purposes of this paper, we applied correction factors to the observed Hα fluxes as follows:

$$SC(H\alpha) = 1.6 \; ; \; \log(M_*/M_\odot) < 10.0 \quad (1)$$

$$SC(H\alpha) = 2.0 \; ; \; \log(M_*/M_\odot) \geq 10.0 \quad (2)$$

A relatively bright star ($K_s \lesssim 19$) has been included on all KBSS-MOSFIRE masks since mid-2013 (and on many

[19] Note that only 20 of 43 galaxies at low mass have believable spectroscopic continuum detections, compared to 38 of 47 in the high mass subsample.

masks observed prior to that time); these stars were assigned a normal 0.″7 slit and were reduced in the same way as the galaxies on the mask. Their measured fluxes (i.e., prior to slit loss correction) are typically a factor of $\simeq 1.2-1.4$ smaller than those expected based on the broad-band photometry of the same stars, and thus consistent with the adopted galaxy slit loss corrections. We also compared the observed Hα+[NII]λ6585 fluxes for 18 of the KBSS-MOSFIRE targets (all in the Q1700 field) with measurements made from deep, continuum-subtracted narrow-band Hα observations, discussed previously by Reddy et al. (2010) and Erb et al. (2006b), finding that $f_{\rm NB}/f_{\rm mos} = 2.06 \pm 0.54$ (median and inter-quartile range) where $f_{\rm NB}$ is the photometric line flux from the narrow-band observations and $f_{\rm mos}$ is the observed line flux measured from the MOSFIRE spectra.

2.3.2. *Extinction Corrections*

Extinction corrections were applied to the Hα fluxes using the value of $E(B-V)_{\rm cont}$ from the SED fits, which assumed the Calzetti et al. (2000) starburst attenuation relation (see e.g. Erb et al. 2006b; Reddy et al. 2010); the present KBSS-MOSFIRE sample has $0 \leq E(B-V)_{\rm cont} \leq 0.8$ with a median $E(B-V)_{\rm cont} \simeq 0.2$. It is conventional to assume that nebular emission lines are affected differently by dust compared to the UV stellar continuum, and therefore subject to a different attenuation relation. Calzetti et al. (2000) found a relationship between the reddening of the stars and that of the ionized gas in nearby starburst galaxies,

$$E(B-V)_{\rm neb} = 2.27\ E(B-V)_{\rm cont} \quad (3)$$

where the color excess for the stellar continuum $E(B-V)_{\rm cont}$ can be interpreted with the Calzetti et al. (2000) attenuation relation, but $E(B-V)_{\rm neb}$ is derived from a line-of-sight attenuation relation (e.g., the diffuse Galactic ISM extinction curve of Cardelli et al. 1989) [20]. In the original calibration of equation 3, a standard Galactic ISM reddening curve was used with measurements of H recombination line ratios to derive $E(B-V)_{\rm neb}$; for the Cardelli et al. (1989) Galactic extinction curve, $A(0.656\ \mu{\rm m})_{\rm GAL}/E(B-V) = 2.52$ [the average "SMC bar" extinction curve of Gordon et al. (2003) has $A(0.656\ \mu{\rm m})_{\rm SMC}/E(B-V) = 2.00$] whereas the Calzetti et al. (2000) continuum reddening curve has $A(0.656\ \mu{\rm m})/E(B-V) = 3.33$. Equation 3 implies that, to use a measurement of the color excess $E(B-V)_{\rm cont}$ to estimate the attenuation of the Hα emission line in magnitudes,

$$A(H\alpha) = 2.52 \times 2.27\ E(B-V)_{\rm cont} = 5.72 \times E(B-V)_{\rm cont} \quad (4)$$

assuming Galactic extinction, or

$$A(H\alpha) = 2.00 \times 2.27\ E(B-V)_{\rm cont} = 4.54 \times E(B-V)_{\rm cont} \quad (5)$$

for SMC extinction (Gordon et al. 2003) applied to the nebular emission.

[20] The relation in equation 3 is often misunderstood to mean that the attenuation of Hα emission in magnitudes is higher by a factor of 2.27 than for a continuum photon at the same wavelength; however, it is important to note that equation 3 *assumes* that the two values of the color excess are applied in combination with *different reddening curves*. Although often done, it is incorrect (or at least inconsistent with the original derivation and intended use of equation 3) to use the continuum reddening curve to estimate the attenuation of emission lines. Under the common assumptions that $E(B-V)_{\rm neb} = C\ E(B-V)_{\rm cont}$ (where C is a constant) and that $E(B-V)_{\rm neb}$ can be multiplied with the selective extinction coefficient at 6564Å in the Calzetti et al. (2000) attenuation relation, one obtains the same Hα attenuation as given by proper interpretation of equation 3 with $1.36 \lesssim C \lesssim 1.72$ (see equations 4 and 5.)

However, the relationship between $E(B-V)_{\rm neb}$ and $E(B-V)_{\rm cont}$, and the appropriate extinction curve to be used with either, remains uncertain for high redshift star-forming galaxies. It has been shown that the assumption that $E(B-V)_{\rm neb} = E(B-V)_{\rm cont}$ together with the Calzetti et al. (2000) continuum attenuation relation (i.e., that $A(H\alpha) = 3.33\ E(B-V)_{\rm cont}$) yields SFRs consistent with those measured from stacks of X-ray, mid-IR, and far-IR observations of similarly-selected $z \sim 2$ galaxies (Reddy & Steidel 2004; Erb et al. 2006b; Reddy et al. 2010, 2012a). Other analyses, however, suggest higher nebular extinction (see, e.g., Förster Schreiber et al. 2009; Price et al. 2013), particularly for more metal-rich and/or higher mass galaxies, even after accounting for the extinction curve/color excess interpretation issues mentioned above.

For definiteness, we have assumed the following:

$$A(H\alpha) = 4.54\ E(B-V)_{\rm cont}\ ;\ E(B-V)_{\rm cont} \leq 0.20 \quad (6)$$

$$A(H\alpha) = 5.72\ E(B-V)_{\rm cont}\ ;\ E(B-V)_{\rm cont} > 0.20 \quad (7)$$

equivalent to using an SMC-like extinction curve for galaxies with continuum reddening equal to or below the median value, and Galactic diffuse ISM extinction curve[21] for those above. Using these corrections, we find that the median $\log({\rm SFR}_{H\alpha})$ and median $\log({\rm SFR}_{\rm SED})$ for the KBSS-MOSFIRE sample agree to within 0.02 dex; for individual galaxies, the two SFR estimates have a median absolute deviation $\simeq 0.20$ dex (see Figure 3.). Of course, we do not know that agreement between $\rm SFR_{SED}$ and $\rm SFR_{H\alpha}$ means that either is "correct", but at the very least we can say that they are surprisingly consistent both as an ensemble and on an object-by-object basis.

Observations of Balmer line ratios (e.g., Hα/Hβ) can be used to measure $E(B-V)_{\rm neb}$ directly, and the current KBSS-MOSFIRE sample with $2 \lesssim z \lesssim 2.6$ includes more than 200 galaxies for which both Hα and Hβ line fluxes have S/N$>$ 5; however, greater attention to relative calibration between K-band and H-band spectra is required before the line ratios can be confidently used for extinction measurements, and thus we defer quantitative discussion to future work. Nevertheless, we find a median $I(H\alpha)/I(H\beta) = 3.89 \pm 0.65$, or $E(B-V)_{\rm neb} = 0.29 \pm 0.16$ when evaluated assuming the Cardelli et al. (1989) Galactic extinction curve; the corresponding value of the median continuum color excess for the same set of galaxies is $E(B-V)_{\rm cont} = 0.17$.

After the corrections for slit losses and extinction were applied, Hα fluxes were converted to luminosities assuming a Λ-CDM cosmology with $\Omega_m = 0.3$, $\Omega_\Lambda = 0.7$, and $h = 0.7$ and the Kennicutt (1998) conversion between Hα luminosity and SFR (with adjustment to the Chabrier IMF). In what follows, we use the values of $\rm SFR_{H\alpha}$ listed in Tables 1-3, since they are less strongly covariant with inferred M_* (see, e.g., Reddy et al. 2012b) compared to $\rm SFR_{SED}$; however, none of the results presented in this paper would alter significantly if $\rm SFR_{SED}$ were used instead.

Similarly, it is important to emphasize that, with the exception of the inferred SFR (and thus also sSFR), most of the results presented in this paper do not rely on the absolute calibration of emission line fluxes or their extinction corrections; rather, they depend primarily on the intensity ratios of lines observed simultaneously (i.e., in the same atmospheric band) and are sufficiently close to one another in wavelength that

[21] The LMC average extinction curve is nearly identical to that of the Galaxy over the relevant wavelength range.

differential slit losses or extinction should be negligible.

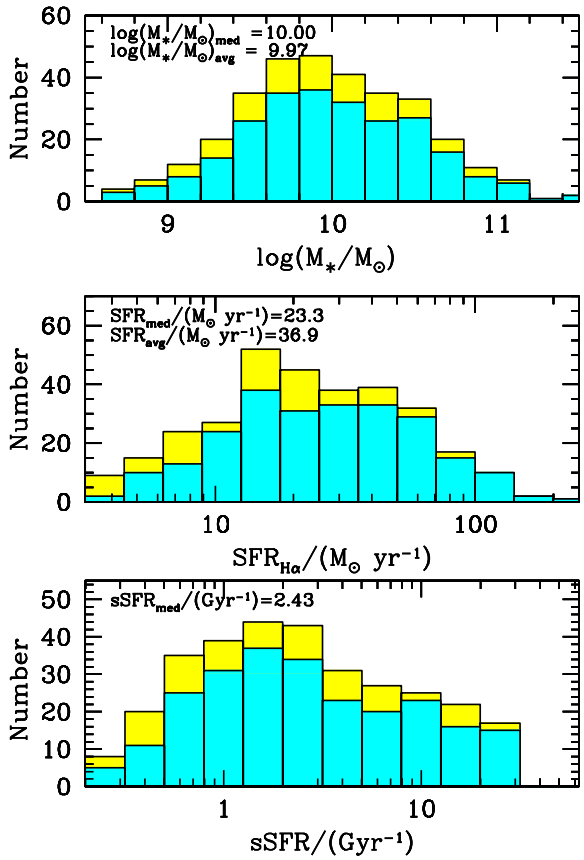

FIG. 4.— Histograms of stellar mass, star formation rate, and specific star formation rate for the KBSS-MOSFIRE sample with $1.95 \leq z \leq 2.60$. The yellow (light) histogram includes a total of 321 galaxies with Hα and stellar mass measurements, independent of whether or not [NII]λ6585, [OIII], or Hβ are detected. The cyan (darker) histogram includes the 242 galaxies appearing in Tables 1-3, excluding 9 objects flagged as AGN [see section 5]. The mean and median values are given on each panel for the parent sample; the subset with N2 and/or [OIII]/Hβ measurements is statistically indistinguishable.

2.4. *Current Sample Statistics*

As summarized in Figure 4, the $z \sim 2.3$ KBSS-MOSFIRE sample includes galaxies with $8.6 \lesssim \log(M_*/M)_\odot \lesssim 11.4$ and $2 \lesssim SFR_{H\alpha} \lesssim 500$ $M_\odot$ yr^{-1}. Specific star formation rates (sSFR$\equiv SFR_{H\alpha}/M_*$) range over more than two orders of magnitude, with a median value of 2.4 Gyr^{-1}, in good agreement with median values estimated when SFR is measured using mid- and far-IR luminosities in addition to the UV (Reddy et al. 2012b,a). Note that Figure 4 compares histograms of M_*, $SFR_{H\alpha}$, and sSFR for the sample of 242 galaxies appearing in Tables 1-3 (excluding 9 flagged as AGN; see section 5) with a "parent" KBSS-MOSFIRE sample of 321 galaxies in the same redshift range with $\geq 5\sigma$ Hα detections, without regard to whether or not additional emission lines have been observed or detected. Thus, galaxies in the Hα sample but not appearing in Tables 1-3 are single-line detections, observed only in K band and of lower overall S/N, usually because their spectra are based on relatively short total integration times obtained for redshift identification.

Of the 251 objects included in Tables 1-3, 189 (75.3%) had prior redshift identifications from optical (rest-frame far-UV) spectra obtained with Keck 1/LRIS-B, 30 (12.0%) had been observed previously with LRIS-B without yielding a redshift identification, and 32 (12.7%) had never before been observed spectroscopically. Among all of the KBSS-MOSFIRE observations so far, when the redshift was known from optical spectroscopy to be in the targeted range $2 \leq z \leq 2.6$, more than 90% yielded successful detections of rest-frame optical nebular lines; when the redshift was not known *a priori*, a similar fraction yielded new spectroscopic redshifts from the MOSFIRE H-band and/or or K-band spectra.

As mentioned above, the selection criteria used for KBSS-MOSFIRE are broader than those of purely rest-UV-color selected samples over the same range of redshifts discussed by (e.g.) Steidel et al. (2004); Erb et al. (2006a,c); Reddy et al. (2010, 2012b); specifically, targets were included whose observed rest-UV and UV/optical colors indicate more heavily reddened galaxies compared to those selected by the "BX" and "MD" criteria. We have also found that the spectroscopic success rate for optically-faint ($\mathcal{R} \gtrsim 25$) galaxies within the UV-color selected samples is higher using near-IR spectroscopy, where most galaxies have strong nebular emission lines, than for optical spectroscopy, where most galaxies have no strong emission lines, and thus identification depends on much weaker absorption lines observed against a faint stellar continuum. Compared to the optical spectroscopic sample of $2 \leq z \leq 2.6$ UV color-selected galaxies in the same 15 KBSS fields (1202 galaxies at the time of this writing), the KBSS-MOSFIRE sample includes a slightly larger fraction of galaxies with $\log(M_*/M_*) > 10.5$ (19.5% vs. 17.4%) and with masses $\log(M_*/M_*) < 9.5$ (19.5% vs. 18.5%). The median SFR_{SED} is 23.3 $M_\odot$ yr^{-1} in the KBSS-MOSFIRE sample, to be compared with 19.5 $M_\odot$ yr^{-1} in the full rest-UV spectroscopic sample. In summary, the sensitivity of MOSFIRE for near-IR spectroscopy has produced a spectroscopic sample that is essentially unbiased with respect to the parent photometric sample, at least in terms of SFR and M_*; this was not the case for the earlier NIRSPEC sample at similar redshifts (Erb et al. 2006a,c).

Realistically, any spectroscopic sample at high redshift, whether based on near-IR or optical spectra, suffers from incompleteness with respect to SFR, which will in turn affect the sample's distribution of M_*. At the low mass end, for example, even with zero extinction our photometric selection criteria limit the galaxies to $G \lesssim 26$, which corresponds to SFR $\gtrsim 1.3$ $M_\odot$ yr^{-1} using the standard conversion of rest-frame 1500 Å luminosity to SFR (e.g., Madau et al. 1998) at $z \sim 2.3$; our detection limit for Hα corresponds to approximately the same SFR for zero extinction. The same practical limits would apply to even the deepest near-IR-selected samples. At the high stellar mass end, greater extinction (nebular and/or UV) may more than compensate for larger overall SFRs, so that the resulting selection function with respect to M_* or SFR becomes potentially complex. The KBSS-MOSFIRE sample is undoubtedly missing high M_* galaxies with very low SFR, which constitute a substantial fraction ($\simeq 40\%$) of galaxies with $\log(M_*/M_\odot) > 11.0$ and $z \sim 2.3$ according to, e.g. Kriek et al. (2008). At the low-mass end, it would be missing most galaxies with uncorrected Hα line fluxes $\lesssim 5 \times 10^{-18}$ ergs s^{-1} cm^{-2}, corresponding to SFR $\lesssim 4 M_\odot$ yr^{-1} at $z \sim 2.3$ after typical correction for slit losses and extinction for galaxies with $\log(M_*/M_\odot) \sim 9$.

2.5. *Targets with Previous Near-IR Spectroscopic Observations*

Of the 251 targets listed in Tables 1-3, 25 galaxies ($\simeq 10\%$) were also included in the NIRSPEC sample of Erb et al. (2006a,c,b), though only 2 of the 25 had been spectroscopically observed in more than one near-IR atmospheric band. In general, the MOSFIRE spectra of the same targets are of much higher S/N and have $\simeq 3$ times higher spectral resolution; however, the nebular redshifts of objects in both samples measurements agree well, with $\langle c(z_{\rm MOS} - z_{\rm NS})/(1+z_{\rm MOS})\rangle = -15 \pm 41$ km s^{-1} (rms). Nine of the current KBSS-MOSFIRE sample were observed by Law et al. (2009), and one by Law et al. (2012), using the OSIRIS integral-field spectrometer and the Keck 2 Laser Guide Star Adaptive Optics facility; two galaxies in the current sample were observed as part of the SINS survey using SINFONI on the VLT (Förster Schreiber et al. 2009). NIRSPEC-based nebular redshifts of 34 objects in the current KBSS-MOSFIRE sample were used to measure galaxy systemic redshifts by Steidel et al. (2010) in their analysis of the kinematics of galaxy-scale outflows at $z \sim 2.3$.

Stellar masses and SFRs (based on SED fitting, including some of the earliest Spitzer/IRAC photometry) have been presented by Shapley et al. 2005b for 17 of the current KBSS-MOSFIRE targets in the Q1700 survey field; many of the current Q1700 galaxies were included in more recent work by Kulas et al. (2013), based on independent measurements of a subset of the current MOSFIRE data in that field.

The last column in each of Tables 1-3 includes the references to earlier work, where relevant.

3. THE "BPT" DIAGRAM AT $\langle Z\rangle = 2.3$

3.1. *The Locus of Star-forming Galaxies in the BPT Plane*

Perhaps the most remarkable aspect of the BPT diagram for local star-forming galaxies is the narrow locus along which most star forming galaxies are found, sometimes referred to as the "HII region abundance sequence" (Dopita et al. 2000) because the left-hand branch can be interpreted as a sequence in overall ionized-gas-phase metallicity. The tightness of the sequence is controlled by the range within a galaxy sample of some combination of the hardness and intensity of the ionizing stellar radiation field and the properties of the ambient ISM being ionized. At $z \simeq 0$, more than 90% of star-forming galaxies fall within ± 0.1 dex of the ridge-line of the sequence (Kewley et al. 2013a); for the SDSS data set used in Figure 5, the scatter in log([OIII]/Hβ) at fixed log([NII]/Hα) is $\simeq 0.11$ dex after accounting for measurement errors.

Figure 5 shows definitively what had already been suggested by the relatively small number of earlier measurements for galaxies at $z \sim 1-2.5$ (Shapley et al. 2005a; Erb et al. 2006a; Liu et al. 2008): the nebular spectra of high redshift star-forming galaxies occupy an almost entirely distinct region of the BPT diagram as compared to local galaxies. It has been shown (e.g., Kewley et al. 2001; Kauffmann et al. 2003) that, for local galaxies, the locus of points along the star-forming branch of the BPT diagram can be fit well by a function

$$\log([\mathrm{OIII}]/\mathrm{H}\beta) = \frac{0.61}{\log([\mathrm{NII}]/\mathrm{H}\alpha) + 0.08} + 1.10 \qquad (8)$$

(e.g.,Kewley et al. 2013a). Fitting the same functional form to the KBSS-MOSFIRE sample in Table 1 yields

$$\log([\mathrm{OIII}]/\mathrm{H}\beta) = \frac{0.67}{\log([\mathrm{NII}]/\mathrm{H}\alpha) - 0.33} + 1.13. \qquad (9)$$

Formally, $\chi^2/\nu = 13.6$ for the best-fit model with respect to the data, or a weighted error of $\simeq 0.15$ dex. For comparison to the BPT locus of local star-forming galaxies, it is of interest to estimate the intrinsic scatter (in the absence of measurement errors) of the locus about the best-fit model. To accomplish this, we assumed that the error bars on each point $\sigma_{{\rm m},i}$ are the true measurement errors but that the total variance for each point $\sigma^2_{{\rm tot},i} = \sigma^2_{{\rm m},i} + \sigma^2_{\rm sc}$, where $\sigma_{\rm sc}$ represents the intrinsic scatter, and is assumed to be a constant (i.e., independent of the measurement errors). The value adopted for $\sigma_{\rm sc}$ is that which yields $\chi^2/\nu \approx 1$; we find that $\sigma_{\rm sc} \approx 0.12$ dex– remarkably similar to the scatter observed in the SDSS galaxy sample relative to the best-fit locus (which generally has negligible measurement errors by comparison). Figure 5 (light shaded region) shows that the vast majority of data points (as well as the points with upper limits on log ([NII]/Hα)) are consistent with a swath in which both log ([NII]/Hα) and log ([OIII]/Hβ) vary by ± 0.12 dex with respect to the best-fit model in equation 9.

Formally, it is difficult to distinguish whether the shift in the locus is primarily due to changes in [OIII]/Hβ, [NII]/Hα, or both. The shift has implications, independent of its physical origin, for the use of strong-line nebular diagnostics beyond the local universe. As shown in Figure 5, the calibrations (or re-calibrations) of the strong line indices imply a one-dimensional curve in the BPT plane, since galaxies of a given value of 12+log(O/H) map uniquely to values of [NII]/Hα and [OIII]/Hβ, with metallicity increasing toward the "right" and "down" along the sequence. The red curves superposed on the $z \simeq 0$ locus in the BPT plane trace the metallicity sequence predicted by recently re-calibrated strong-line indicators that make use of the same line ratios that appear in the BPT diagram, for galaxies with oxygen abundances from 0.2-1.0 times solar ($8.0 \leq 12+\log(\mathrm{O/H}) \leq 8.7$; the solid curve is the best fit regression formula advocated by Maiolino et al. (2008) while the dashed curve is the same locus predicted by the conversion formulae of Kewley & Ellison (2008)[22]. Not surprisingly, both curves follow the ridge line in BPT space traced by the SDSS sample rather accurately– reflecting the fact that essentially the same set of galaxies was used to establish the best-fit joint calibrations for the relevant strong-line indices.

The important point is that according to the local calibrations, overall changes in [O/H] would simply move objects along these curves; it then follows that any galaxy whose BPT parameters do *not* fall along the calibration sequence cannot yield consistent values of 12+log(O/H). Stated simply, Figure 5 shows that there is a problem applying a calibration based on local galaxies to a high-redshift sample, even for those that have been re-normalized to consistent metallicity scales for $z \simeq 0$ (e.g., Maiolino et al. 2008; Kewley & Ellison 2008). In practice this means that the "measured" 12+log(O/H) from strong line ratios will depend systematically on which emission lines are measured. For example, many measurements at $z < 2.6$ rely on the N2 metallicity calibration, since applying it requires observations in only one atmospheric band and the ratio is insensitive to nebular extinction; at $z \gtrsim 3$, on the other hand, estimates are more likely to be based on R23 and other permutations of [OII], [OIII], and Hβ, since [NII] and Hα cannot be observed from the ground. In the latter case, additional issues come into play, e.g., nebu-

[22] Both curves were corrected to reflect oxygen abundances consistent with the N2 abundance scale with the PP04 calibration, for consistency.

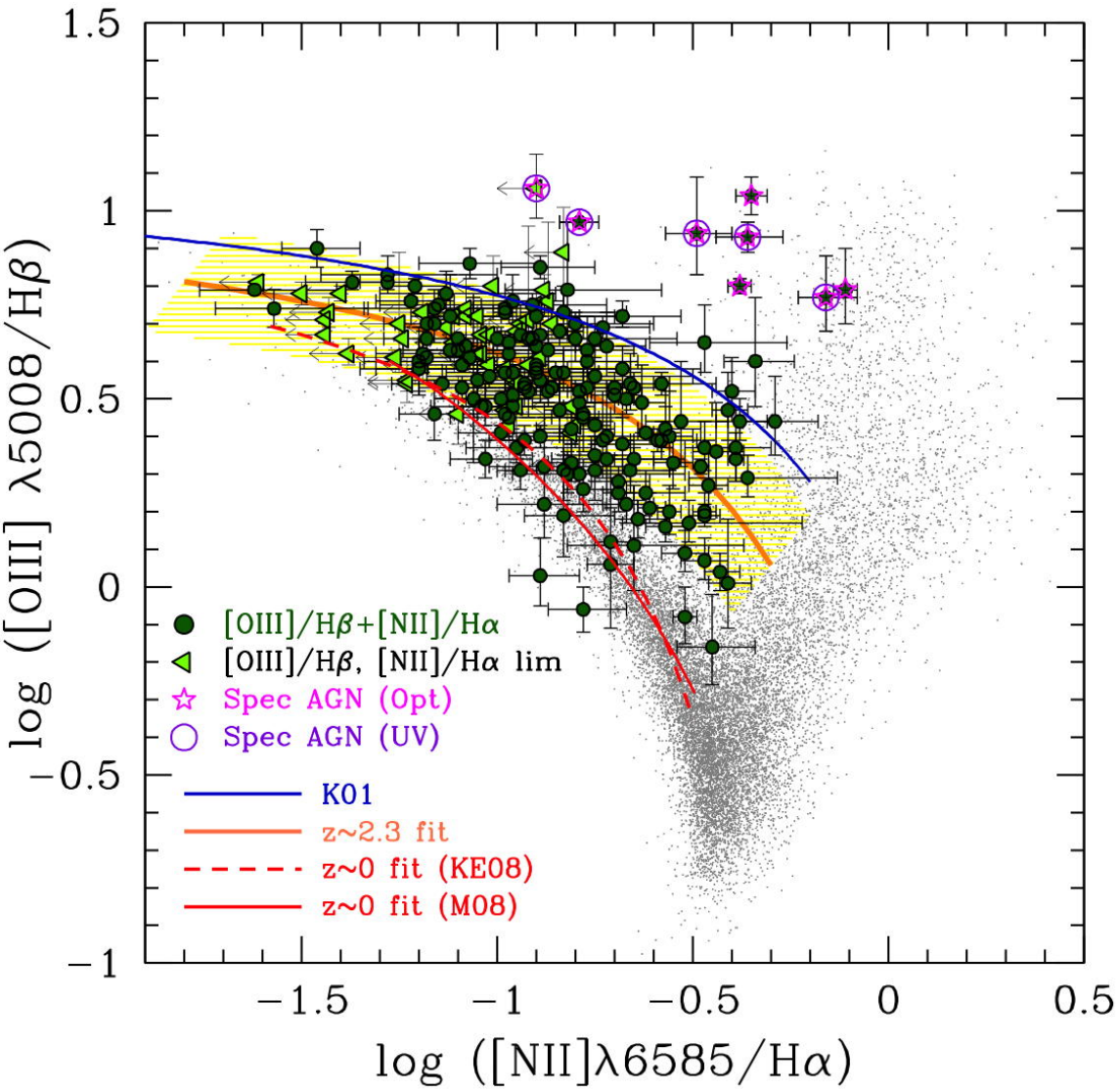

FIG. 5.— "BPT" diagram for 219 objects with $\langle z \rangle = 2.34 \pm 0.16$ in the KBSS-MOSFIRE survey (large points with error bars) in comparison with the SDSS ($z \simeq 0$) sample (e.g., Tremonti et al. 2004; locus of gray points). The 168 objects with measurements in both [NII]/Hα and [OIII]Hβ are indicated with dark green points, while an additional 51 galaxies with [OIII]/Hβ detections and upper limits (2σ) for [NII]/Hα are light triangles with left-pointing arrows. The red curves trace the "metallicity sequence" of SDSS star-forming galaxies, showing the expected location of galaxies in the BPT plane for oxygen abundances of 0.2-1.0 solar – the solid curve is based on the calibration of Maiolino et al. (2008), while the dashed curve represents the same metallicity sequence implied by the strong-line calibration of Kewley & Ellison (2008). Both curves have been adjusted to the N2 metallicity scale of PP04 for consistency. The blue solid curve is the "maximum starburst" model of Kewley et al. (2001). The orange curve is the best-fit BPT sequence for the KBSS-MOSFIRE sample (equation 9) , with the yellow shaded region tracing the inferred intrinsic dispersion of ± 0.1 dex. Eight objects among the 219 have been identified as AGN based on their rest-UV and/or rest-optical spectra (see discussion in section 5); these are indicated with magenta "stars". AGN identified by both rest-UV and rest-optical spectra are indicated by circles surrounding the stars.

lar extinction, accurate relative flux calibrations, and the well-known non-monotonic behavior of the line indices.

Figure 6 illustrates the problem in the context of the $z \sim 2.3$ sample: using locally-established metallicity calibrations leads to systematically different metallicities even for the closely-related N2 and O3N2 methods (both calibrations from PP04), which were calibrated primarily using the "direct" or "T_e" method and the same set of local H II regions. Interestingly, the *scatter* in the locus of inferred metallicities for the $z \sim 2.3$ sample remains small ($\lesssim 0.04$ dex after accounting for the contribution of measurement errors to the observed scatter), suggesting that a re-calibration at high redshift of the strong-line indicators may produce an equally good, albeit different, mapping of metallicity to strong line intensity ratios[23]. The linear regression in Figure 6 serves as an initial estimate of how the conversion might work at $z \sim 2.3$; it will be used in section 7 below.

The question remains whether either of the estimates of $12+\log(\mathrm{O/H})$ is reliable when applied to galaxies at $z \simeq 2.3$; the answer depends strongly on what factor is primarily responsible for the shift in the BPT sequence at $z \sim 2.3$, and

[23] In section 4.5, we revisit the calibrations of the PP04 N2 and O3N2 metallicity relations and their implications for the high-redshift sample.

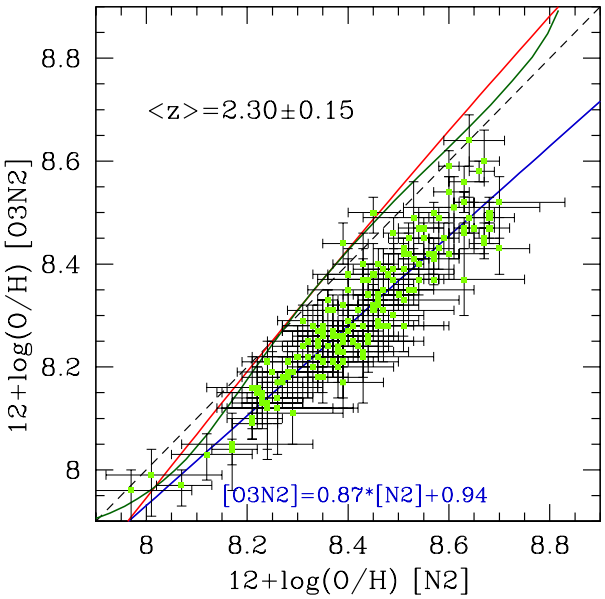

FIG. 6.— Comparison of the inferred oxygen abundance of the $\langle z \rangle = 2.3$ sample based on the PP04 calibrations of the N2 and O3N2 strong-line indices (points with error bars, where the error bars account for measurement errors only and not for uncertainties in the calibrations). The dashed line indicates the expected relation if the two methods were to give the same value of 12+log(O/H). The red and green curves represent the best-fit regression formulae for recent re-calibrations of strong line indicators based on the low redshift sample (Kewley & Ellison 2008 and Maiolino et al. 2008, respectively)– the observed scatter in the low-redshift training sets is $\sim 0.03-0.04$ dex. The systematically lower values of O3N2-based oxygen abundances as compared to those of N2 are evident, consistent with an offset of $\Delta(12+\log(O/H) = 0.13 \pm 0.01$ dex. The blue line is the best linear fit to the relation between the two inferred values at $z = 2.3$. The scatter about this relation, after accounting for measurement errors, is $\simeq 0.04$ dex.

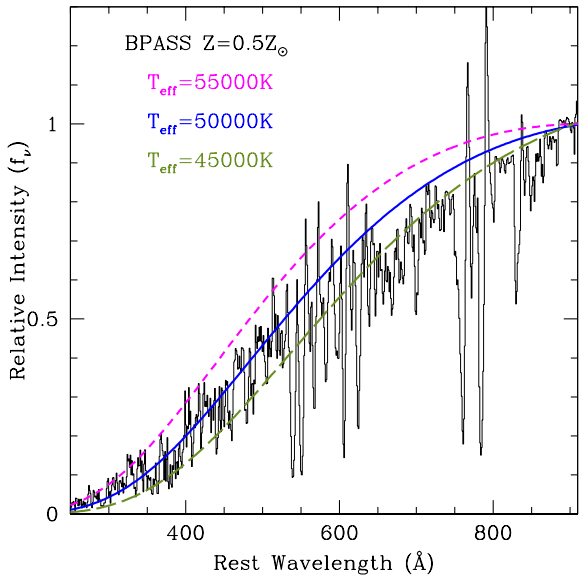

FIG. 7.— Comparison of blackbody spectra with $T_{\rm eff} = 45000-55000$ K and a "Binary Population and Spectral Synthesis" (BPASS) population synthesis model with continuous star formation, $Z = 0.5\ Z_{\odot}$, an age of 10^8 years, and including the effects of binaries (Eldridge & Stanway 2009). The spectra have been normalized to match at rest wavelength of 912 Å (1 Ryd). The $T_{\rm eff} = 50000$ K blackbody (blue solid curve) is a good match to the theoretical spectrum, whose metallicity 12+log(O/H)=8.4 is typical of those inferred for the KBSS-MOSFIRE sample.

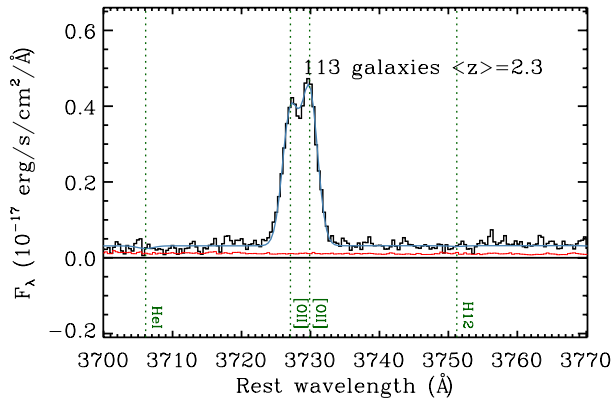

FIG. 8.— Stacked J-band spectrum of 113 KBSS-MOSFIRE $z \sim 2.3$ galaxies showing the resolved [OII] doublet, with $I(3727)/I(3729) = 0.86$. The median value of the ratio for individual galaxies is identical, corresponding to a median electron density $n_{\rm e} \simeq 220$ cm^{-3}.

whether it is reasonable to interpret the locus as an abundance sequence as at low redshift. We address this question in section 4 below.

4. PHYSICAL INTERPRETATION OF THE $Z \sim 2.3$ BPT DIAGRAM

The physical cause of the offset of high-redshift galaxies in the BPT plane has recently been explored by a number of authors through examination of the relatively small number of nearby galaxies occupying similar positions in the BPT diagram (e.g., Liu et al. 2008; Brinchmann et al. 2008), using theoretical models (e.g., Kewley et al. 2001; Erb et al. 2010; Kewley et al. 2013a), or a combination of the two (e.g., Shirazi et al. 2013; Kewley et al. 2013b). Kewley et al. (2013a) in particular have explored in some detail how altering various physical parameters (metallicity, hardness of ionizing radiation field, electron density, prevalence of shocks or AGN versus stellar photoionization) in high redshift HII regions would affect galaxies' position in the BPT diagram. A common conclusion of most of the recent work is that the main driver of the offset is a higher effective ionization parameter, or the dimensionless ratio of the number density of H-ionizing photons to that of H atoms in the H II gas,

$$\Gamma \equiv \frac{n_\gamma}{n_H} \approx \frac{n_\gamma}{n_e} \qquad (10)$$

where n_H is the number density of hydrogen atoms and n_γ is the equivalent density of photons capable of ionizing hydrogen impinging on the face of the gas layer. Γ is analogous to the commonly-used parameter U (or $q = cU$, where c is the speed of light), except that the latter are generally used in the context of a spherical geometry as in the case of an idealized H II region Stromgren sphere surrounding a point-like ionizing source such as a single O-star. Γ is intended to be more general, and to avoid the connotation of a particular geometrical configuration. The effective ionization parameter Γ obviously depends on both the shape and intensity of the radiation field and the physical density in the ionized gas; the former will in turn depend on the physical density of star formation and the ionizing-luminosity-weighted effective temperature mix of the stars producing the ionizing photons. It (Γ) will also depend on the relative three-dimensional distribution of massive stars, ionized gas, and neutral ISM within a galaxy; in some locations, a packet of gas may be ionized by multiple sources impinging from different distances and directions, each of which has been subject to different modu-

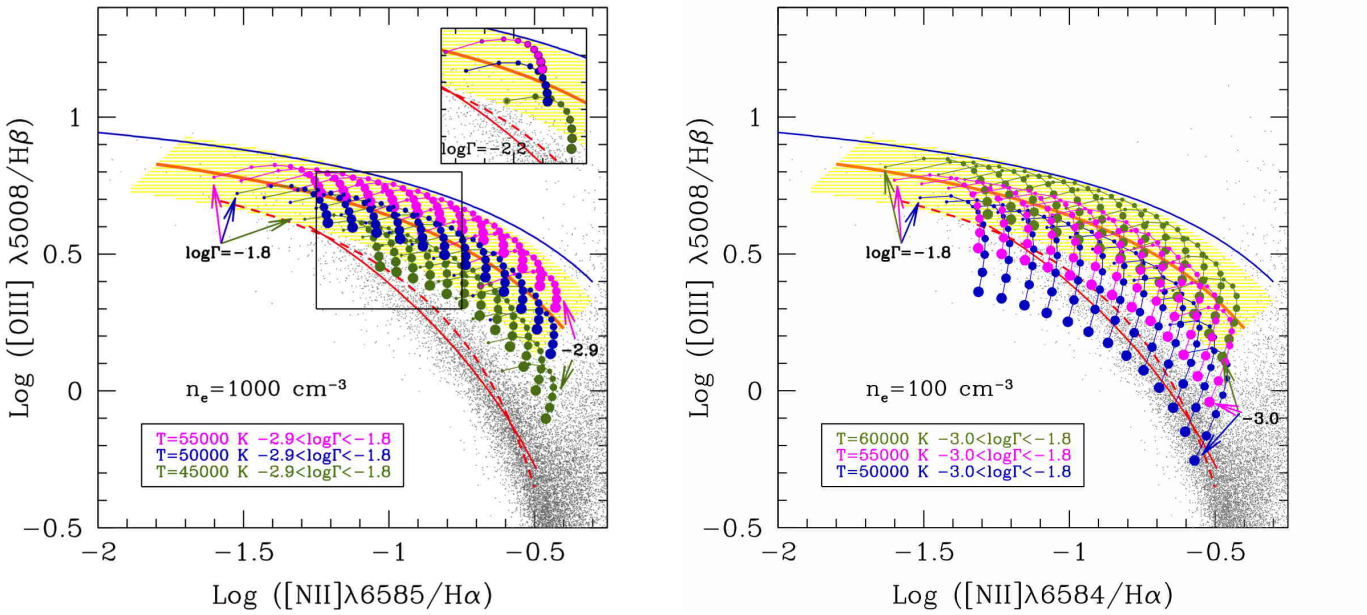

FIG. 9.— (Left) Predicted locus in the BPT diagram for CLOUDY models described in the text; the colors are coded according to the assumed shape (parametrized by $T_{\rm eff}$) of the ionizing radiation field, for ionization parameters in the indicated range and assuming $n_{\rm e} \sim 1000$ cm^{-3}. The shaded region and the solid and dashed curves are the same as in Figure 5. The curves between points, with the same color coding as the points themselves, connect model runs with the same value of logΓ, at intervals of Δlog$\Gamma = 0.1$ dex in between each. For each value of logΓ, the connected points range in metallicity $Z/Z_{\odot} = 0.2-1.0$ in steps of $\Delta(Z/Z_{\odot}) = 0.1$, where the point size scales with $Z/Z_{\odot}$. The inset panel re-plots the region within the black box, but for a single value of the ionization parameter. This view shows the modest dependence on gas-phase metallicity at fixed Γ and $T_{\rm eff}$. (Right) As in the left panel, but for models with $n_e = 100$ cm^{-3}

lations of intensity and shape by intervening material.

4.1. *Photoionization Models*

To gain some intuition, we ran a large grid of model H II regions using CLOUDY[24] in which gas-phase metallicity, ionization parameter, physical density, and the effective temperature ($T_{\rm eff}$) of the stellar ionizing sources were allowed to vary. We initially assumed solar abundance ratios for all elements, but allowed the overall metallicity to range from 0.2 to 1.0 times solar. For simplicity, we began by modeling the UV radiation field shape with a blackbody of temperature $T_{\rm eff} = 45,000\,K$, motivated by the shape of the rest-frame far-UV spectra of $z \sim 3$ LBGs in a very deep spectroscopic survey (Steidel et al 2015, in prep.). We then extracted the predicted intensity ratios of nebular emission lines, as well as the corresponding values of the N2 and O3N2 estimates of 12+ log(O/H), for comparison with the model metallicity. We sought the range of model parameters that could reproduce the high redshift BPT data, including the observed trend in the metallicity indicators (Figure 6). We found that higher effective temperatures for the ionizing radiation field were needed to reproduce the [OIII]/Hβ ratios of the bulk of the $z \sim 2.3$ galaxies, so the grids were expanded to include blackbody energy distributions with $40,000\ {\rm K} \leq {\rm T_{eff}} \leq 60,000$ K.

Note that we have deliberately chosen not to use theoretical stellar models in the CLOUDY runs because of the large uncertainties in the ionizing spectra of O stars and the very high density and complex morphology of star formation within the high-redshift galaxies. Instead, we emphasize that we are interested in constraining the effective shape of the ionizing radiation field and the average ratio of ionizing photons to ISM density within the ionized regions *required to reproduce the observations*. In spite of the relative simplicity of our models, we argue that assuming blackbody ionizing spectra is reasonable. For example, Figure 7 shows that blackbody ionizing spectra represent a reasonable approximation to the shape of the 1-4 Ryd stellar continuum of modern stellar population synthesis models (Eldridge & Stanway 2009.) Similarly, we show in section 8.1 below that the low-redshift BPT sequence can be adequately reproduced assuming a blackbody ionizing spectrum with $T_{\rm eff} \simeq 42000$ K.

For the moment we treat $T_{\rm eff}$ of the ionizing sources independently of the metallicity of the ionized gas producing the observed emission lines. The rationale for doing this, explained in more detail below, is once again that, given the uncertainty in modeling massive star populations as a function of stellar metallicity, we choose to fix the input spectrum in order to better understand the sensitivity of the strong-line indicators to *gas phase* metallicity. Similarly, it seems prudent not to assume that other physical conditions in high-redshift H II regions are similar to local ones until it has been shown to be the case; for this reason, our models include no assumptions about dust, depletion of elements onto dust grains, or non-solar abundance ratios of any elements relative to O.

The range of electron density $n_{\rm e}$ used in the model grids was chosen based on the approximate range inferred from observations of the density-sensitive [OII]λ3727/[OII]λ3729 ratio for a sub-sample of 113 KBSS-MOSFIRE galaxies having appropriate J-band spectra[25] (to be described in more detail in future work). For 90 spectra of individual objects

[24] Calculations were performed with version 13.02 of CLOUDY, last described by Ferland et al. (2013).

[25] While n_e can also be estimated from the ratio [SII]λ6718/[SII]λ6732, these lines are considerably weaker than the [OII] lines for most objects in our sample, limiting the number of objects with ratios determined with sufficient S/N.

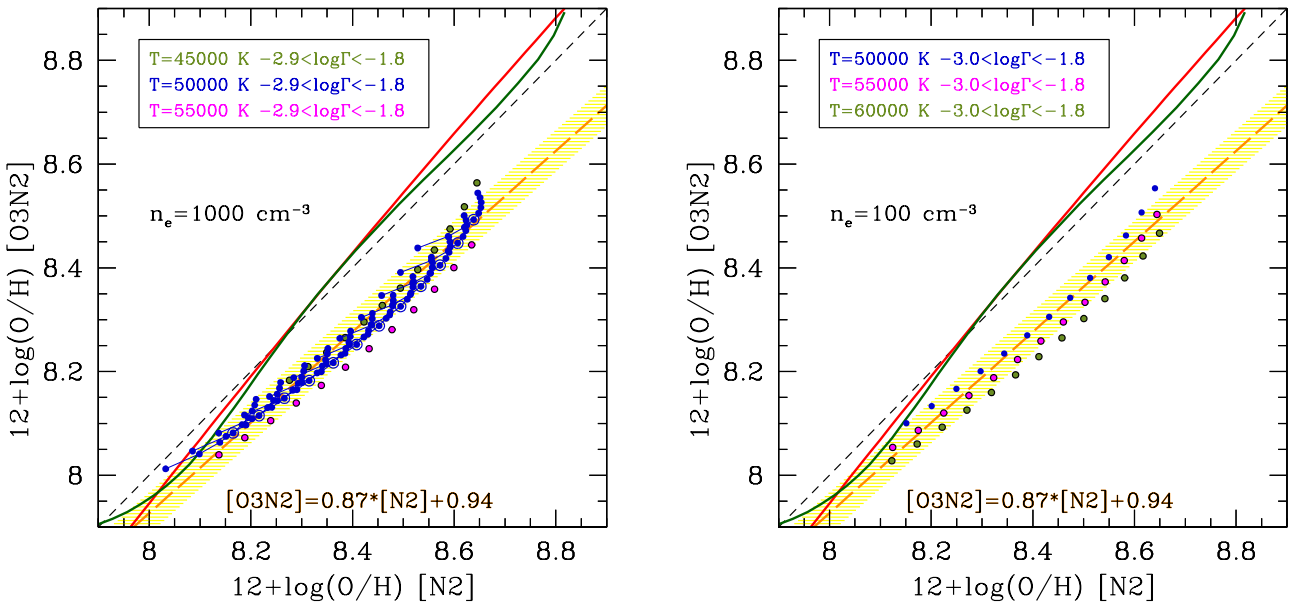

FIG. 10.— (Left) The predicted run of the N2 and O3N2 metallicity estimates for the same set of model parameters as in Figure 9, which should be compared with Figure 6. The yellow shaded region represents the $\simeq 0.04$ dex scatter inferred from the $z \sim 2.3$ observations relative to the best-fit linear relation (orange dashed line). Note that the run of values for these metallicity estimators is actually almost entirely due to a variation in ionization parameter, rather than gas-phase metallicity, and the scatter about the linear relation is dominated by the differences in $T_{\rm eff}$ considered. As in Figure 9a, models with $T_{\rm eff} = 50,000$ K are the best overall fit to the observations. (Right) Same as the left-hand panel, for models with $n_e = 100$ cm^{-3}. Here only the points for $Z/Z_\odot = 0.5$ are plotted, for clarity, to better illustrate the Γ and $T_{\rm eff}$ dependence (at fixed gas-phase metallicity).

with $2.06 < z < 2.62$ and significant detections ($> 5\sigma$) of both members of the [OII]$\lambda\lambda$3726, 3729 doublet, we find $I(3727)/I(3729) = 0.86^{+0.29}_{-0.15}$ (median, with errors corresponding to the 16th and 84th percentile). The corresponding electron densities are $n_{\rm e} \simeq 220^{+380}_{-160}$ cm^{-3} for $10000 < T_{\rm e} < 14000$ K, with the largest values approaching $n_{\rm e} \simeq 2000$ (see section 6.1 below) A stacked spectrum of all 113 J band [OII] spectra also has $I(3726)/I(3729) = 0.86 \pm 0.03$ (Figure 8).

Figure 9 shows model BPT diagrams where the solid curves and shading are as in Figure 5 but the KBSS-MOSFIRE data points have been suppressed for clarity. Two versions of the model are plotted, representing the approximate range of electron density $n_{\rm e}$ among the sample. We focus on the results for $n_e = 1000$ cm^{-3} for the purpose of discussion; the main effect of the lower-density model grid is to require values of $T_{\rm eff}$ higher by ~ 5000 K to reproduce a given value of log([OIII]/Hβ). The left-hand panel of Figure 9 shows that the locus of models with $T_{\rm eff} = 50000$ K and $-2.9 \leq \log\Gamma \leq -1.8$, with metals $Z/Z_\odot = 0.2 - 1.0$, follows very closely the global fit to the KBSS-MOSFIRE BPT data presented above (equation 9); if the $T_{\rm eff} = 45000$ and $T_{\rm eff} = 55000$ grids are included, the correspondence with the full distribution of the $z \sim 2.3$ galaxies is remarkably good. Similarly, Figure 10 shows that the same range of model parameters predicts a relationship between the N2 and O3N2 indices in excellent agreement with the observations (cf. Figure 6.)

Unfortunately, in the context of the models that work well to reproduce the observations, neither N2 nor O3N2 is particularly sensitive to the oxygen abundance in the *ionized gas*, which of course is known *a priori* for the models. In fact, the position of the model locus on the BPT diagram is nearly independent of *gas-phase* oxygen abundance over the modeled range (0.2-1.0 times solar); the position along the BPT sequence is sensitive primarily to ionization parameter Γ, while the maximum value of log([OIII]/Hβ) reached in the BPT diagram is closely related to $T_{\rm eff}$ of the assumed ionizing radiation field. Figure 9a shows that the "metallicity sequence", such as it is, is a very subtle effect, in which a factor of 5 change in gas-phase metallicity moves the locus primarily vertically, but only by $\lesssim \pm 0.05$ dex (and the trend with metallicity is not monotonic). Other strong-line methods would be equally problematic; for example, we find that the same range of model parameters predicts that log(([OIII]+[OII])/Hβ), the ratio upon which the "R23" method depends, is also essentially independent of input gas-phase metallicity (Figure 11). The implication is that, if the models are reasonable, essentially all galaxies in the KBSS-MOSFIRE sample are consistent with having anywhere from 0.2-1.0 times solar nebular oxygen abundance, and that the strong-line ratios are probably not measuring 12+log(O/H) *of the ionized gas* at high redshifts. The implications for strong-line metallicity measurements are discussed in section 4.2 below.

4.2. *Implications for Strong-Line Metallicity Calibrations*

The utility of strong lines for estimating metallicity at high redshift can still be salvaged as long as $T_{\rm eff}$ and/or Γ are monotonically correlated with *stellar* metallicity, likely to closely trace the gas-phase metallicity for such young stars. Such correlations are expected at some level, though they are arguably more model-dependent. It is known that early O-type Magellanic Cloud stars of a given spectral classification have $T_{\rm eff}$ higher by several thousand K compared to their Galactic counterparts (e.g., Massey et al. 2005). A systematic shift from $T_{\rm eff} \simeq 42,000$ K to $T_{\rm eff} = 50,000$ K for the stars dominating the ionizing radiation field could produce a vertical shift in the BPT diagram of $\Delta\left(\log([{\rm OIII}]/{\rm H}\beta)\right) \simeq 0.3$ dex (see, e.g.,

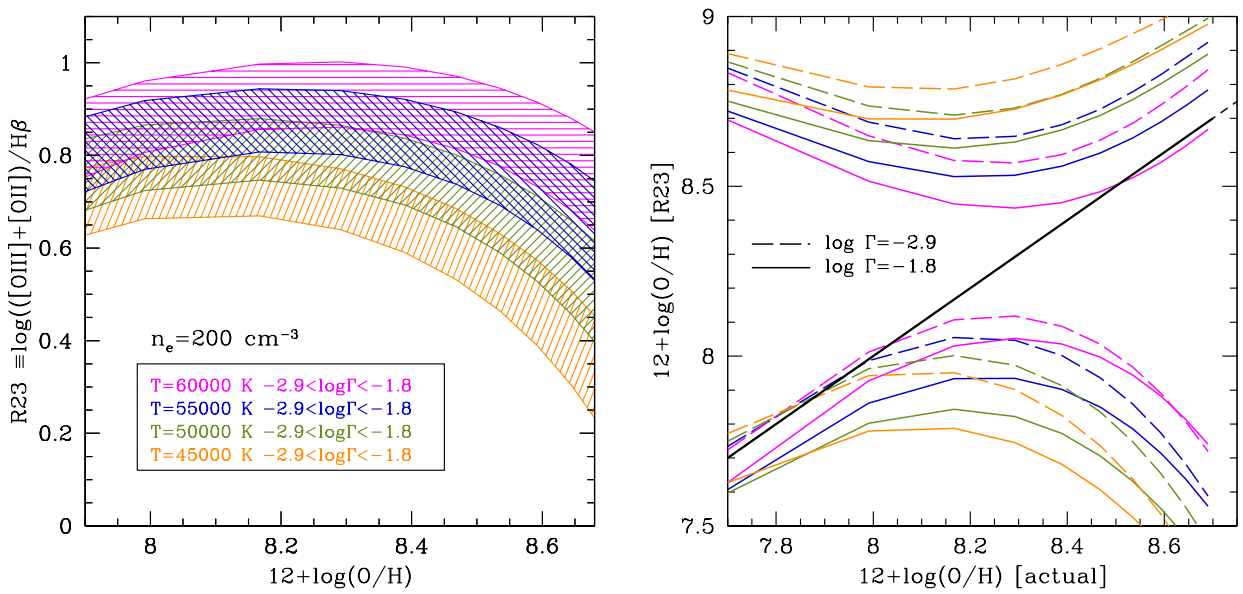

FIG. 11.— (Left) Predictions of the photoionization models for the "R23" parameter as a function of gas-phase metallicity, where the shaded regions in each color show the effects of varying Γ over the range indicated. (Right) R23-based metallicities versus actual gas-phase metallicity predicted by the model grids. Two curves are plotted for each color-coded set of models: the solid curve corresponds to logΓ = −1.8 and the long-dashed curve corresponds to logΓ = −2.9. The two distinct sets of curves for a given $T_{\rm eff}$ reflect the well-known double-valued behavior of R23-based metallicities. The lower set of curves uses the lower branch calibration of McGaugh (1991), while the upper set of curves uses the upper-branch calibration of Kobulnicky & Kewley (2004)– both calibrations use O32 to correct for ionization parameter variations in addition to the R23 parameter. The black solid line indicates equality between the R23-inferred and model values of 12+log(O/H). Note that neither R23 calibration performs well in the $Z\sim0.2-1.0$ $Z_\odot$ range (i.e., 12+log(O/H) = 8.0-8.7.)

Figure 9). In general, stellar metallicity is expected to affect the shape of the ionizing radiation field (Shields & Tinsley 1976) over the critical range $1-4$ Rydberg relevant for ionizing H, He, O, N, and S and producing the observed nebular lines. Harder ionizing UV spectra are expected at lower overall metallicity due to reduced metallic line blanketing in the stellar photospheres; metallicity also strongly affects the prevalence, composition, and structure of massive star stellar winds (e.g., Kudritzki & Puls 2000), which in turn have implications for the degree of stellar rotation. These effects and their possible implications are discussed further in section 4.4 below.

If one admits the possibility that the strong line ratios at high redshifts are driven primarily by factors only indirectly related to gas-phase metallicity, why do they appear to work at low redshift? For the empirically-calibrated O3N2 and N2 relations, for example, the oxygen abundances are rather directly related to galaxy positions along the BPT sequence. Lines of constant O3N2 index are very close to being perpendicular to the low-redshift BPT star-forming locus. However, as we show in Figures 12 and 13 and discuss below, a large part of this behavior may be attributable to variations in N/O, and not O/H.

In this context, it is of interest to ask whether the low redshift BPT sequence can be reproduced using simple photoionization models similar to those applied above to the high redshift data. As shown in Figure 13, the characteristic shape of the low-redshift BPT locus can be reproduced by assuming ionizing sources with $T_{\rm eff}\simeq42000$ K, ionization parameter extending to slightly lower values than those required for the $z\sim2.3$ locus, and metallicities $Z/Z_\odot\simeq0.5-0.7$, substantially lower than usually ascribed to the low-excitation branch of the BPT diagram. The typical metallicities required to match the nearly-vertical portion of the BPT locus depend to a large degree on assumptions built into models– most commonly, the dependence of (N/O) on (O/H). There is ample evidence in local H II regions for strong systematic variation of N/O with O/H when both have been determined by the direct $T_{\rm e}$ method; for example, data compiled by Pilyugin et al. (2012) show that for $12+\log({\rm O/H})\lesssim8.2$, $\log({\rm N/O})\simeq-1.45$ ([N/O]= −0.6), but that for higher oxygen abundance, $\log({\rm N/O})\simeq-1.45+1.8[12+\log({\rm O/H})-8.2]$ (see Figure 12, where we show a third-order polynomial fit to the Pilyugin et al. 2012 data set). Qualitatively similar results have been obtained by many other studies (e.g., Vila Costas & Edmunds 1993; van Zee et al. 1998; Henry & Worthey 1999; Andrews & Martini 2013). The generally-accepted interpretation is that, for low oxygen abundances, H II regions are chemically very young, so that only primary N is present (hence the plateau at $\log({\rm N/O})\simeq-1.5$), while at higher O/H, N/H includes contributions from both primary and secondary N enrichment, with the result that N/O increases more rapidly than O/H. Pilyugin et al. (2012) show that the solar ratio of N/O ($\log({\rm N/O})\simeq-0.86$) is reached when $12+\log({\rm O/H})\simeq8.5$, with N/O becoming super-solar [$\log({\rm N/O})\simeq-0.6$] for solar (O/H) ($12+\log({\rm O/H})=8.69$). Other results suggest more gradual changes in (N/O) with (O/H) (e.g., Pérez-Montero & Contini 2009) or a significantly higher (O/H) at the transition from primary to primary+secondary N (e.g., Andrews & Martini 2013)– suggesting that the precise behavior depends on the nature of the calibration sample and the details of the methods used to measure the abundances. Figure 12 illustrates the substantial range of N/O versus O/H from the recent literature (by no means exhaustive).

Clearly, assumptions concerning the behavior of N/O versus O/H directly affect the predicted locations of models in the BPT plane for a given Γ and $T_{\rm eff}$– for example, lowering

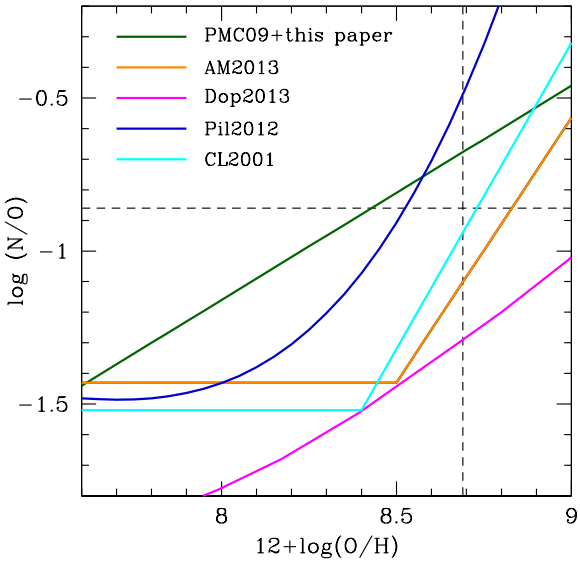

FIG. 12.— Plot showing examples of N/O versus O/H trends and/or assumptions from the recent literature (PMC09=Pérez-Montero & Contini 2009; AM2013 = Andrews & Martini 2013; Dop2013 = Dopita et al. 2013; Pil2012=Pilyugin et al. 2012; CL2001=Charlot & Longhetti 2001.) The solar values of 12+log(O/H) and log(N/O) are indicated with vertical and horizontal dashed lines, respectively. At low oxygen abundance, several of the results show the "plateau" near log(N/O) $\simeq -1.5$, usually attributed to primary N enrichment. The PMC09 result is based on a collection of both extragalactic H II regions and emission line galaxies having T_e-based measurements of N and O abundances; Pil2012 is based on a literature sample of extragalactic H II regions with T_e measurements, AM2013 is based on stacks of SDSS galaxies in bins of M_*, also based on the direct method. CL2001 is a parametrization of data presented by Henry & Worthey (1999), while Dop2013 is a new fit of data presented by van Zee et al. (1998) (note that Dopita et al. (2013) assumes a much lower value of the solar N/H than our assumption of log(N/H) = 7.83).

N/O by 0.2 dex relative to solar at a given O/H essentially shifts the entire sequence by 0.2 dex in N2, i.e., toward the left in the BPT diagram[26] . For the same reason, the dependence of N/O on O/H within samples used for local (empirical) calibration of strong line abundance indicators is "built-in" to any method that makes use of the N2 line ratio– even when no explicit reference is made to N/O. Similarly, the ratio log([NII]λ6585/[OII]λ3729), often used as an indicator of oxygen abundance, is only weakly dependent on O/H when N/O is held fixed, and the mapping of strong line ratios to O/H depends almost entirely on what has been assumed for (N/O) as a function of O/H. The right-hand panel of Figure 13 shows the effects in the BPT plane of the assumption of modest dependence of N/O on O/H,

$$\log(\mathrm{N/O}) = -1.1 + 0.7(X - 8.0) \qquad (11)$$

where $X = 12+\log(\mathrm{O/H})$. This relation, which predicts log(N/O)= –0.62 for solar O/H, is consistent with the local sample of giant extragalactic H II regions and H II galaxies compiled by Pérez-Montero & Contini (2009), as well as with our inferences for the $z \sim 2.3$ KBSS-MOSFIRE sample as discussed below.

Many commonly-used models have encoded the assumptions into the model grids, and in some cases they assume a very rapid increase of N/O over the most relevant range of O/H (e.g., Charlot & Longhetti 2001; Dopita et al. 2013.) The issue of how N/O affects strong line methods of measuring O/H is discussed in detail by Pérez-Montero & Contini (2009); see section 4.5. In spite of the well-established (though not necessarily numerically agreed-upon) trends of N/O as a function of O/H in nearby H II regions and emission line galaxies, similar measurements are not yet available for galaxies at high redshift.

4.3. *Implications for N/O at $z \simeq 2.3$*

An interesting, and potentially important, issue emerging from the KBSS-MOSFIRE data and the photoionization models that reproduce them is the implication for (N/O) in the H II regions of the high redshift galaxies: models that simultaneously produce the observed values of [NII]/Hα and [OIII]/Hβ ratios do not obviously require non-solar (N/O). One possibility would be that the models resemble the data by accident, and that, if the correct N/O dependence on O/H were in the models, a different set of parameters would be required to match the data. However, there also exists evidence that (N/O) may behave differently in the high redshift galaxies compared to local HII regions with the same range in 12+log(O/H). For example, from stacks of SDSS spectra in bins of SFR, Andrews & Martini (2013) found qualitatively similar (N/O) behavior compared to those of Pilyugin et al. (2012) for galaxies with $\log(\mathrm{SFR}/\mathrm{M}_\odot\mathrm{yr}^{-1}) \leq 1$, with a "plateau" in N/O at low O/H, and a rapid increase in N/O above $12+\log(\mathrm{O/H}) \simeq 8.5$ (note that the transition occurs at an oxygen abundance higher by 0.2 dex than Pilyugin et al. (2012) in spite of the fact that both samples were based on direct metallicity measurements– see Figure 12). However, for the sub-samples of galaxies with SFR similar to those of the KBSS-MOSFIRE sample ($\log(\mathrm{SFR}/\mathrm{M}_\odot\mathrm{yr}^{-1}) \gtrsim 1$), N/O does *not* appear to vary with O/H and, moreover, *is consistent with solar* (see their Figure 14).

We have also considered the ratio N2S2$\equiv \log([\mathrm{NII}]\lambda6585/([\mathrm{SII}]\lambda6718+\lambda6732))$, proposed by Pérez-Montero & Contini (2009) as a sensitive measure of (N/O) in H II regions. N2S2 has the advantage of being insensitive to extinction and (in the case of KBSS-MOSFIRE) involves lines measured simultaneously in the K-band spectra. We find that N2S2 $\simeq -0.1 \pm 0.1$, i.e., nearly constant, in both individual spectra for which both [N II] and [S II] are detected, and in spectral stacks formed from subsets of the KBSS-MOSFIRE $z \sim 2.3$ sample. The photoionization models that reproduce the observed N2 and [OIII]/Hβ ratios predict N2S2 in the observed range if $\log(\mathrm{N/O}) \simeq -1.0 \pm 0.1$, independent of gas-phase oxygen abundance for $Z/Z_\odot = 0.1-1$.

Thus, at present we do not see evidence for the low values of log(N/O) ($\simeq -1.5$) that might be expected for very young systems in which only primary N has enriched the ISM, such as damped Lyman α systems (see e.g., Pettini et al. 2008), nor of a strong dependence of (N/O) on (O/H) as expected as secondary N production progresses. Rather, most of the galaxies in our sample appear to have log(N/O) within ~ 0.2 dex of $\log(\mathrm{N/O})_\odot$. Of course, we cannot make strong statements about the galaxies with only upper limits on log([NII]/Hα).

[26] In addition to the behavior of (N/O) vs. (O/H), another common assumption in photoionization models is that gas-phase N and O are depleted by amounts similar to those observed in Galactic H II regions (e.g., Esteban et al. 2004), typically $\simeq 0.07-0.09$ dex for each. In our models, we have made no attempt to account for O or N outside of the gas phase; assuming the Orion nebula depletions would raise the inferred total abundance of oxygen by $\sim 20\%$ relative to those shown in Figure 13.

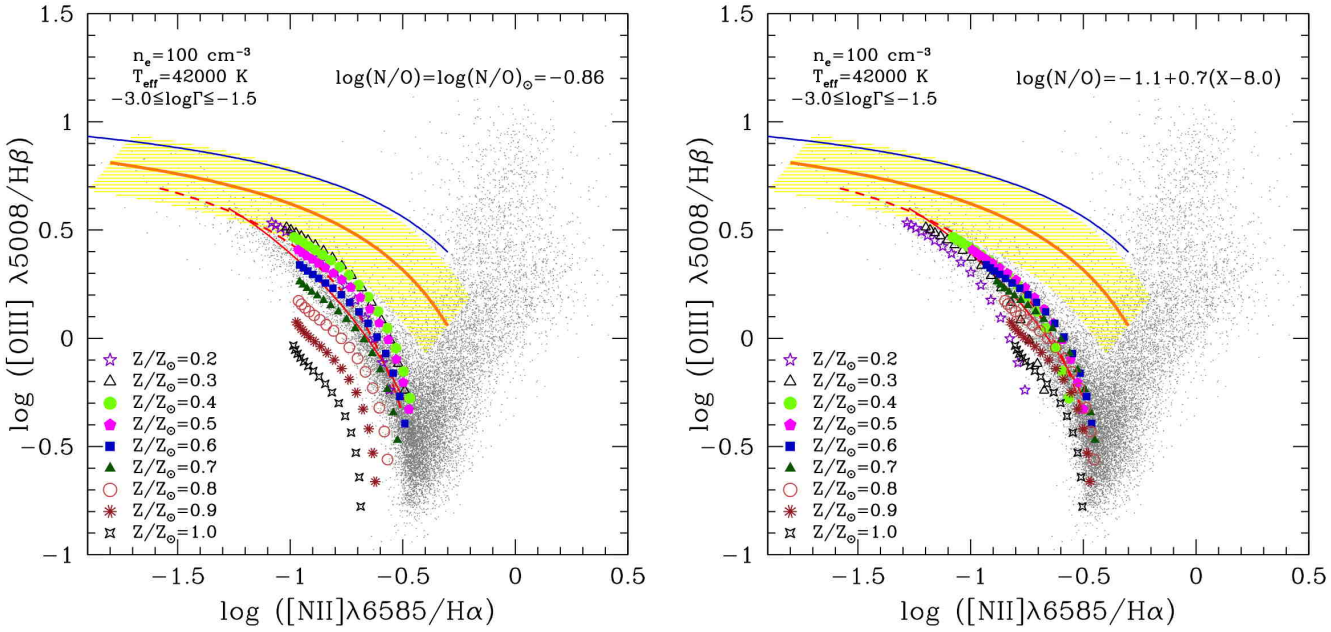

FIG. 13.— BPT diagram showing example photoionization model grids capable of reproducing the salient features of the star-forming galaxy sequence at low redshift. The point colors and symbols depend on assumed O/H relative to the solar values, with the ionization parameter Γ spanning the same range at each metallicity, in steps of $\Delta\log\Gamma = 0.1$. The assumed radiation field shape is that of a $T_{\rm eff} = 42000$ K blackbody. (*Left:*) Models for which the solar ratio of N/O (i.e., independent of O/H) has been assumed (*Right:*) Models which have N/O varying with O/H as in equation 11. Note that the assumptions about N/O have two effects: one is to shift the model loci onto the low-redshift BPT locus. The other is to introduce a dependence on O/H of the position along the BPT sequence, at least for $Z/Z_\odot \lesssim 0.5$. Note that in both model sets, no assumptions have been made about depletion of N or O onto grains (both assume zero depletion).

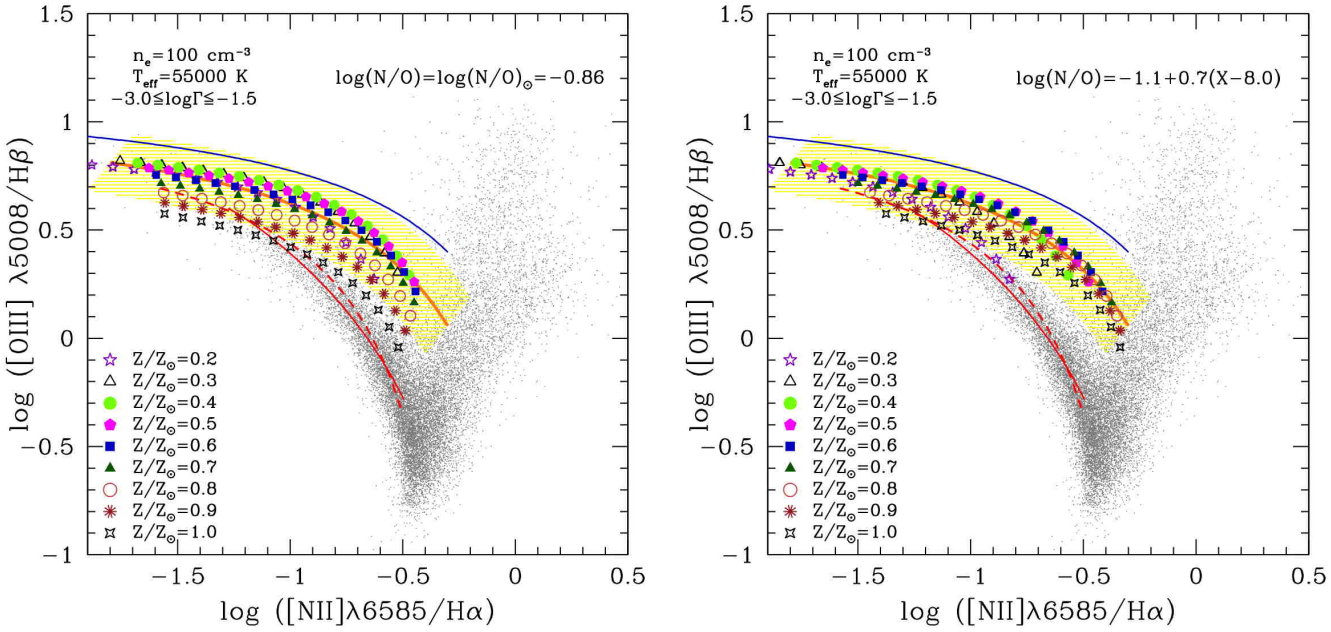

FIG. 14.— Predictions for the locations on the BPT diagram as in Figure 13, where the only change is that $T_{\rm eff}$ of the ionizing sources has been increased from 42000 K to 55000 K. As in Figure 13, the left-hand panel is for solar N/O, while the right-hand panel assumes that N/O is dependent on O/H according to equation 11.

Figure 14 illustrates another potentially important set of issues, when viewed together with Figure 13: the higher overall excitation of the high redshift BPT sequence has the effect of "compressing" the predicted metallicity dependence of the models, and it is possible to match both the low redshift and high redshift BPT sequences with the same model (with the same modest dependence of N/O on O/H) where the only change was to increase $T_{\rm eff}$ from 42000 K to 55000 K. Figures 13 and 14 show why the lower portion of the BPT sequence, so prominent in the low-redshift galaxy samples where it is extremely sensitive to N/O versus O/H, may be much less apparent in high redshift sample. At both low and high redshifts, it remains the case that the BPT sequence is primarily a sequence in Γ, with the vertical position (i.e., in $\log([\mathrm{OIII}]/\mathrm{H}\beta)$) of the leftward "bend" being primarily sensitive to the radiation field shape. Comparison of the right-hand panels of Figures 13 and 14 shows that a galaxy's position in the BPT plane may be significantly less dependent on metallicity (N/O *or* O/H) as compared to local galaxies. It also suggests that the highest metallicity objects at high redshift might be expected in the region between the two "branches" of the BPT diagram, where they might ordinarily be classified as AGN or AGN/star-forming composite objects (see section 5).

4.4. *Is $T_{\rm eff} = 50000$ K reasonable?*

While more sophisticated modeling is beyond the scope of this paper, we note that the upper envelope of the KBSS-MOSFIRE $z = 2-2.6$ sample (Figure 5) is well-represented by the models with $T_{\rm eff} \simeq 55000-60000$ K (see Figure 9), which strongly resembles the so-called "maximum starburst" model curve of Kewley et al. (2001), whose main distinguishing characteristic was a much "harder" stellar ionizing radiation field between 1 and 4 Ryd compared to standard stellar models. The main point is that high ionization parameter *and* hard (i.e., high $T_{\rm eff}$) ionizing spectra are both required to easily match the observations.

Stellar models capable of producing the inferred harder radiation field have been proposed– particularly those including binaries and/or rotation (e.g., Eldridge & Stanway 2009; Brott et al. 2011; Levesque et al. 2012; see also Figure 7). In fact, the shape of the ionizing spectra of individual massive stars, and the expected net radiation field from massive star populations, remain very uncertain, both theoretically and observationally. Indeed, there are other areas where tension exists between observations and stellar evolution models– for example, the very blue observed colors of a fraction of star-forming galaxies at $z \gtrsim 2.7$ which indicate little or no "break" shortward of the rest-frame Lyman limit (e.g., Iwata et al. 2009; Nestor et al. 2011; Mostardi et al. 2013), or the possible shortfall of H-ionizing photons from known galaxy populations at redshifts relevant for reionization. This issue is discussed further in section 8 below.

Increased importance of binarity and rotation (which are expected to be strongly coupled, since mass loss in binary systems naturally produces more rapidly-rotating stars– see, e.g. Eldridge & Stanway 2012) among massive stars could reasonably explain a number of qualitative properties observed in the high-redshift H II regions. Aside from producing massive stars that evolve toward *hotter* $T_{\rm eff}$ while on the main sequence, rapid rotation also results in larger UV luminosities and longer main sequence lifetimes at a given mass and metallicity (Brott et al. 2011). The effects become much stronger in stars with metallicities comparable to that of the LMC (assumed in the models to have 12+log(O/H)=8.35, similar to the mean inferred metallicity of the $z \simeq 2.3$ sample). Models suggest that all rapid rotators with $M \gtrsim 30 M_{\odot}$ spend a substantial fraction of their lifetimes with $T_{\rm eff} \sim 50000-60000$ K, much hotter than their slowly-rotating counterparts (see Figure 7 of Brott et al. 2011). Rapidly-rotating massive stars also produce much more N during their main-sequence evolution, possibly affecting the gas-phase N/O in the surrounding nebula (see section 4.2 for further discussion). *The implication is that it may not be necessary to invoke unusual numbers of Wolf-Rayet stars, extremely young stellar population ages, or extremely "top-heavy" initial mass functions (IMFs) to understand the high $T_{\rm eff}$ that appear to be common in high redshift galaxies.* It thus seems entirely plausible that the BPT sequence observed for $z \sim 2.3$ galaxies could be driven by changes in stellar evolution that are favored in high redshift star-forming galaxies compared to most galaxies in the local samples.

Of course, there are other potentially important physical processes that could alter the positions of galaxies in the BPT plane. For example, it has been shown recently that shifts in the BPT diagram can result from H II regions in which radiation pressure dominates over gas pressure, so that the standard assumption of constant electron density breaks down and the structure of the H II zone is fundamentally altered (Verdolini et al. 2013; Yeh et al. 2013.) Alternatively, shocks almost certainly play some role in modulating the locations of galaxies in the BPT plane (e.g., Newman et al. 2013; Kewley et al. 2013a), particularly for galaxies with $\log(\mathrm{M}_*/\mathrm{M}_{\odot}) \gtrsim 11$ where kinematic evidence for AGN activity often accompanies large values of the N2 ratio (Förster Schreiber et al. 2014; Genzel et al. 2014; see also section 5). Objects for which shocks dominate (energetically) over star formation in the integrated spectrum are evidently rare at lower stellar masses in the high redshift universe; however, it has been shown that, at least in some cases, spatially resolved spectroscopy (particularly with higher spatial resolution observations assisted by adaptive optics) reveals nuclear regions dominated by shocks and/or AGN excitation in what might otherwise appear to be a normal star-forming object (Wright et al. 2010). However, the bulk of $z \sim 2.3$ BPT locus is most easily explained by photoionization, as described above. For the sake of simplicity, since the vast majority of the current sample does not appear to require shocks to explain the observations in the context of the BPT diagram, we will not consider them further.

4.5. *N2 and O3N2 Calibrations, Revisited*

Thus far we have used the calibrations presented by PP04 for mapping the N2 and O3N2 indices to oxygen abundances determined from direct $T_{\rm e}$ measurements. We have seen above that both of these calibrations are sensitive (through the N2 index) to the behavior of N/O as a function of O/H, so that differences in this behavior between the local calibration set and the high-redshift galaxies could produce systematic differences in inferred 12+log(O/H). Systematically higher N/O at a given O/H in the high redshift sample could potentially account for the N2-inferred oxygen abundances being systematically higher than the corresponding O3N2 values (see Figure 6).

According to the linear versions of the PP04 calibrations,

$$12+\log(\mathrm{O/H})_{\mathrm{N2}} = 8.90+0.57\times \mathrm{N2} \quad (12)$$

and

$$12+\log(\mathrm{O/H})_{\mathrm{O3N2}} = 8.73-0.32\times \mathrm{O3N2} \quad (13)$$

so the dependence of the inferred metallicity on N2 is shallower in the case of O3N2. In addition, both PP04 fits intentionally cover a wide range of line indices– considerably wider than the range observed in the current KBSS-MOSFIRE sample– in order to calibrate the index over the widest possible metallicity range. It may be useful in the case of the $z \sim 2.3$ sample to restrict the calibration data set to the same range of N2 and O3N2 index observed, since it allows estimation of the calibration uncertainties most relevant to the high redshift sample (see section 7.2 below).

We have repeated the fits to the N2 and O3N2 metallicity calibrations of PP04, using *the same data set and measurement errors as PP04*, with the following exceptions: first, we limited the regression to the range of N2 and O3N2 line indices observed in the KBSS-MOSFIRE $z \sim 2.3$ sample, and second, we have included only the data points for which the oxygen abundance was measured using the direct T_e method, to reduce the effect of systematics on the overall metallicity scales. The results of the least-squares fits are as follows (see Figure 15:)

For N2,

$$12+\log(\mathrm{O/H})_{\mathrm{N2}} = 8.62+0.36\times \mathrm{N2} \qquad (14)$$

$$(\sigma = 0.13 \text{ dex};\ \sigma_{\mathrm{sc}} = 0.10 \text{ dex})$$

where the new fit includes only the PP04 data for which $-1.7 \leq \mathrm{N2} \leq -0.3$ (92 measurements).

For O3N2,

$$12+\log(\mathrm{O/H})_{\mathrm{O3N2}} = 8.66-0.28\times \mathrm{O3N2} \qquad (15)$$

$$(\sigma = 0.12 \text{ dex},\ \sigma_{\mathrm{sc}} = 0.09 \text{ dex})$$

where the fit was restricted to the range $-0.4 \leq \mathrm{O3N2} \leq 2.1$, again including only direct T_e-based oxygen abundances (65 measurements). In both relations, σ is the weighted error between the data points and the best fit, and σ_{sc} is an estimate of the *intrinsic* scatter calculated in a manner analogous to that used above for the $z \sim 2.3$ BPT sequence fits. The values of σ should be compared to those obtained by PP04, $\sigma = 0.18$ dex and $\sigma = 0.14$ dex for N2 and O3N2, respectively. Both calibrations become tighter when considered over the smaller range of line index, with $\sigma_{\mathrm{sc}} \simeq 0.10$ dex and $\sigma_{\mathrm{sc}} \simeq 0.09$ dex for N2 and O3N2, respectively. These values should be viewed as the *minimum* uncertainties in the calibration between the N2 and O3N2 line indices and 12+log(O/H) at $z \simeq 0$.

Using the revised regression formulae in equations 14 and 15 (shown in Figure 15) lowers the systematic offset between the two indicators when applied to the $z \sim 2.3$ sample, primarily because the coefficient in front of the N2 index in equation 14 is substantially reduced relative to that in equation 12, while the new calibration of [O3N2] (equation 15) is nearly identical to the original PP04 solution (equation 13).

Although we have used the data set assembled by PP04, a more recent calibration of O3N2-based oxygen abundances by Pérez-Montero & Contini (2009) finds an almost identical linear fit to that of PP04, $12+\log(\mathrm{O/H}) = 8.74-0.31\times \mathrm{O3N2}$, using a larger sample of T_e-based measurements. In addition, these authors examined how the strong-line calibration of O/H would be affected systematically by N/O; they find that the overall scatter is reduced substantially if a term dependent on N/O is included,

$$12+\log(\mathrm{O/H}) = 8.33-0.31\times \mathrm{O3N2}-0.35\log(\mathrm{N/O}) \qquad (16)$$

Equation 16 becomes identical to that of PP04 if $\log(\mathrm{N/O}) = -1.17$ ($[\mathrm{N/O}] = -0.3$) and matches the normalization of equation 15 at the median O3N2 of the calibration data set (corresponding to $12+\log(\mathrm{O/H}) = 8.32$) if $\log(\mathrm{N/O}) = -1.06$ ($[\mathrm{N/O}] = -0.2$), close to the values inferred for the high redshift sample.

Thus, there is some cause for optimism that, at least in the case of O3N2, the inferred oxygen abundances are not likely to be strongly biased by differences in N/O between the calibration data set compared to that of the high-redshift sample.

4.6. *Direct Metallicity Calibration at $z \sim 2.3$*

At present, there is only a handful of direct metallicity measurements at $z > 1.5$ (Villar-Martín et al. 2004; Yuan & Kewley 2009; Erb et al. 2010; Rigby et al. 2011; Christensen et al. 2012; James et al. 2014; Bayliss et al. 2013), some of which are limits only and/or quite uncertain. In any case, as an ensemble they remain insufficient to discern any systematic trends. At minimum, a cross-check on strong-line abundance estimates at high redshifts will require a substantial sample of galaxies covering a range of implied Γ for which each galaxy has both measurements of the doublet ratio of [OII]$\lambda\lambda$3727, 3729 and/or [SII]$\lambda\lambda$6718, 6732 (for estimates of n_{e}) and the ratio [OIII]λ4364/[OIII]λ5008 in addition to the strong lines. Figure 16 shows that, in the context of the models, measurement of the weak λ4364 feature would (as expected) provide a relatively model-independent measure of *gas phase* oxygen abundance in the high redshift galaxies[27]. Figure 16 also indicates that uncertainties in the radiation field shape (i.e., T_{eff}) may limit the precision of measuring oxygen abundances to $\sim \pm 0.1$ dex; qualitatively, this may be understood as due to the dependence of equilibrium T_{e} on the mean energy per ionizing photon, at fixed metallicity.

As for the general detectability of the [OIII]λ4364 feature, its predicted strength relative to Hβ ranges from 0.1 to 0.03 for $0.05 \lesssim \mathrm{Z/Z_{\odot}} \lesssim 0.5$; the median observed H$\beta$ flux in the current KBSS-MOSFIRE sample is $\mathrm{f(H\beta)} \simeq 7.5\times10^{-18}$ ergs s^{-1} cm^{-2}, with median S/N$\simeq$ 8.6. Thus, typical KBSS-MOSFIRE spectra are within a factor of a few of the expected flux level $\sim 1\times10^{-18}$ ergs s^{-1} cm^{-2}, and the best individual spectra, with $(\mathrm{S/N})_{\mathrm{H}\beta} > 40$, should allow for detections. The results of our analysis of the KBSS-MOSFIRE data on this topic will be presented in future work (see also section 6.) Importantly, all of the strong lines (of [O II], [O III], Hα, Hβ, [N II], and [S II]) plus [O III]λ4364 can be observed from the ground only over the more restrictive range $2.36 \lesssim z \lesssim 2.57$ (see Figure 1); by design, a large fraction of the objects in Tables 1-3 (103 of 251 or 41%) falls in this range. Thus, we expect that analysis of the highest-quality spectra, together with stacks formed from those of typical quality, should allow for the necessary calibration tests using direct T_{e} method measurements of gas-phase oxygen abundances– at least for $z \simeq 2.36-2.57$.

4.7. *Physical Interpretation: Summary*

Sections 4.1-4.5 above have attempted to highlight the *caveats* associated with interpreting the ratios of strong emission lines produced in the H II regions of high redshift galax-

[27] Alternatively, the UV OIII]λ1661,1666 intercombination feature, which is predicted to be somewhat stronger than λ4364 over most of the range in physical conditions covered by the models, can be used instead, although its use introduces a much stronger dependence on accurate nebular extinction estimates–see section 6 for examples.

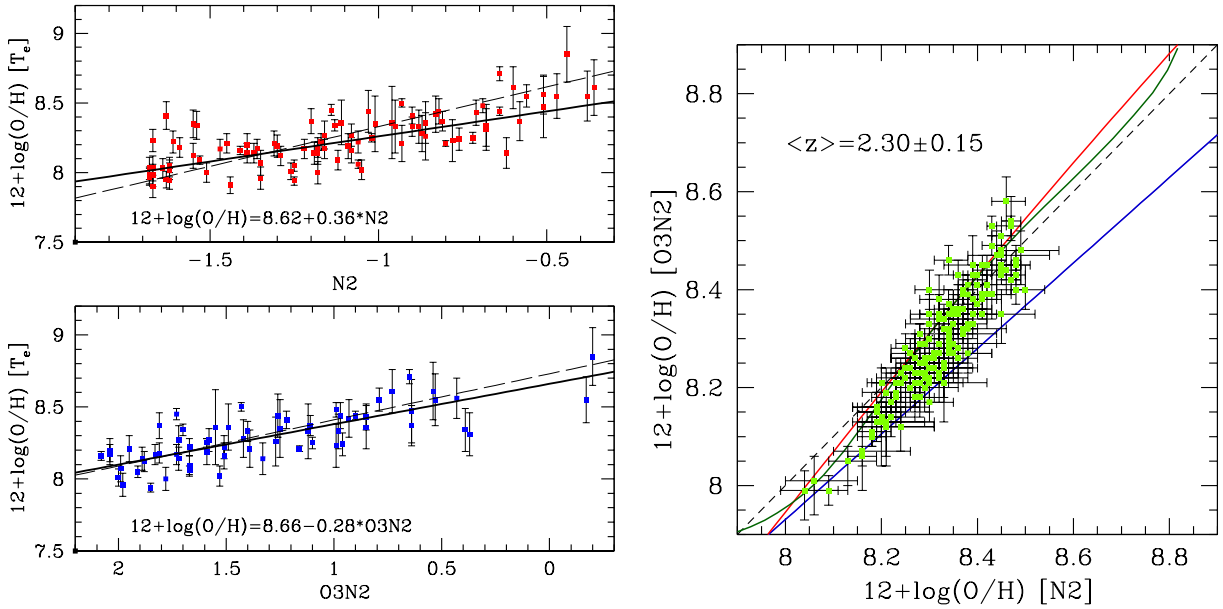

FIG. 15.— (Left) Linear regressions between T_e-based metallicity and the N2 line index ($N2 \equiv \log([NII]\lambda6585/H\alpha)$ (top) and $O3N2 \equiv \log([OIII]\lambda5008/H\beta) - \log([NII]\lambda6585/H\alpha)$ (bottom) for a subset of the data used by PP04, as described in the text. The modified fits, given as an equation in each panel, are shown by the heavy solid lines. The best linear fits given by PP04 (and used in this paper) are shown with lighter, dashed lines. (Right) Same as Figure 6, but assuming the modified calibrations for O3N2 and N2 metallicity measurements given in equations 14 and 15. The blue solid line is best fit linear relationship from Figure 6, using the original PP04 calibrations.

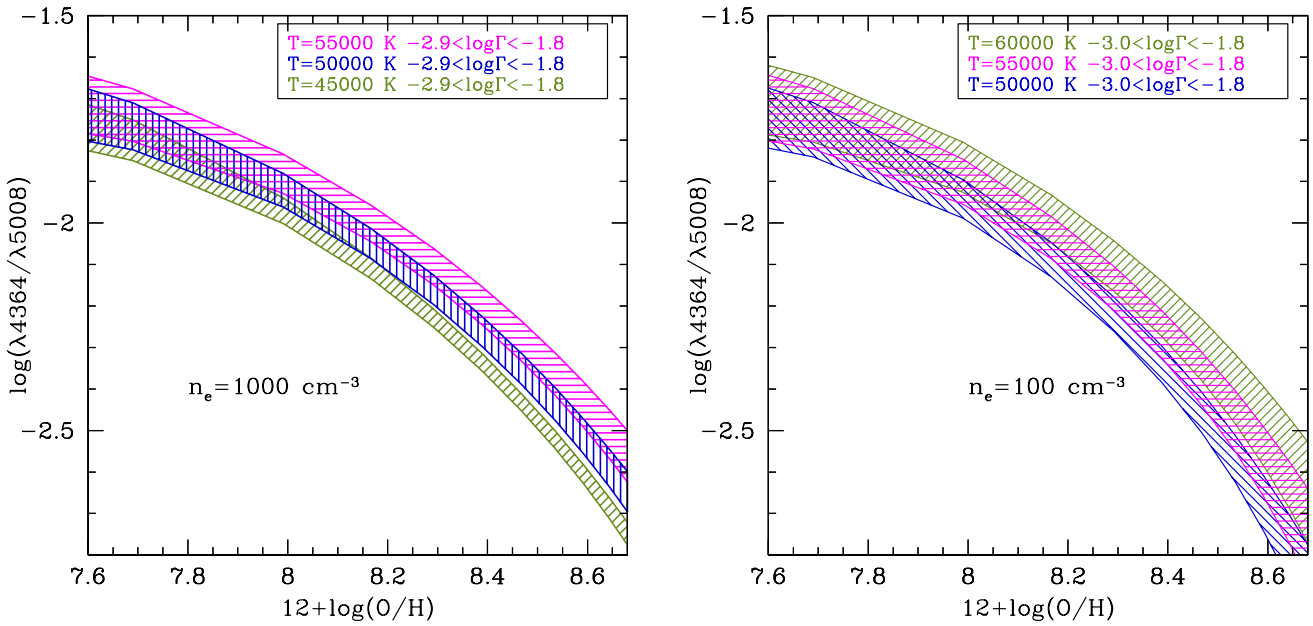

FIG. 16.— The expected intensity of the T_e-sensitive auroral line [OIII]λ4364 relative to [OIII]λ5008 for the range of photoionization models as in Figures 9 and 10. The dependence on the radiation field intensity and shape (as well as on n_e) is modest over this range, so that measurements should yield accurate values of 12+log(O/H) suitable for calibrating the strong-line ratios.

ies in the context of what is known from much more extensively studied "local" star-forming galaxies.

The "offset" in the position of the locus of star-forming galaxies in the high redshift sample compared to the BPT sequence of local star-forming galaxies appears to have contributions, in rough order of importance, from:

- harder stellar ionizing radiation field, needed to explain the preponderance of large observed [OIII]/Hβ in the high redshift sample;
- higher ionization parameters than inferred for most low-redshift star-forming galaxies;
- shallower dependence of (N/O) on (O/H) than is typically inferred for galaxies in the local universe, with (N/O) close to the solar value over the full range of inferred (O/H) (see also Masters et al. 2014, which independently reached a similar conclusion).

The implications of the BPT shift for measurements of gas-phase abundances from strong emission lines remain uncertain, but the generally higher level of excitation, and the less-pronounced behavior of (N/O) vs. (O/H), have the combined effect of *reducing* the degree to which the strong line ratios are sensitive to gas-phase (O/H). However, the inferred higher $T_{\rm eff}$, enhanced (N/O), and higher Γ may all be direct consequences of pronounced differences in the evolution of massive main sequence stars in sub-solar metallicity environments at high redshifts. If so, the differences will have very broad implications– perhaps more important than measurement of gas-phase metallicities.

At present, we suggest that metallicities inferred from strong line ratios should be used with caution until they have been calibrated directly (i.e., at high redshift) using T_e-based measurements, which has become feasible with the advent of multiplexed near-IR spectroscopy. Based on the (currently limited) observational constraints together with inferences from photoionization models, we suggest that the most reliable of the commonly-used strong line indices is O3N2, whose calibration onto the "$T_{\rm e}$" abundance scale appears stable with respect to changes in the (low-z) samples used for calibration, and is only moderately sensitive to the behavior of N/O with O/H, unlike N2. The commonly-used R23 method is unfortunately of limited use over the actual metallicity range most relevant at $z\sim 2.3$, $8.0 \lesssim 12+\log({\rm O/H}) \lesssim 8.7$.

5. AGN VERSUS STELLAR IONIZATION

The BPT diagram has been used most often in the literature as a means of separating galaxies whose nebular spectra are produced predominantly by HII regions from those for which a significant contribution of the observed line emission is likely to have been excited by AGN. The basic principle in distinguishing the star-forming galaxy sequence from that of the so-called "mixing sequence" (see, e.g., Kewley et al. 2001; Kauffmann et al. 2003; Kewley et al. 2013a) is that AGN generally have much harder far-UV spectra than stellar populations, resulting in a tendency to produce higher [OIII]/Hβ relative to [NII]/Hα. In addition, regions near the centers of galaxies harboring AGN tend to be relatively metal-rich, which together with emission from slow shocks that often accompany such activity, pushes [NII]/Hα toward high values. Expectations for the behavior of high-redshift AGN in the BPT plane have been explored in some detail by Kewley et al. (2013a), who pointed out that AGN in low metallicity hosts (which appear to be extremely rare at $z\simeq 0$) could conceivably be found with high [OIII]/Hβ but low [NII]/Hα. If so, they could fall near to the star-forming sequence in the BPT diagram, possibly leading to ambiguities in classification of objects falling above the $z\simeq 0$ star-forming sequence. This is clearly an important issue to address here, since we have shown that nearly all star-forming galaxies at $z\sim 2.3$ are found in that region.

Fortunately, a deep survey at high redshifts such as KBSS provides some advantages for AGN identification over wide-field samples at $z\simeq 0$ such as SDSS. One is that the identification of active galactic nuclei in distant galaxies has been revolutionized in recent years thanks to pointed, very deep X-ray surveys with CHANDRA and mid-IR photometry with SPITZER/IRAC, which image, respectively, the X-rays produced in AGN accretion disks and emission from AGN-heated dust. In addition, most of the galaxies in our KBSS-MOSFIRE sample have already been observed in the rest-frame far-UV using LRIS; the far-UV provides access to emission lines of much higher ionization species than are easily observed in the rest-frame optical (e.g., C IV$\lambda\lambda$1548, 1550, N V$\lambda\lambda$1238,1242.) The presence of nebular emission in such species clearly indicates AGN excitation, since the relevant ionization potentials are too high to have been produced by hot stars (see, e.g., Steidel et al. 2002; Hainline et al. 2011.) By combining what is known from UV spectroscopy with multi-wavelength observations sensitive to the presence of AGN, one would normally not need to rely on the BPT diagram as the primary means of discrimination. Nevertheless, it is useful to examine the small number of objects identified as likely AGN to see where they lie in BPT space.

Five objects in the current sample were identified as AGN based on existing rest-frame UV spectra (Figure 17.) One of the 5 (Q0105-BX58) is a faint broad-lined AGN, while the others have relatively narrow rest-UV emission lines but were flagged as AGN based on strong emission lines of N V, C IV, and He IIλ1640. Figure 18 shows the MOSFIRE spectra of the 5 objects from Figure 17, along with 3 additional AGN identified as such solely on the basis of their rest-frame optical spectra (rest-UV spectra have not yet been obtained). As can be seen in Figure 5, all 8 of these objects occupy positions in the BPT plane that distinguish them from the main locus of $z\sim 2.3$ star-forming galaxies. In addition to the unusual BPT line ratios, the rest-optical emission lines (even for the "narrow-lined" AGN) are substantially broader than typical among the star-forming galaxy sample; see Figure 18.

One object from the list in Table 3, Q0821-RK5, is similarly flagged as an AGN because of its observed $\log([{\rm NII}]/{\rm H}\alpha) = +0.02$ (it has not yet been observed in the H-band, and so does not appear in Figure 5). Such large [N II]/Hα ratios are reached only by galaxies in the "AGN" portion of the BPT diagram for local galaxies, and thus are very likely to harbor AGN; this is supported also by its very red color $(\mathcal{R}-K_s)_{\rm AB} = 3.59$, its very broad and diffuse emission lines ($\sigma = 246$ km s^{-1}, or 99th percentile of all measured Hα line widths) and its huge inferred stellar mass ($\log({\rm M_*/M_\odot}) = 11.79$, by far the largest in the sample) likely due to contamination by hot dust emission in the observed near-IR (see Hainline et al. 2012). In this particular case the SED is ambiguous due to the lack information for observed wavelengths $> 2\mu$m, since Q0821 is the only KBSS field lacking deep IRAC coverage.

Among the KBSS galaxies exhibiting no evidence for AGN (e.g., those falling within or consistent with the shaded region

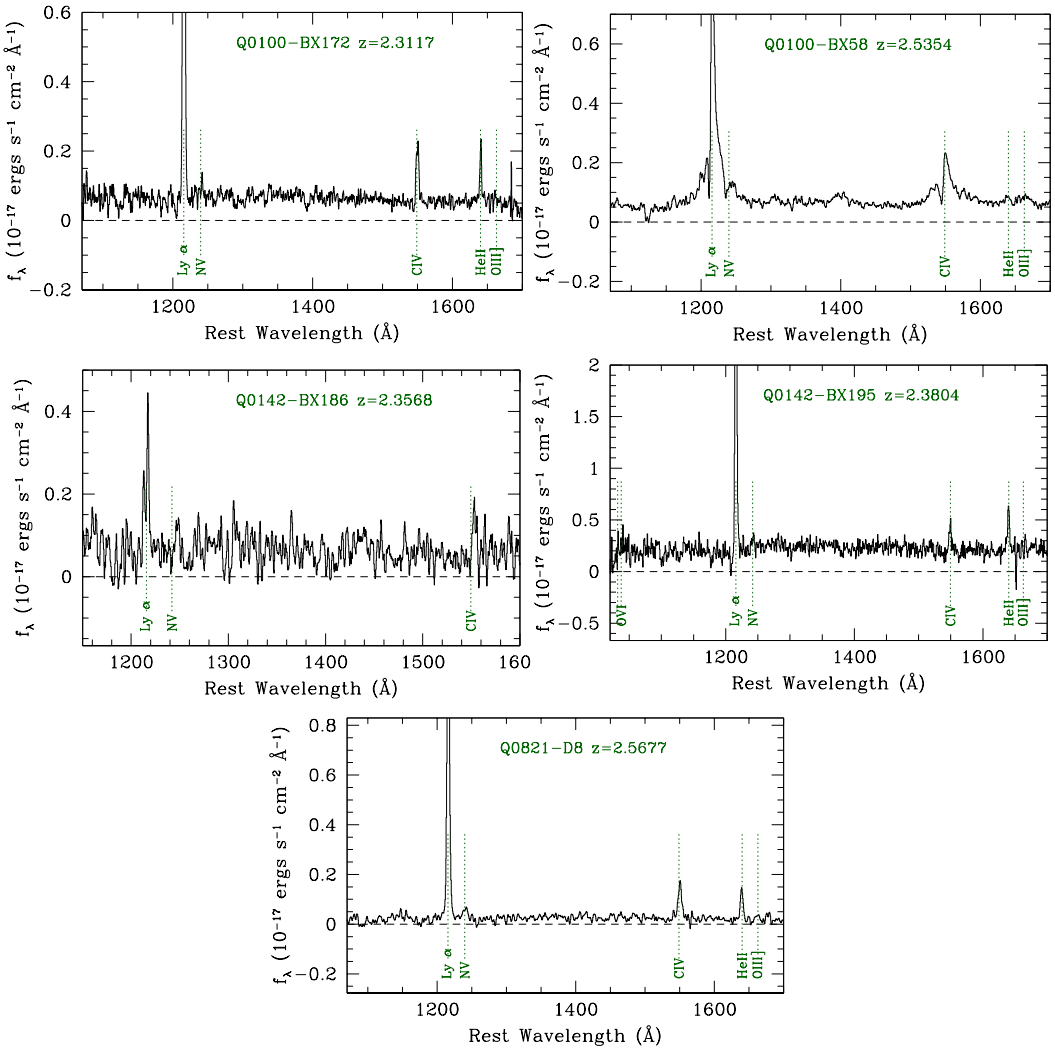

FIG. 17.— Rest-UV spectra (Keck/LRIS-B) for the 5 objects spectroscopically identified as AGN prior to being observed with MOSFIRE; their rest-frame optical MOSFIRE spectra are shown in Figure 18. Emission lines of N V, C IV, and He II clearly indicate the presence of AGN; Q0100-BX58 (top right panel) is a broad-lined AGN, albeit quite faint ($\mathcal{R}$ = 23.4). .

in Figure 5), there appears to be a rather sharp upper limit of log([OIII]/Hβ) $\lesssim$ 0.9. This threshold is exceeded only by two of the objects flagged as AGN. As discussed below in section 6, this upper envelope in [O III]/Hβ implies a maximum $T_{\rm eff}$ for sources dominating the ionizing radiation field, $T_{\rm eff,max} \sim 55000-60000$ K based on our modeling. AGN can exhibit a wide range of energy distributions over the important 1-4 Ryd range, but their shape is approximately a power law rather than an exponential (as in the case of stars) over this interval. Figure 19 helps to illustrate the difference between the assumed blackbody spectra and power-law AGN spectra. Clearly, lines associated with species having ionization potentials above $\simeq$ 50 eV would be more unambiguous signatures of AGN excitation compared to [OII], [OIII], and [NII] transitions available in the rest-frame optical. On the other hand, Figure 19 shows that these ions (particularly [OIII]) are extremely sensitive to $T_{\rm eff}$– e.g., increasing $T_{\rm eff}$ from 45000 K to 55000 K approximately triples the number density of photons capable of ionizing O II to O III relative to those that can ionize H I to H II. Although the possible range of AGN SEDs is large, and while AGN would tend to produce larger ratios of [O III]/Hβ, they would nevertheless be unlikely to produce a *consistent* upper envelope at a particular value ([OIII]/Hβ $\simeq$ 0.9) as observed in the $z \sim 2.3$ sample.

There is a small number of galaxies (see Figure 5) whose positions on the BPT plane might be considered ambiguous in terms of their classification (those lying above the yellow shaded region but below the objects known to be AGN), but they all have relatively large error bars, so that their true positions may well lie within the $z \sim 2.3$ star forming sequence. Thus, we conclude that AGN excitation plays a significant role in only a small fraction of the KBSS-MOSFIRE sample. The 9 identified AGN have been excluded from most analyses in this paper, since their strong line ratios are unlikely to be related to stellar processes.

6. LOCAL ANALOGS OF KBSS-MOSFIRE GALAXIES

It is potentially instructive to examine what is known about a relatively local population of galaxies that in many respects resembles both typical and extreme members of the KBSS-MOSFIRE sample at $z \simeq 2.3$: the so-called "green pea" (GP) galaxies (e.g., Cardamone et al. 2009) are relatively rare $z \simeq 0.2$ objects selected by their distinctive colors caused by unusually large [O III] equivalent widths. As shown in Figure 20, these rapidly star-forming, compact galaxies occupy much of the same region of the BPT plane as the high redshift

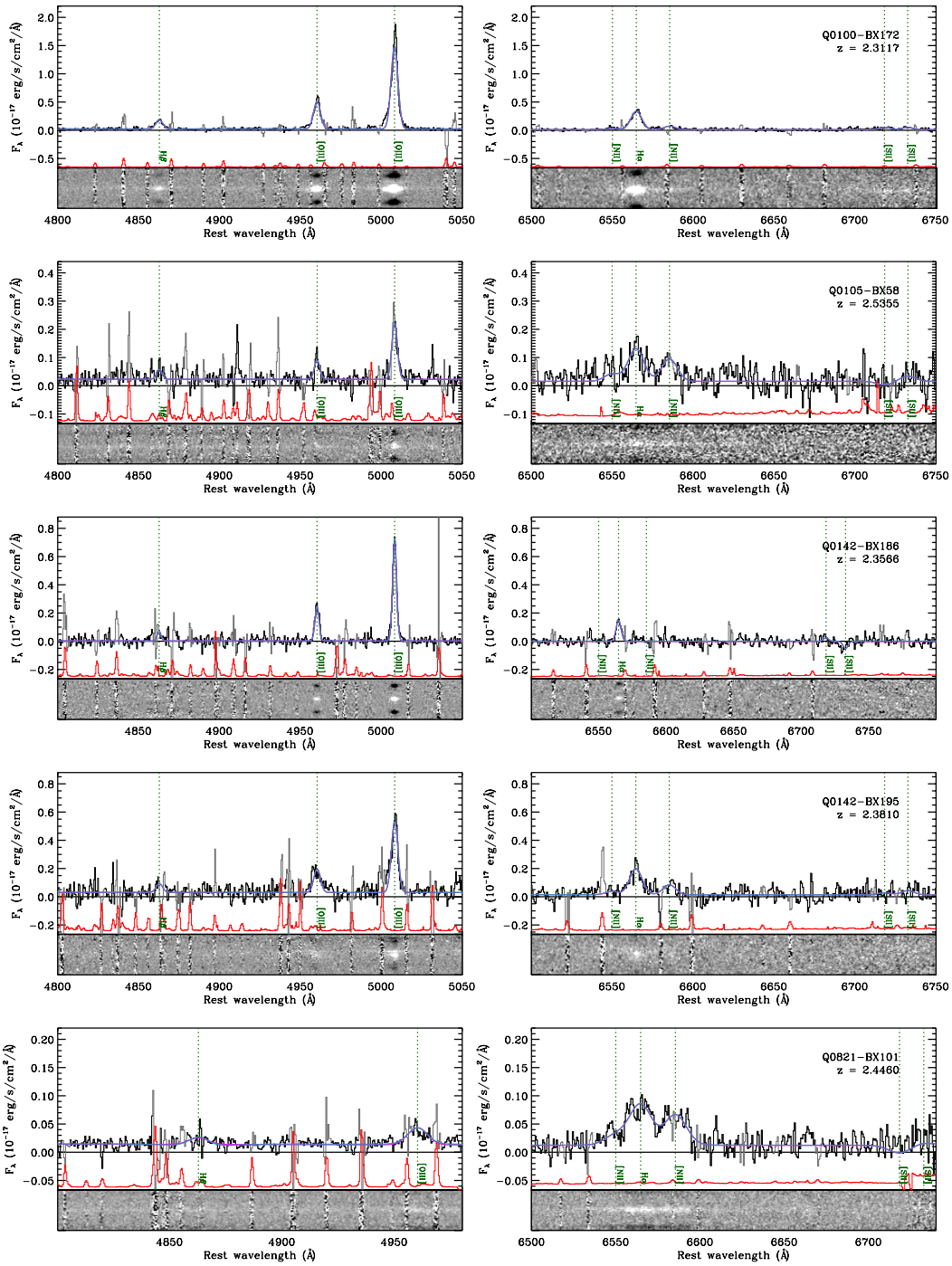

FIG. 18.— MOSFIRE H-band (left) and K-band (right) spectra of the 8 objects in Tables 1 and 2 identified as AGN (those marked with magenta stars in Figure 5).

objects. The sample of 9 GPs in Figure 20 is comprised of 6 "extreme" GPs studied by Jaskot & Oey (2013) and 3 "normal" GPs with very deep follow-up spectroscopy (Amorín et al. 2012). These 9 galaxies have a complete set of strong nebular lines as well as metallicity measurements based on the direct T_e method; they serve as a possible "preview" of the efficacy of the strong line metallicity measurements for similar galaxies at higher redshifts.

First, we note that our simple photoionization models [more sophisticated, but less general, models were presented by Jaskot & Oey (2013) and Amorín et al. (2012) in interpreting their data] presented in section 4 above are able to reproduce both the position of the GPs in the BPT plane (left panel of Figure 20) and the behavior of the N2 and O3N2 indices measured from the GPs' strong line ratios (right panel of Figure 20). The corresponding direct method metallicities (indicated in Figure 20b beside each point) show good agreement when the O3N2 and N2-based numbers are near 12+log(O/H)$\simeq$ 8.0 (true for all 6 of the "extreme green peas"), but the 3 "normal" GP galaxies suggest a possible issue[28]:

[28] We note that the GP whose direct metallicity is most discrepant with the

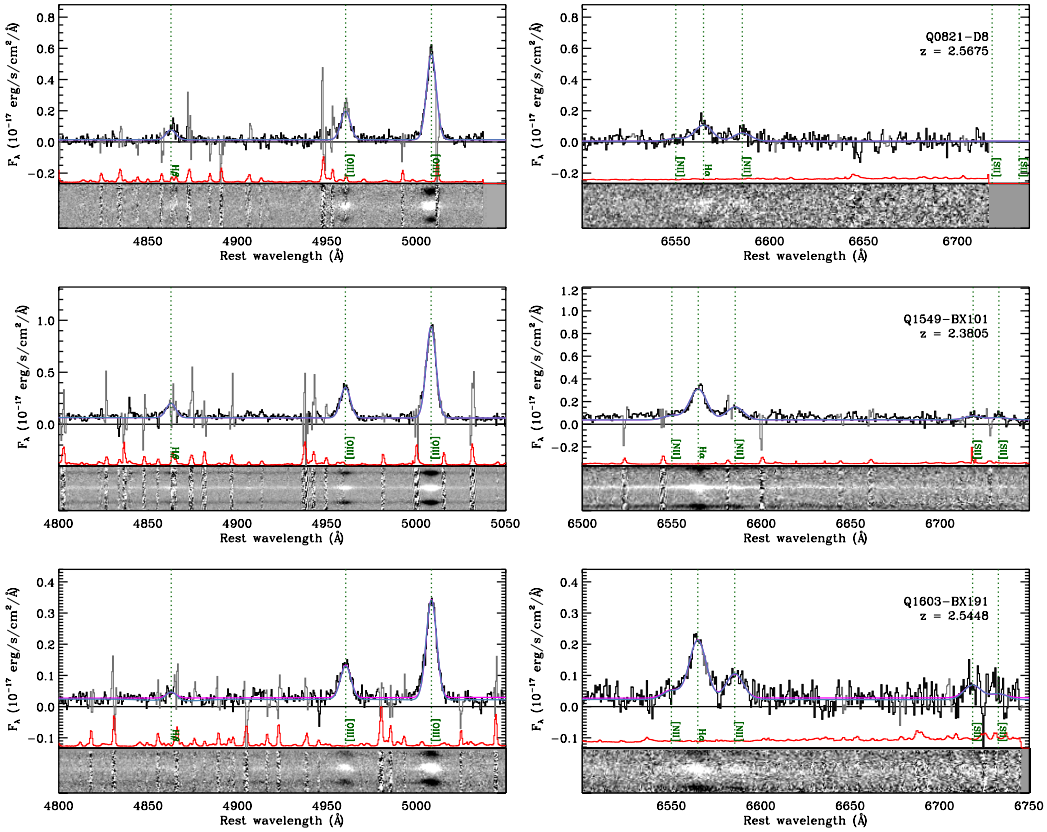

FIG. 18.— (Continued)

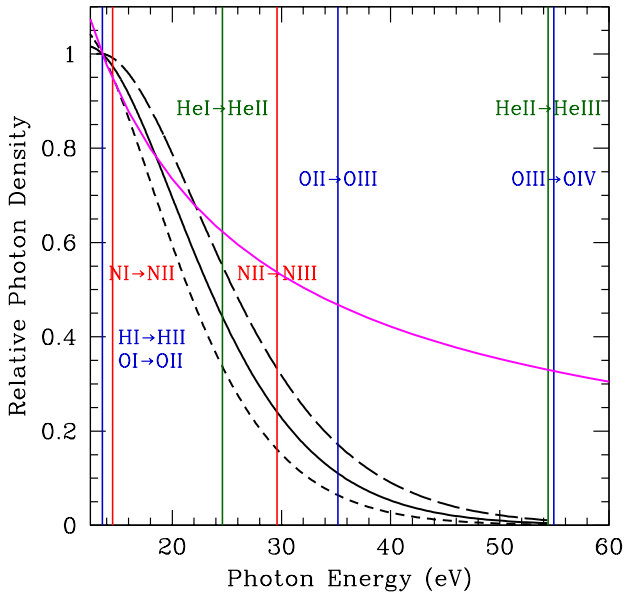

FIG. 19.— Illustration of the relative photon density of ionizing photons under various assumptions about the ionizing radiation field. The vertical lines indicate the ionization potential for ions most relevant to the observations. The black curves are for blackbody spectra with T_{eff} = 45000, 50000, and 55000 K (short-dashed, solid, and long-dashed lines, respectively). The magenta curve is for a power law spectrum of the form $f_\nu \propto \nu^{-\alpha}$, with $\alpha = 0.8$.

strong line estimators (GP232539; Amorín et al. 2012) has $z = 0.277$, which places the weak [OIII]λ4364 feature at an observed wavelength of $\sim$ 5572 Å, so that it is possible that its measured intensity has been affected by residuals from the strong 5577 Å night sky emission line; there is a positive residual at the position of the (weaker) NaD night sky line in the spectrum.

their direct metallicities are comparable to or even lower than those of the "extreme" examples, but the strong-line indices imply higher metallicities– and the discrepancy may become marginally worse along the sequence followed by both the $z \sim 2.3$ galaxies and by the ionization parameter sequence in the photoionization models. Part of the disagreement relative to the local strong-line calibrations, as pointed out by Amorín et al. (2010), is due to the fact that the GP galaxies appear to have higher (N/O) than typical local galaxies of the same oxygen abundance. The 3 examples in Figure 20 all have log(N/O)$\simeq -1.0$, close to the solar ratio. We recall from section 4 above that roughly solar (N/O) was also inferred for most of the $z \simeq 2.3$ galaxies on the basis of the photoionization models. The "extreme" GPs, on the other hand, appear to have (N/O) consistent with that of local metal-poor dwarf galaxies, with log(N/O)~ -1.5, normally interpreted as systems in which only primary N enrichment has occurred (e.g., van Zee et al. 1998).

6.1. *"Extreme" Galaxies at $z \simeq 2.3$*

In fact, the extreme GPs have properties very similar to our most extreme $z \sim 2.3$ galaxies– most of which have only upper limits on [N II/Hα] (light green triangles in Figure 20a) as well as the highest values of [O III]/Hβ in the sample, with log([OIII]/Hβ) $\simeq 0.9$. Thus, it appears that the extreme galaxies at both low and high redshift share a common "upper envelope" in the BPT diagram, previously discussed in section 5.

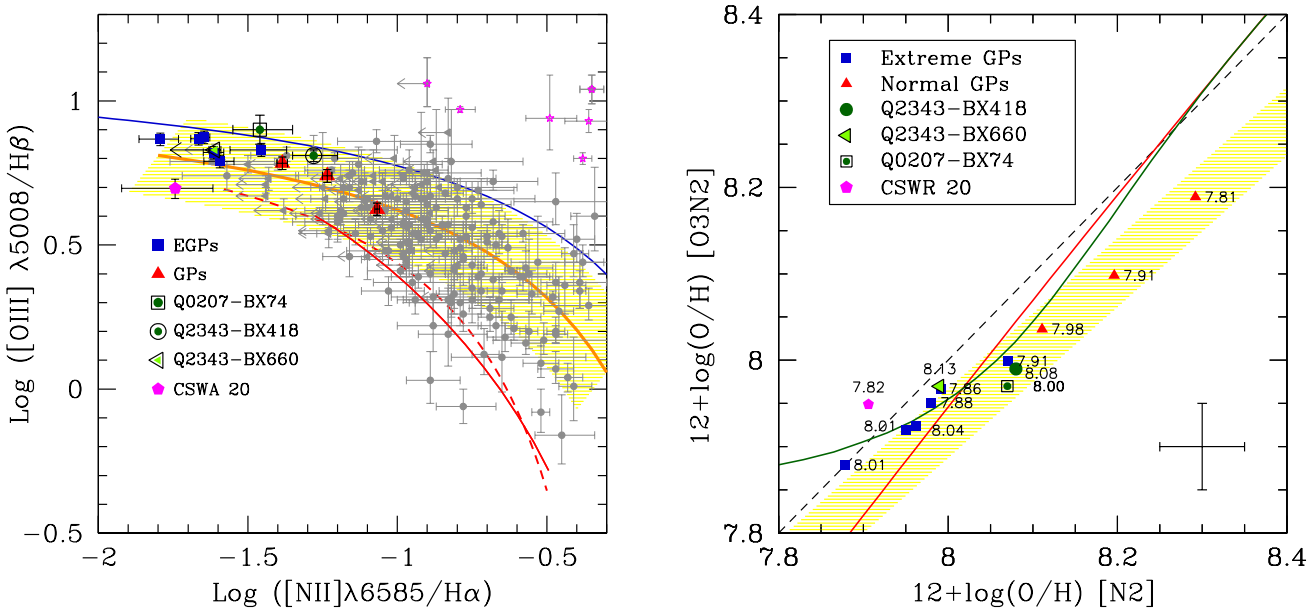

FIG. 20.— (Left) Plot analogous to Figure 9, but adding 9 $z \simeq 0.2$ "green pea" galaxies (EGP: dark blue squares; GP: red triangles). (Right) Analogous to Figures 6 and 10, showing the metallicities that would be inferred using the N2 and O3N2 indices for the GPs (blue squares), EGPs (red triangles), the 3 $z \sim 2$ galaxies with direct metallicity measurements (this work; green symbols), and CSWA 20, a $z = 1.4$ lensed galaxy (James et al. 2014; magenta pentagon.) For each point, the value of 12+log(O/H) measured from the direct method is indicated (see text for discussion, and Figure 22. The errorbar in the righthand panel show the typical uncertainties on the T_e-based metallicity determinations; the formal uncertainties for the N2- and O3N2-based determinations are similar or smaller.)

Three galaxies in the current KBSS-MOSFIRE sample (Q2343-BX418, Q2343-BX660, and Q0207-BX74) are found near the EGPs in the BPT diagram, and have particularly good MOSFIRE (J, H, and K bands) as well as LRIS-B (rest-frame UV) spectra; they are indicated in Figure 20. Q2343-BX418 ($z = 2.3053$) was studied in detail by Erb et al. (2010) as a prototypical example of a UV-bright galaxy with little or no reddening, strong Lyman α emission, and unusually strong rest-UV nebular lines of OIII]$\lambda\lambda$1661,1666 and CIII] $\lambda\lambda$1906,1909. Q2343-BX660 ($z = 2.1741$) and Q0207-BX74 ($z = 2.1889$) have similar rest-UV spectra to that of BX418, as shown in Figure 21, as well as similar rest-optical strong line ratios. All 3 galaxies have $\log(M_*/M_\odot) \sim 9.0$ (very similar to the GP sample introduced above), SFR$\simeq 30-50$ $M_\odot$ yr^{-1}, and among the lowest inferred oxygen abundances and highest sSFRs in the current KBSS-MOSFIRE sample. Both Q2343-BX418 and Q2343-BX660 are known to be compact, both in Hα emission (from Keck/OSIRIS laser guide star AO IFU observations; Law et al. 2009) and in the rest-optical continuum (from HST/WFC3 F160W observations; Law et al. 2012). Q0207-BX74 appears to be similarly compact, though as yet no AO or HST observations are available.

Erb et al. (2010) used measurements of rest-UV OIII] intercombination lines (at the redshift of BX418, [OIII]λ4364 does not fall within one of the ground-based atmospheric windows) together with rest-optical nebular emission based on Keck/NIRSPEC spectra to measure T_e and thus "direct" metallicities, finding 12+log(O/H)= 7.8 ± 0.1, where some of the uncertainty stems from a non-detection of [OII]λ3727,3729 (so that the contribution of O^+ to O/H could not be determined). We have re-observed Q2343-BX418 with MOSFIRE in J, H, and K bands, covering, in addition to the BPT line ratios (Table 1 and Figure 5), the [OII]$\lambda\lambda$3726,3729 doublet, detected with S/N$\sim$ 30. The observations in the 3 near-IR bands were obtained on the same night and carefully cross-calibrated to remove any differential slit losses using observations of a calibration star placed on one of the slits for all 3 observations. We used these observations to calculate the electron density n_e from the [OII] doublet ratio, the Balmer decrement (Hα/Hβ), the ratio

$$O32 \equiv [OIII](\lambda 4960+\lambda 5008)/[OII](\lambda 3727+\lambda 3729) \quad (17)$$

and, using the new [OIII]λ5008 measurement together with the rest-UV measurement of the OIII]$\lambda\lambda$1661,1666 intercombination feature presented by Erb et al. (2010), the electron temperature T_e[OIII], from which (O^{++}/H^+) was derived. The ratio (O^+/H^+) was inferred assuming $T_e([OII]) \simeq T_e([OIII])$ as indicated by photoionization models, yielding a direct measure of 12+log(O/H) assuming that $(O/H) = (O^{++}/H^+)+(O^+/H^+)$. The results are summarized in Table 4. We have assumed zero nebular extinction as in Erb et al. (2010), supported by both the Balmer decrement and the SED fitting results, and find $12+\log(O/H) = 8.08 \pm 0.05$, $\simeq 0.3$ dex higher than that obtained by Erb et al. (2010). The difference is attributable to a lower derived T_e driven by a larger [OIII]λ5008 flux from the new H-band spectrum, as well as the detection of the [OII]$\lambda\lambda$3727,3729 doublet, which allowed the contribution to (O/H) from O^+ to be included. We also note that the measured O32 $\simeq 10$ is in excellent agreement with the photoionization models that reproduce BX418's position on the BPT diagram (see section 4).

We performed similar analyses for Q2343-BX660 and Q0207-BX74. As summarized in Table 4, we infer high values of $n_e = 300-1600$ cm^{-3}, very high ionization level (based on O32), and direct oxygen abundances 12+log(O/H)$\simeq$ 8.00–8.15. Once again the measurement of T_e[OIII] is based on the rest-UV OIII] doublet strength relative to [OIII]λ5008, and the oxygen abundance includes the contribution from O^+; the

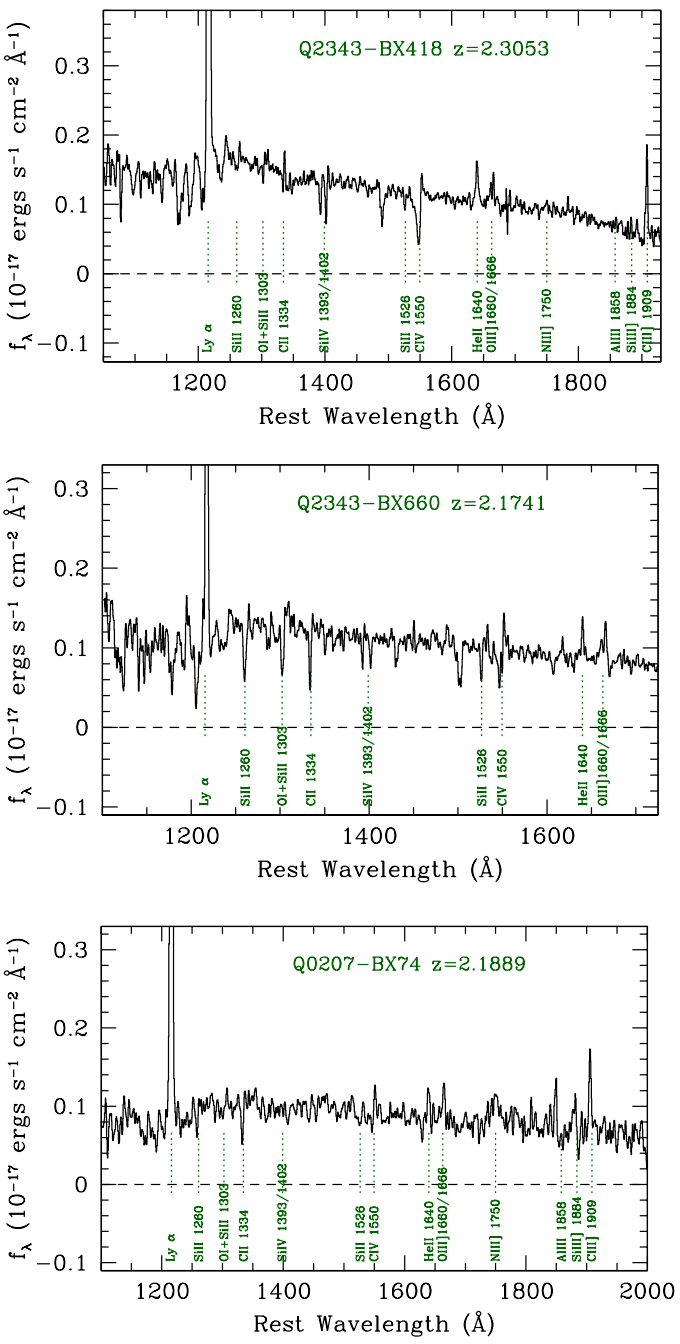

FIG. 21.— Rest-UV Keck/LRIS-B spectra of (top) Q2343-BX418 (see Erb et al. 2010), (middle) Q2343-BX660 and (bottom) Q0207-BX74 Note the presence of unusually strong lines of OIII] $\lambda\lambda$1661, 1666 and the [CIII]+CIII] blend near 1908 Å.

Keck/LRIS-B spectra used to measure the UV features are shown in Figure 21.

The disadvantage of using the UV [O III] feature instead of [O III]λ4364 to measure T_e is that it is much more sensitive to the nebular extinction correction. Fortunately, two of the 3 galaxies for which the measurements are available (BX418 and BX660) are consistent with zero nebular extinction based on the observed Hα/Hβ ratio (the "Balmer decrement"), which are each consistent with the "Case B" expectation of Hα/Hβ = 2.86; both are also consistent with zero extinction based on their SED fits.

For Q0207-BX74, based on the observed Balmer decrement, we obtain $E(B-V)_{neb} = 0.18$, while the stellar continuum (from SED fitting) has $E(B-V)_{cont} = 0.13$ assuming the Calzetti et al. (2000) attenuation relation. We corrected the relevant line fluxes in Table 4 assuming the former and the Cardelli et al. (1989) extinction curve. Note that effect of the dust correction to the observed ratio OIII](λ1661+λ1666)/[OIII]λ5008 was to increase it by a factor of 2.04, increasing the inferred T_e from $\sim$ 12140 K to $\sim$ 14300 K and lowering the inferred oxygen abundance by $\sim$ 0.23 dex, from 8.23 to 8.00.

Figure 22 summarizes the comparison of the direct metallicity estimates for the same 13 galaxies as in Figure 20. In addition to the N2 and O3N2-based estimates, we have applied the low-metallicity branch of the R23 calibration of McGaugh (1991) [as expressed by Kobulnicky et al. 1999] to the measurements of O32 and $([OIII]_{tot}+[OII]_{tot})/H\beta$, to estimate R23-based metallicities, shown in the rightmost panel of Figure 22. Figure 22 suggests that, at least for this sample, O3N2 provides a slightly better approximation to the direct method metallicities, with a relative offset of $\log(O/H)_{O3N2} - \log(O/H)_{dir} = 0.00 \pm 0.11$ dex, while $\log(O/H)_{N2} - \log(O/H)_{dir} = 0.04 \pm 0.14$ dex and $\log(O/H)_{R23} - \log(O/H)_{dir} = 0.16 \pm 0.08$ dex. We caution that these statistics are based on a very small sample, confined to low metallicities where the various indicators appear to be in reasonable agreement with one another; however, the finding that the O3N2 index provides the least-biased estimate of direct-method metallicities for galaxies offset from the BPT excitation sequence is consistent with results presented by Liu et al. (2008) for $z \simeq 0$ SDSS galaxies; these authors found that N2 systematically over-estimates 12+log(O/H) compared to the direct method. *On balance, it seems most likely that the O3N2 index yields more reliable values of 12+log(O/H) than those derived from the N2 index.*

7. THE M_*-METALLICITY RELATION AT $\langle Z \rangle = 2.3$

A correlation between stellar mass M_* and nebular oxygen abundance has now been well-established at $z \simeq 0$ using both strong-line metallicity measurements (e.g., Tremonti et al. 2004; Kewley & Ellison 2008; Maiolino et al. 2008) as well as direct T_e-based measures (Andrews & Martini 2013). However, even in the local universe the quantitative behavior of the mass-metallicity relation (MZR) depends substantially on the method used to measure 12+log(O/H). Apparently similar behavior, with substantial offsets in the sense that galaxies are inferred to have lower ionized gas metallicities at a given M_*, has been observed for relatively small samples of $z > 2$ galaxies (Erb et al. 2006a; Maiolino et al. 2008; Law et al. 2009; Förster Schreiber et al. 2009; Henry et al. 2013; Newman et al. 2013; Wuyts et al. 2014; Kewley et al. 2013b).

As we have seen above, we do not yet know whether the strong-line determinations of metallicity at high redshift are directly comparable to those obtained at low redshift, even using the same diagnostic. We showed in the previous section that there is evidence, albeit limited, (see Figure 22 and Liu et al. 2008) that the O3N2 calibration is least biased with respect to direct-method metallicities for galaxies falling "above" the low-redshift BPT ionization sequence. We have also shown (see also Newman et al. 2013) that there is a systematic offset of $\Delta \simeq 0.13$ dex between metallicities inferred from the PP04 N2 and O3N2 indices when they are applied to the same galaxies in the KBSS-MOSFIRE $z \simeq 2.3$ sample, in spite of the fact that these calibrations were established using

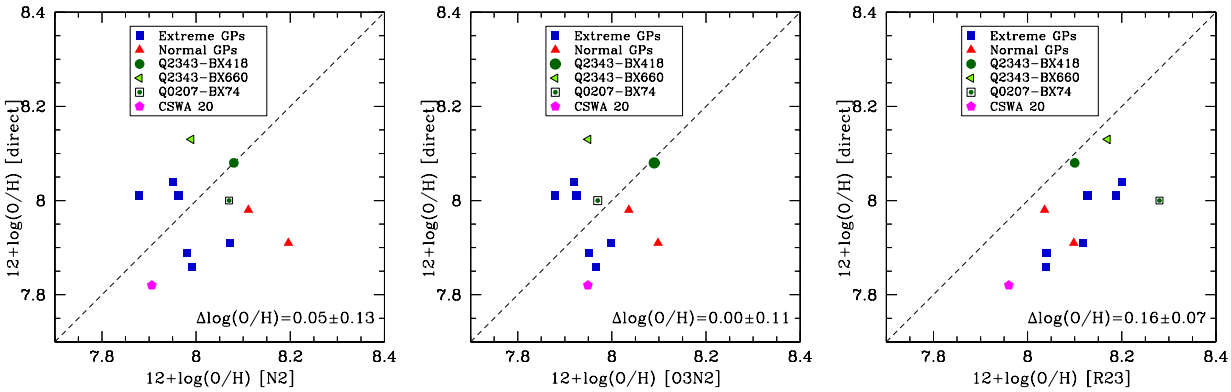

FIG. 22.— Comparison between direct T_e measurements of 12+log(O/H) and values suggested by three different strong-line indicators for the same set of galaxies shown in Figure 20b. Left: N2, Center: O3N2, Right: R23, using the lower-branch calibration of McGaugh (1991) (see text, and Table 4, for details). The mean and rms scatter in the difference between individual measurements of 12+log(O/H) and the direct method measurement is given in the lower right of each panel.

direct T_e abundances of the same local galaxy sample. There is little doubt that other systematic differences in the MZR plane would be found using other local strong line calibrations.

In addition to systematics resulting entirely from application of local calibrations, it is also quite probable that, even at a given redshift, results of different studies may differ in detail either because of the way in which targets are selected, or by differences in the quality and depth of the resulting spectra (see, e.g., Juneau et al. 2014). The degree to which selection and/or observational bias affects global statistics like the MZR will also depend on the extent to which fundamental galaxy properties (which one is trying to measure) are correlated with a galaxy's "observability", as discussed in section 2.4 above. Measuring evolution of the galaxy population in the MZR plane is potentially even more problematic, since selection and observation biases may be changing with redshift in a way that could either mask or exaggerate real differences.

For the moment, since most of our analysis of the nebular spectra in the KBSS-MOSFIRE sample has been focused on measuring the BPT line ratios, we have produced MZRs using both the N2 and O3N2 indices and the PP04 calibrations; the results are shown in Figures 23 and 24. The same set of 242 galaxies with $\langle z \rangle = 2.30 \pm 0.16$ (all objects in Tables 1-3 not classified as AGN) was used for both determinations of the MZR. The N2 data set, shown in Figure 23, has 192 N2 detections (Tables 1 and 3) together with 50 upper limits (Table 2). For O3N2, the sample includes 161 galaxies with detections of both [OIII]/H$\beta$and N2 (Table 1), 50 with [OIII]/Hβ detections and N2 upper limits (Table 2), and 31 galaxies for which only N2 has been measured (Table 3). This last subsample was included by using the fact that KBSS-MOSFIRE galaxies with both N2 and O3N2 measurements fall along a well-defined sequence with small intrinsic scatter (Figure 6); the best-fit linear relation

$$12+\log(\mathrm{O/H})_{\mathrm{O3N2}} = 0.87\,[12+\log(\mathrm{O/H})_{\mathrm{N2}}]+0.94 \qquad (18)$$

was used to convert from N2-based to O3N2-based metallicity scales. The error bars for the converted points include both the uncertainty in N2 and the residual dispersion of the data relative to the fit in equation 18[29].

In both Figures 23 and 24 the long-dashed (orange) lines show the best linear fits to the ensemble of measurements and limits for the full data set. The fits were obtained using the Bayesian linear regression method described by Kelly (2007), which accounts for measurement errors in both the dependent and independent variables, and treats non-detections/limits in a consistent manner. For the purposes of the calculation, we assumed a characteristic uncertainty in $\log(\mathrm{M_*/M_\odot})$ of ± 0.16 dex[30]. The method returns posterior distributions for each parameter, including the variance of the *intrinsic* scatter, which is of particular interest since MZR scatter has not been measured previously at high redshift. Expressing the MZR as a linear function of the form

$$12+\log(\mathrm{O/H}) = \mathrm{Z_{10}}+\gamma\,[\log(\mathrm{M_*/M_\odot})-10] \qquad (19)$$

where $\mathrm{Z_{10}}$ is the metallicity normalization at $\log(\mathrm{M_*/M_\odot}) = 10.0$ and γ is the linear slope, we find best-fit parameters as follows:

$$\mathrm{N2}: \quad \mathrm{Z_{10}} = 8.41 \pm 0.01; \quad \gamma = 0.20 \pm 0.02; \quad \sigma_{sc} = 0.10 \pm 0.01 \qquad (20)$$

and

$$\mathrm{O3N2}: \quad \mathrm{Z_{10}} = 8.27 \pm 0.01; \quad \gamma = 0.19 \pm 0.02 \quad \sigma_{sc} = 0.10 \pm 0.01 \qquad (21)$$

In both cases, σ_{sc} is the best estimate of the *intrinsic* scatter in the MZR relative to the fit. We will return to a discussion of the low intrinsic scatter in the $z \sim 2.3$ MZRs below (section 7.2.

Generally, the low-redshift MZRs such as those used for comparison in Figures 23 and 24 reflect a "flattening" above a characteristic stellar mass; consequently, the fitting functions used to represent them include such a characteristic mass as an additional parameter (e.g., Maiolino et al. 2008; Moustakas et al. 2011; Andrews & Martini 2013; Zahid et al. 2014), somewhat akin to "L^*" in a luminosity function. However, we found that fitting the more complex functions to the KBSS-MOSFIRE data at $z \sim 2.3$ could not be justified, since Figures 23 and 24 clearly show that the linear functions in equations 20 and 21 are good fits, and there is no obvious sign that

[29] This small subsample of the O3N2 data set, which represents only 12.8% of the sample, was included for completeness. Excluding it from the fits discussed below has no significant effect on the results.

[30] The results are insensitive to the exact value adopted; 0.16 dex is the median estimated uncertainty in the stellar mass estimates for similar galaxy samples (Shapley et al. 2005b; Erb et al. 2006c)

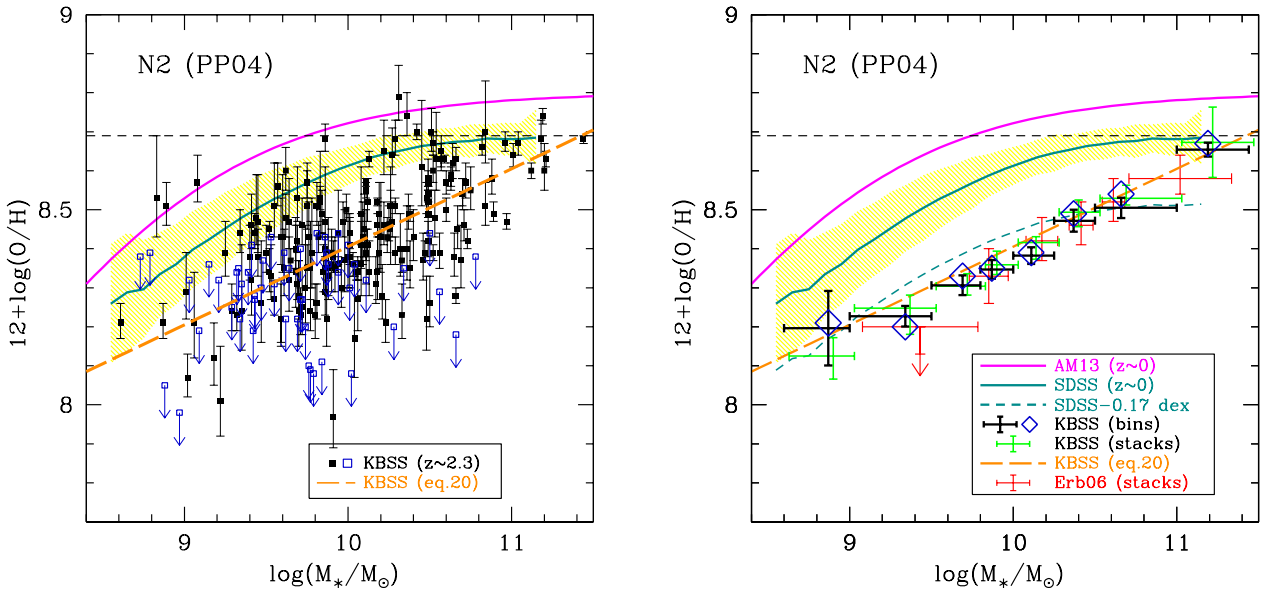

FIG. 23.— (*Left*) Observed relation between stellar mass (M_*) and oxygen abundance inferred from the PP04 N2 index calibration, for $z \sim 2.3$ KBSS-MOSFIRE galaxies. The sample includes 192 galaxies with [NII]/Hα measurements (black points) and 50 with 2σ upper limits on [NII]/Hα (blue open squares, with downward arrows). The long-dashed orange line is the best-fit linear relation between $12+\log(O/H)_{N2}$ and $\log(M_*/M_\odot)$ (equation 21; see text for discussion) using the ensemble of individual measurements (i.e, not binned). The solid turquoise curve and light shading (representing the approximate scatter) is the best-fit MZR for star-forming galaxies in SDSS-DR7, assuming the (linear) N2 calibration of PP04. The solid magenta curve is the best-fit MZR from Andrews & Martini (2013) where metallicities were determined using the direct method based on stacked SDSS spectra in bins of stellar mass. (*Right*) Same as left panel, but with data points binned by stellar mass (see Table 5). The black, heavy error bars are the weighted average metallicities of the individual galaxies in each bin. In the y-direction, the error bars reflect uncertainty in the bi-weight mean within each bin, with the x-direction error bars indicating the limits of the M_* bin. The x-location of each point is determined by the median $\log(M_*/M_\odot)$ within the bin. The blue diamonds are the median inferred metallicity within each stellar mass bin, and the light green error bars are based on stacked spectra in the same bins (see text for discussion). Note that the same linear fit (from equation 20) to the KBSS N2 MZR is shown in both panels, based on the full sample of individual measurements as described in the text. The red error bars show the results of Erb et al. (2006a), based on spectral stacks in bins of stellar mass. The dashed turquoise curve in the righthand panel shows the local SDSS MZR, shifted to lower inferred oxygen abundance by 0.17 dex.

either of the MZRs flattens at high M_*. It is not yet clear how literally one should take apparent differences in shape or normalization of the MZRs at $z \sim 0$ and $z \sim 2.3$ MZRs, for all of the reasons emphasized above. For the same reason, one should probably use caution interpreting similarities or differences between any two galaxy samples without a detailed understanding of the systematics of the selection function, the criteria for successful observation, and the likely systematic issues inherent in mapping strong-line ratios to metallicity.

It is perhaps encouraging, on the other hand, that the posterior likelihood distributions of both γ and σ_{sc} for the $z \sim 2.3$ MZRs are entirely consistent with one another; the only significant difference between them (aside from the larger contribution of measurement errors for N2 as compared to O3N2) is the aforementioned offset in metallicity normalization of 0.13-0.14 dex.

7.1. *The MZR in Bins of* M_*

Erb et al. (2006a) first showed, based on composite spectra formed from bins of M_* (large open diamonds in Figure 23), that the $z \sim 2.3$ MZR lies substantially below the $z \simeq 0$ relation. The amplitude of the shift in metallicity depends on the method used to measure it – Erb et al. (2006a) found that the shift of the $z \sim 2.3$ metallicities (measured using N2) relative to the MZR of Tremonti et al. (2004) was −0.56 dex, but decreased to $\simeq$ −0.3 dex when the PP04 N2 calibration was applied to the SDSS sample. It appears (Figure 23) that the KBSS-MOSFIRE N2-based MZR exhibits a slightly shallower dependence of the N2 index on M_* than the Erb et al. (2006a) sample, at least for low M_*. We note that, although the galaxies targeted by Erb et al. (2006a) came from UV color-selected catalogs defined in the same way as most of the current sample, the KBSS results are nearly independent of the Erb et al. (2006a) sample, in the sense that all of the nebular line measurements are based on new observations with MOSFIRE, and only 25 of 251 galaxies ($\simeq$ 10%) of the new sample were included in that of Erb et al. (2006a).

Referring to Figure 23, the best fit locus of individual galaxies from KBSS-MOSFIRE agrees well with the result from the stacked spectra of Erb et al. (2006a) for $\log(M_*/M_\odot) \gtrsim 9.8$ (i.e., in all but the lowest mass bin of the Erb et al. 2006a data), while for $\log(M_*/M_\odot) \lesssim 9.8$, the KBSS data indicate higher values of $12+\log(O/H)_{N2}$ than the upper limit of Erb et al. (2006a). We discuss the significance of and possible reasons for this discrepancy below.

Most subsequent high-redshift ($z \gtrsim 1.5$) evaluations of the MZR to date have also relied primarily on stacked spectra in bins of M_* as in Erb et al. (2006a) (e.g., Newman et al. 2013; Henry et al. 2013; Cullen et al. 2014; Troncoso et al. 2014; Wuyts et al. 2014; Sanders et al. 2014). To facilitate comparison with other MZR determinations, we evaluated the KBSS-MOSFIRE data in 8 bins of M_* covering the full observed range (see Tables 5 and 6). For the purpose of evaluating stellar mass bins that include objects with metallicity upper limits (in all cases due to the non-detection of [NII]), we assigned each N2 line index non-detection its nominal 1σ upper limit and an uncertainty of $\pm$0.3 dex (i.e., a factor of two). The corresponding metallicity uncertainty was obtained by prop-

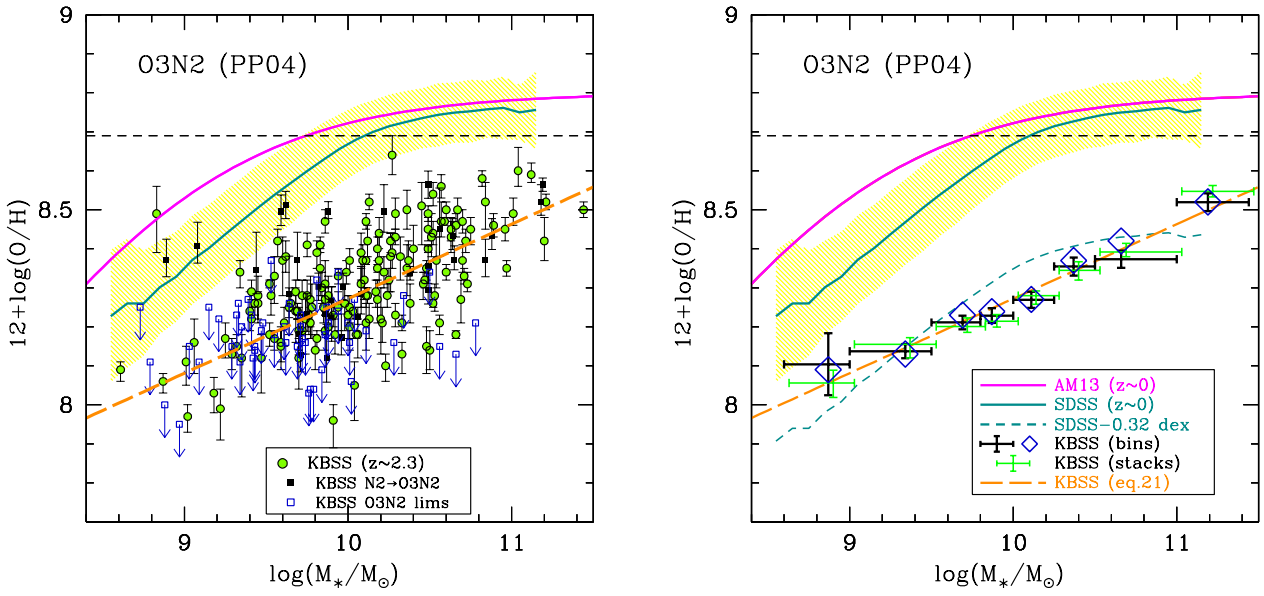

FIG. 24.— (*Left*) Same as Figure 23, but for metallicities inferred from the PP04 O3N2 calibration. Galaxies with individual O3N2 measurements (160 objects; Table 1) are indicated with light green solid dots, while 2σ upper limits on the O3N2 metallicity (51 objects; Table 2) are shown with blue squares. Equation 18 was used to convert the 31 galaxies with N2 but lacking O3N2 measurements (Table 3), represented by solid black squares with error bars). The solid turquoise curve and yellow shaded region represents the $z \simeq 0$ SDSS-DR7 MZR using the same PP04 O3N2 calibration; the magenta curve is the Andrews & Martini (2013) $z \sim 0$ MZR (as in Figure 23). (*Right*) As in Figure 23, where individual measurements were combined within the same bins of stellar mass (see Table 6). In both panels, the long-dashed orange curve is the best linear fit to the O3N2 MZR from equation 21, using all of the individual measurements as described in the text. The dashed turquoise curve in the righthand panel is the low-redshift SDSS relation, shifted to lower oxygen abundance by 0.32 dex.

agating the assumed line index error to a corresponding error in metallicity. For N2-based metallicities, $\sigma = \pm 0.17$ dex on $12+\log(\mathrm{O/H})_{\mathrm{N2}}$, while for O3N2-based metallicities the N2 line index error contributed an uncertainty of $\sim \pm 0.10$ dex, which was propagated along with the [OIII]/Hβ measurement error to obtain a limiting value. We then evaluated the median and the weighted average metallicity within each mass bin; the results are summarized in Tables 5 and 6 and plotted in Figures 23 and 24.

Since only $\sim 20\%$ of the sample has metallicity limits (50 out of 242 galaxies), the bin values are relatively insensitive to the exact metallicity values for the limits. Figures 23 and 24 show both bin mean (black error bars) and bin median (blue diamonds) These values are consistent with one another, as well as with the linear fit to the ensemble of individual measurements (equations 20 and 21 for N2 and O3N2, respectively) described in the previous section.

We also constructed stacked spectra within the same stellar mass bins (to be discussed in detail elsewhere; Strom et al., in preparation) for the KBSS-MOSFIRE sample. Line indices obtained from spectral stacks have distinct advantages, particularly if many of the individual spectra are not of high enough quality to allow object-by-object line ratio measurements, since spectra yielding only upper limits on inferred metallicity can be easily included in the stacks along with those yielding individual detections. However, stacks do require one to choose how to (or whether to) scale the rest-frame spectra of individual galaxies prior to averaging; there are many subtleties to making this choice, and its subsequent effect on the results may depend on the underlying selection method and the nature of any observational biases. For the present, we made spectral stacks for the KBSS-MOSFIRE sample, using the same method employed by Erb et al. (2006a), with results summarized in Tables 5 and 6 and shown in the righthand panels of Figure 23 and 24. As can be seen in Figures 23 and 24, the metallicity values based on stacks are consistent at the $\lesssim 1\sigma$ level with both the median and the average values within each bin; moreover, fits of a linear MZR of the form given in equation 19 to the binned data points (whether one chooses the median, mean, or stacked values) yield values of Z_{10} and γ consistent with the fits to the full sample ensemble (with no binning).

Thus, the origin of the apparent difference between the KBSS sample and that of Erb et al. (2006a) is probably not related to binning/stacking, nor to the details of how one includes spectra with individual N2 upper limits. Aside from pure sample variance (the lowest-mass bin in the Erb et al. (2006a) sample is based on a spectral stack of only 15 galaxies, whereas the KBSS sample contains 85 galaxies in the same stellar mass range), some part of the discrepancy might be explained by very different spectral resolution and S/N (both are considerably higher for the MOSFIRE spectra), when one accounts for the fact that weak emission lines are harder to distinguish from the continuum level, so that systematic errors in the zero level of the spectra can have a large effect on inferred line strength near the detection limit. A related possibility is that there is a real difference in the properties of the galaxy samples at low M_* that leads to different line index measures. One obvious possibility is (e.g.) a different average SFR: the mean SFR in the lowest-M$*$ bin of the Erb et al. (2006a) sample is $\simeq 2.5$ times larger than that of the KBSS galaxies in the same range of M_*; however, we show in section 7.3 below that the inferred metallicities at a given stellar mass within the KBSS sample do not obviously depend on SFR.

In any case, the relation between the strong-line

metallicity– using either the N2 or O3N2 indices– and $\log(M_*/M_\odot)$ is quite shallow over the range in M_* spanned by the KBSS-MOSFIRE sample, with best-fit linear slope of $\gamma \simeq 0.20$ that appears to extend over the full observed range of M_*

7.2. *Scatter in the $z \sim 2.3$ MZR*

As for the BPT locus discussed in section 3 above, it is interesting to compare the degree of scatter in inferred metallicity at fixed M_* at $z \simeq 2.3$ to that observed at low redshift. We found above that, for both N2- and O3N2-based metallicity determinations, the *intrinsic* scatter in the MZR was $\sigma_{sc} \simeq 0.10$ dex, compared to $0.08-0.12$ dex for the SDSS-DR7 sample (Figures 23 and 24; the scatter increases toward lower M_* in the SDSS sample). Dividing the KBSS galaxy sample in half near the median $\log(M_*/M_\odot) = 10.0$ and estimating σ_{sc} separately for each sub-sample, we find no significant difference, with $\sigma_{sc}[\log(M_*/M_\odot) > 10] = 0.11 \pm 0.01$ dex and $\sigma_{sc}[\log(M_*/M_\odot) < 10] = 0.10 \pm 0.01$ dex.

An obvious point, relevant at both $z \sim 0$ and $z \sim 2.3$, is that the scatter in the inferred metallicity at a given stellar mass is *smaller* than could be reasonably expected even if the "true" oxygen abundance were a perfect monotonic function of M_*. The scatter in the empirical strong-line metallicity calibration, estimated by PP04 to be $\simeq 0.18$ dex for N2 and $\simeq 0.14$ dex for O3N2, both *exceed* the inferred intrinsic MZR scatter of $\simeq 0.10$ dex. We showed in section 4.5 that the calibration errors of the N2 and O3N2 methods can be reduced compared to the numbers given by PP04 by restricting the range of line index included in the linear fit. *However, even the reduced calibration uncertainties would still account for 100% of the observed scatter in the MZR even if M_* were perfectly correlated with oxygen abundance.* Taken at face value, this suggests that the relative intensities of the strong emission lines, which we have argued are modulated primarily by ionization parameter and by the hardness of the UV radiation field, must be *more strongly* correlated with M_* than is the oxygen abundance. We will return to the possible implications of this "M_*-excitation" relation in section 8 below.

At $z \simeq 0$, the scatter in the correlation between M_* and metallicity can be reduced significantly by including an additional parameter that accounts indirectly for the cold gas content of the galaxies, most commonly using the SFR. A parametrization of this dependence of the form

$$12+\log(O/H) \propto \mu_* \equiv \log M_* - \alpha \log(SFR/M_\odot yr^{-1}) \, , \quad (22)$$

where α is a constant that minimizes the scatter in metallicity at a given μ_*, was introduced by Mannucci et al. (2010) as a convenient "projection" of what they called the "fundamental metallicity relation" (FMR). According to Mannucci et al. (2010), the FMR is a thin two-dimensional surface in the space defined by M_*, Z, and SFR, upon which all star-forming galaxies lie, independent of redshift for $z \lesssim 2.5$. To first order, the projection of the FMR parametrized by equation 22 accounts for the clearly observed trend (at $z \simeq 0$) that galaxies with higher SFR have lower gas-phase oxygen abundances at fixed M_*. In the context of the FMR, high redshift galaxies, known to have much higher gas fractions and SFRs than most local star-forming galaxies (e.g., Erb et al. 2006c; Daddi et al. 2010; Tacconi et al. 2010, 2013), would also be expected to have correspondingly lower (O/H) at a given M_*. Thus, the value of α in equation 22 adjusts the actual M_* to the mass μ_* expected for a galaxy with $\log(SFR/M_\odot yr^{-1}) = 0$ and the observed metallicity. For this form of the projected FMR, Mannucci et al. (2010) found that $\alpha = 0.32$ minimized the scatter in their $z \sim 0$ sample. An even stronger dependence on SFR of the M_*-Z relation has been suggested by Andrews & Martini (2013), who found $\alpha = 0.66$ for a local galaxy sample whose oxygen abundances were determined using the "direct" method.

However, the typical $z \sim 2.3$ galaxy in our sample has SFR $\simeq 25$ $M_\odot$ yr^{-1} (Figure 4), well beyond the range of SFR well-sampled by the $z \sim 0$ data set used by Mannucci et al. (2010) and near the high SFR extreme of the $z \simeq 0$ sample used by Andrews & Martini (2013). Thus, the assumption that the correlation between SFR and gas-phase metallicity extends over the elevated SFR range of the high redshift samples would require a significant (and uncertain) extrapolation. We defer a detailed discussion of the relationships among M_*, SFR, and inferred oxygen abundance in the KBSS sample to future work, for which we plan updates and improvements to the stellar population parameters (benefiting from additional and recently-obtained ancillary data), extinction estimates, and object-by-object slit loss corrections, as well as increased sample size and dynamic range.

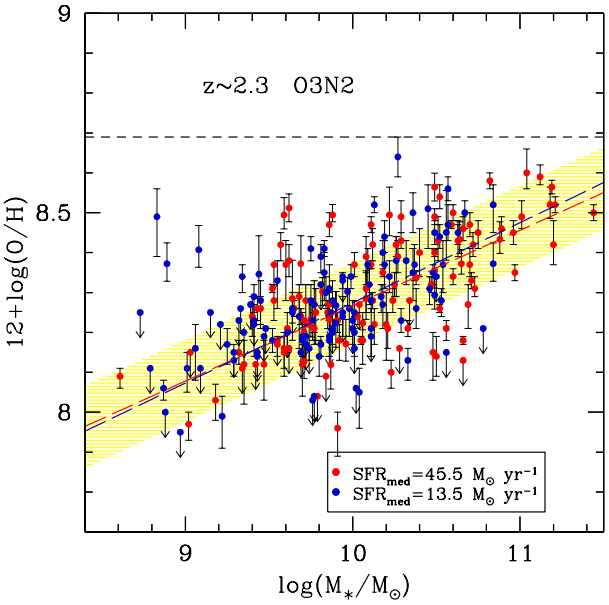

FIG. 25.— Same as the lefthand panel of Figure 24, but here individual points are color-coded according to whether the galaxy has SFR above or below the sample median, 25.5 $M_\odot yr^{-1}$; the median SFR of each sub-sample is indicated in the legend. Each sub-sample includes 121 galaxies, and the best-fit linear MZR (dashed lines) are color-coded in the same way. The shaded region shows the linear regression for the full sample (with parameters listed in equation 21), with width given by the inferred intrinsic scatter (at a given M_*) relative to the linear fit. The parameter estimates listed in equations 23 and 24 are statistically indistinguishable from one another, and compared to the full sample.

7.3. *The SFR Dependence of the MZR at $z \simeq 2.3$*

Within the current KBSS-MOSFIRE sample, dependence of the MZR relation on SFR must be subtle, if present (see also Wuyts et al. 2014; Sanders et al. 2014). Figure 25 shows the O3N2-determined MZR (as in the lefthand panel of Figure 24), but where the sample has been color-coded according

to whether the SFR lies above or below the median SFR of 25.5 $M_\odot yr^{-1}$. The two sub-samples, with median SFRs of 13.5 and 45.5 $M_\odot yr^{-1}$, were each fitted independently using the same functional form (equation 19) that produced the parameters listed in equation 21. Note that the overlap in M_* for the low-SFR and high-SFR subsamples is substantial, in spite of the well-known overall trend of higher SFR at higher M_*. The fits for the two SFR-based sub-samples are remarkably similar in normalization, slope, and intrinsic scatter, despite the factor of $\simeq 3.4$ difference in median SFR:

$$SFR_{low} : Z_{10} = 8.27 \pm 0.01;\ \ \gamma = 0.20 \pm 0.03; \qquad (23)$$
$$\sigma_{sc} = 0.11 \pm 0.01$$
$$SFR_{high} : Z_{10} = 8.27 \pm 0.01;\ \ \gamma = 0.19 \pm 0.02; . \qquad (24)$$
$$\sigma_{sc} = 0.10 \pm 0.01.$$

The two different best-fit linear relationships are over-plotted in Figure 25; clearly they are nearly identical to that of the full sample (equation 21 and Figure 24, shaded region in Figure 25.) and to one another.

At first glance this result implies that metallicity and SFR are not strongly linked at $z \simeq 2.3$, at least among galaxies in the observed range of M_* and SFR in our current sample. More generally, as will be detailed elsewhere (Strom et al 2014, in preparation), we have thus far not been able to identify a model in which inclusion of SFR as an additional parameter significantly reduces the scatter in the $z \sim 2.3$ MZR.

8. SUMMARY AND DISCUSSION

We have presented near-IR spectroscopy for an initial sample of 251 star-forming galaxies with $2.0 \leq z \leq 2.6$ observed in the 15 fields of the Keck Baryonic Structure Survey. All spectra were obtained using MOSFIRE, the recently-commissioned near-IR multi-object spectrometer on the Keck 1 10m telescope, during the first 18 months of its operation. In addition to the large size of the galaxy sample, the quality of the spectra of individual galaxies is much higher, and the dynamic range within the sample much larger, than has been possible to achieve previously. In this paper, we have explored the quantitative use of the strong nebular emission lines in the rest-frame optical spectra of high-redshift galaxies, re-examining their utility for diagnosing the physical conditions in galaxies during the peak of their most active star-forming phase. The main conclusions are as follows:

1. At $z \sim 2.3$, galaxies occupy an almost entirely distinct, but similarly tight, locus in the BPT diagram compared to the vast majority of star-forming galaxies in the local universe (Figure 5). The shift in the observed locus can be qualitatively explained if essentially all high-redshift H II regions are characterized by both harder ionizing radiation fields and higher ionization parameters than apply for all but the most extreme local galaxies.

2. Since all strong-line metallicity indicators and their calibrations are "tuned" to reproduce the tight sequence in the BPT diagram for local galaxies, the shift of the high redshift locus means that the same calibrations among the strong-line indicators cannot be used at high redshift without introducing systematics in the metallicity scale. Since ground-based observations are confined to redshift intervals within which particular strong nebular lines fall in the near-IR atmospheric windows, galaxy samples at different redshifts will necessarily depend on different subsets of the strong lines. It is entirely possible, perhaps even likely, that calibration issues could mimic global changes in metallicity or other physical conditions in HII regions with redshift. As an example, we show that metallicities inferred from the N2 and O3N2 indices of $z \sim 2.3$ galaxies differ systematically from each other, with an offset that averages $\simeq 0.13$ dex, in the sense that N2-inferred metallicities are higher (Figure 6).

3. Using simple photoionization models (with minimal assumptions about the details of the ionizing sources) we find that the observed locus of $z \sim 2.3$ galaxies in the BPT diagram, as well as the behavior of the N2 and O3N2 indices with respect to one another, can be reproduced remarkably well if the shape of the net ionizing radiation field in high-redshift HII regions resembles a blackbody with effective temperature $T_{eff} = 50000 - 60000$ K and ionization parameter in the range $-2.9 \lesssim \log\Gamma \lesssim -1.8$ (Figures 9 and 10). In the context of the models, most of the variation along the principle axis of the BPT locus is produced by changes in Γ, while the overall normalization of [OIII]/Hβ is modulated primarily by the effective temperature of the ionizing radiation field. For the high inferred level of ionization, a galaxy's position in BPT space is nearly independent of the ionized gas metallicity over the range $0.2 \leq Z/Z_\odot \leq 1.0$– *so that any observed metallicity dependence of the strong-line ratios is more likely caused by correlations between the radiation field shape and intensity with the metallicity of the stars themselves.* In addition, we find the $z = 2.3$ BPT locus is most easily reproduced if the (N/O) ratio in the ionized gas is close to the solar ratio over the full observed range of (O/H). Such high N/O, as well as high T_{eff}, may both be a consequence of the effects of binaries and rapid rotation on massive main sequence stars. Such effects are predicted to be greatly enhanced at the sub-solar metallicities that appear to be the rule at high redshift.

4. The KBSS-MOSFIRE sample contains a small number of AGN (Figures 17 and 18), most of which had been previously identified based on emission lines of high ionization species in their rest-frame UV spectra. The positions of AGN on the BPT diagram (Figure 5) appear distinct from the vast majority of objects which show no evidence in their rest-UV, rest-optical, or other multi-wavelength measurements for energetically significant contamination by AGN. The highest-excitation star-forming galaxies in the KBSS-MOSFIRE sample exhibit a maximum $\log([OIII]\lambda 5008/H\beta) \simeq 0.9$, consistent with the predictions of the photoionization models with UV ionizing radiation field in the 1-4 Ryd range resembling a blackbody with $T_{eff} = 55000 - 60000$ K and $\log\Gamma \gtrsim -2.0$ (Figure 9). This upper envelope appears to be the same for the most extreme star-forming galaxies in the local universe, where they are many orders of magnitude rarer.

5. We have drawn attention to the similarities between the most extreme galaxies (in terms of their position on the BPT diagram) in the $z \sim 0$ and $z \sim 2.3$ samples. In particular, the so-called "green pea" galaxies at $z \simeq 0.2$ appear to have strong line ratios placing them directly on the $z \sim 2.3$ BPT locus, while the "extreme green peas" are coincident with the highest excitation galaxies observed in the $z \simeq 2.3$ sample. Comparison of the published samples of green peas having accurate direct (T_e) metallicity measurements with the $z \sim 2.3$ galaxies is also interesting. The strong-line metallicity indices of the GPs follow the same trend as observed among the $z \sim 2.3$ sample and as predicted by our photoionization models (cf. Figure 6, 10, and 20). The corresponding direct measures of oxygen abundances for the GPs and a small subset of the $z \sim 2.3$ sample suggest that among the commonly-applied strong-line calibrations, the least-biased with respect to the di-

rect (T_e) metallicity measurements is O3N2. The differences in N2- and O3N2-based oxygen abundances described above imply that N2 generally over-estimates metallicities at $z \sim 2.3$ (by ~ 0.13 dex for $0.2-1.0$ $Z_\odot$.). The systematic differences can be reduced considerably (but not entirely eliminated) by restricting the low-redshift calibration data sets to the range of line indices observed among the high redshift sample (Figure 15.) We propose a simple empirical relation for converting 12+log(O/H)$_{N2}$ to the corresponding O3N2-based value appropriate at $z \sim 2.3$.

6. As shown previously using stacked spectra (Erb et al. 2006a), there is a relationship between M_* and the strong-line indices (N2 or O3N2) in place at $z \sim 2.3$ qualitatively similar to those observed at $z \simeq 0$ (Figures 23 and 24). If one converts the observed line indices into oxygen abundances using the locally-established calibrations (i.e., under the assumption that the line indices can be used to measure metallicity), the best-fit $z \sim 2.3$ MZR is somewhat *shallower* than some previous studies have suggested, $12+\log(O/H) \propto 0.20\ [\log(M_*/M_\odot)-10]$ using either N2 or O3N2 indices. Both versions of the MZR are consistent with the same linear behavior over the range of M_* observed. (Figures 23 and 24.) As for the locus in the BPT diagram, the intrinsic scatter in the MZR (i.e., scatter of inferred metallicity at a given M_*) is both small and remarkably similar at $z \sim 2.3$ and $z \sim 0$ when the same metallicity calibration is applied to both: $\sigma_{sc} \simeq 0.10$ dex. Over the well-covered range of M_* observed in the current $z \sim 2.3$ KBSS-MOSFIRE sample ($9 \lesssim \log(M_*/M_\odot) \lesssim 11$), there is no obvious M_* dependence of the MZR scatter.

7. We have pointed out that the small values inferred for the *intrinsic* scatter in the $z \sim 2.3$ MZR ($\sigma \simeq 0.10$ dex) is uncomfortably small compared with the minimum uncertainties inherent in the calibrations of the strong-line metallicity methods, even when the latter are re-calibrated only over the range of line indices covered by the $z \sim 2.3$ observations. When taken together with the photoionization models showing that the observed line ratios at $z \sim 2.3$ are more strongly affected by ionizing radiation field intensity and shape than by ionized gas metallicity, it suggests that the more fundamental correlation (of which the MZR is a by-product) is between M$*$ and the properties of the massive stars that determine the ionization/excitation state of the gas in their surroundings.

8. We investigated briefly whether there is evidence within our sample for a dependence (at fixed stellar mass) between inferred oxygen abundance and SFR as observed in the local universe. We find nearly identical best-fit MZR relations (normalization, slope, and intrinsic scatter) for independent sub-samples (121 galaxies each) median SFRs differing by a factor of $\simeq 3.4$. *At present, over the range spanned by our current $z \sim 2.3$ sample, inferred oxygen abundances appear to be independent of SFR at a given stellar mass.*

8.1. *Implications and Future Work*

Among the issues raised, we regard the following as unresolved and particularly interesting to pursue with future work:

8.1.1. *Metallicity measurements at high redshift*

There is currently very limited evidence that *any* strong-line abundance estimates at high redshift reliably measure gas-phase metallicity, as is universally assumed. However, the prospects for improving the situation are good, since instruments now exist (like MOSFIRE) capable of obtaining sufficiently sensitive spectra of high redshift galaxies to measure weak lines such as [OIII]λ4364 whose strengths relative to strong lines provide direct information on physical conditions in the ionized gas. We have shown that it should be feasible to obtain such measurements at $z \sim 2.3$ for individual galaxies with metallicities as high as $Z \sim 0.5\ Z_\odot$; it may be possible, using spectral stacks, to extend the calibrations to higher metallicity (see, e.g., Andrews & Martini 2013). Because of the remaining uncertainty associated with converting strong-line ratios to oxygen abundance, until direct metallicity cross-checks have been completed, we suggest that galaxies should not be "pre-screened" for deep follow-up based on their strong-line-implied abundances (see section 6). One should also obtain, wherever possible, measurements of the rest-UV OIII] intercombination lines available from deep ground-based optical spectroscopy (section 6.1), which in some cases may be more sensitive, albeit more dependent on nebular extinction corrections, than measurement of [OIII]λ4364 in the rest-frame optical.

8.1.2. *The dominant ionizing sources in high-redshift H II regions*

In order to temporarily avoid uncertainties associated with the details of the predicted ionizing spectra of massive stars in high-redshift galaxies, we have modeled the net radiation field shape using a single-temperature blackbody, which can be thought of as the effective temperature of whatever stars are dominating the radiation field for photon energies between 1 and 4 Ryd. It appears that successful population synthesis models used for future more detailed models of the ionized gas in $z \sim 2.3$ galaxies must be capable of producing, in steady state, a net luminosity-weighted spectrum resembling a $\simeq 50,000-60,000$ K blackbody in the far-UV. This may have implications for the high-mass end of the stellar initial mass function (IMF), as well as for the details of the models for the most massive stars. Satisfying the constraint that the stars must produce nebulae with the observed properties may also have implications for the production and transfer of ionizing photons from young galaxies at high redshift.

8.1.3. *The slope and normalization of the MZR at $z \sim 2.3$*

According to our preferred form of the $z \sim 2.3$ MZR presented in section 7, the average metallicity of the dominant star-forming galaxy population changes by only $\lesssim 0.5$ dex over more than 2.5 orders of magnitude in M$*$, $8.6 \lesssim \log(M_*/M_\odot) \sim 11.4$. This shallow dependence of (strong-line-inferred) metallicity on stellar mass ($12+\log(O/H) \propto 0.20\ \log M_*$) is comparable to what is observed *over the same range in M_** at $z \simeq 0$. Because the strong nebular lines appear to be relatively *insensitive* to the ionized gas metallicity, one should be cautious in treating inferred oxygen abundances as direct indications of metallicity in the dominant gas reservoirs of galaxies. Similarly, one should also be cautious interpreting changes in strong-line ratios (e.g., as a function of position within galaxies, or scatter among galaxies of similar stellar mass) as differences in *gas-phase* metallicity– they are perhaps more likely to signal changes in the ionizing sources and their distribution, which may have a different origin.

8.1.4. *Fundamental correlations between nebular line ratios and galaxy properties*

As discussed in section 7.2, the tightness of the relationship between inferred oxygen abundance and M_* is difficult to understand given the uncertainties in the calibration of the strong

line indices onto direct (T_e) based oxygen abundance. The observed relationship is more easily understood if a) there is a relatively narrow range of radiation field effective temperature across all galaxy masses probed in the current sample and b) there is a monotonic relationship between effective ionization parameter Γ and M_*. Understanding *why* ionization level and excitation are so strongly linked to galaxy mass is a key goal for future work.

This work has been supported in part by the US National Science Foundation through grants AST-0908805 and AST-1313472 (CCS), as well as by an NSF Graduate Student Research Fellowship (ALS). The MOSFIRE instrument was made possible by grants to the W.M. Keck Observatory from the NSF "Telescope System Instrumentation Program" (TSIP) and by a generous donation from Gordon and Betty Moore. We thank our colleagues on the MOSFIRE instrument team, particularly Marcia Brown, Khan Bui, John Cromer, Jason Fucik, Hector Rodriguez, Bob Weber, and Jeff Zolkower at Caltech, Ted Aliado, George Brims, John Canfield, Chris Johnson, Ken Magnone, and Jason Weiss at UCLA, Harland Epps at UCO/Lick Observatory, and Sean Adkins at WMKO. Special thanks to all of the WMKO staff who helped make MOSFIRE commissioning successful, especially Marc Kassis, Allan Honey, Greg Wirth, Shui Kwok, Liz Chock, and Jim Lyke. We benefited significantly from an illuminating discussion on the subject of massive stars with Selma de Mink. Constructive comments from the anonymous referee, which led to significant improvements in the content and presentation of the results, are gratefully acknowledged. Finally, we wish to extend thanks to those of Hawaiian ancestry on whose sacred mountain we are privileged to be guests.

REFERENCES

Adelberger, K. L., Steidel, C. C., Shapley, A. E., et al. 2004, ApJ, 607, 226
Amorín, R., Pérez-Montero, E., Vílchez, J. M., & Papaderos, P. 2012, ApJ, 749, 185
Amorín, R., Grazian, A., Castellano, M., et al. 2014, ApJ, 788, L4
Amorín, R. O., Pérez-Montero, E., & Vílchez, J. M. 2010, ApJ, 715, L128
Andrews, B. H., & Martini, P. 2013, ApJ, 765, 140
Asplund, M., Grevesse, N., Sauval, A. J., & Scott, P. 2009, ARA&A, 47, 481
Baldwin, J. A., Phillips, M. M., & Terlevich, R. 1981, PASP, 93, 5
Bayliss, M. B., Rigby, J. R., Sharon, K., et al. 2013, ArXiv e-prints, arXiv:1310.6695
Brinchmann, J., Pettini, M., & Charlot, S. 2008, MNRAS, 385, 769
Brott, I., de Mink, S. E., Cantiello, M., et al. 2011, A&A, 530, A115
Bruzual, G., & Charlot, S. 2003, MNRAS, 344, 1000
Calzetti, D., Armus, L., Bohlin, R. C., et al. 2000, ApJ, 533, 682
Cardamone, C., Schawinski, K., Sarzi, M., et al. 2009, MNRAS, 399, 1191
Cardelli, J. A., Clayton, G. C., & Mathis, J. S. 1989, ApJ, 345, 245
Chabrier, G. 2003, PASP, 115, 763
Charlot, S., & Longhetti, M. 2001, MNRAS, 323, 887
Christensen, L., Laursen, P., Richard, J., et al. 2012, MNRAS, 427, 1973
Cullen, F., Cirasuolo, M., McLure, R. J., Dunlop, J. S., & Bowler, R. A. A. 2014, MNRAS, 440, 2300
Daddi, E., Bournaud, F., Walter, F., et al. 2010, ApJ, 713, 686
Dopita, M. A., Kewley, L. J., Heisler, C. A., & Sutherland, R. S. 2000, ApJ, 542, 224
Dopita, M. A., Sutherland, R. S., Nicholls, D. C., Kewley, L. J., & Vogt, F. P. A. 2013, ApJS, 208, 10
Eldridge, J. J., & Stanway, E. R. 2009, MNRAS, 400, 1019, 1019
—. 2012, MNRAS, 419, 479
Erb, D. K., Pettini, M., Shapley, A. E., et al. 2010, ApJ, 719, 1168
Erb, D. K., Shapley, A. E., Pettini, M., et al. 2006a, ApJ, 644, 813
Erb, D. K., Shapley, A. E., Steidel, C. C., et al. 2003, ApJ, 591, 101
Erb, D. K., Steidel, C. C., Shapley, A. E., Pettini, M., & Adelberger, K. L. 2004, ApJ, 612, 122
Erb, D. K., Steidel, C. C., Shapley, A. E., et al. 2006b, ApJ, 647, 128
—. 2006c, ApJ, 646, 107
Esteban, C., Peimbert, M., García-Rojas, J., et al. 2004, MNRAS, 355, 229
Ferland, G. J., Porter, R. L., van Hoof, P. A. M., et al. 2013, RMxAA, 49, 137
Finkelstein, S. L., Papovich, C., Rudnick, G., et al. 2009, ApJ, 700, 376
Förster Schreiber, N. M., Genzel, R., Bouché, N., et al. 2009, ApJ, 706, 1364
Förster Schreiber, N. M., Genzel, R., Newman, S. F., et al. 2014, ApJ, 787, 38
Genzel, R., Förster Schreiber, N. M., Rosario, D., et al. 2014, ArXiv e-prints, arXiv:1406.0183
Gordon, K. D., Clayton, G. C., Misselt, K. A., Landolt, A. U., & Wolff, M. J. 2003, ApJ, 594, 279
Hainline, K. N., Shapley, A. E., Greene, J. E., & Steidel, C. C. 2011, ApJ, 733, 31
Hainline, K. N., Shapley, A. E., Greene, J. E., et al. 2012, ApJ, 760, 74
Hainline, K. N., Shapley, A. E., Kornei, K. A., et al. 2009, ApJ, 701, 52
Henry, A., Scarlata, C., Domínguez, A., et al. 2013, ApJ, 776, L27
Henry, R. B. C., & Worthey, G. 1999, PASP, 111, 919
Iwata, I., Inoue, A. K., Matsuda, Y., et al. 2009, ApJ, 692, 1287
James, B. L., Pettini, M., Christensen, L., et al. 2014, MNRAS, arXiv:1311.5092
Jaskot, A. E., & Oey, M. S. 2013, ApJ, 766, 91
Jones, T., Ellis, R. S., Richard, J., & Jullo, E. 2013, ApJ, 765, 48
Jones, T. A., Swinbank, A. M., Ellis, R. S., Richard, J., & Stark, D. P. 2010, MNRAS, 404, 1247
Juneau, S., Bournaud, F., Charlot, S., et al. 2014, ApJ, 788, 88
Kauffmann, G., Heckman, T. M., Tremonti, C., et al. 2003, MNRAS, 346, 1055
Kelly, B. C. 2007, ApJ, 665, 1489
Kelson, D. D. 2003, PASP, 115, 688
Kennicutt, R. C. 1998, ARA&A, 36, 189
Kewley, L. J., & Dopita, M. A. 2002, ApJS, 142, 35
Kewley, L. J., Dopita, M. A., Leitherer, C., et al. 2013a, ApJ, 774, 100
Kewley, L. J., Dopita, M. A., Sutherland, R. S., Heisler, C. A., & Trevena, J. 2001, ApJ, 556, 121
Kewley, L. J., & Ellison, S. L. 2008, ApJ, 681, 1183
Kewley, L. J., Maier, C., Yabe, K., et al. 2013b, ApJ, 774, L10
Kobulnicky, H. A., Kennicutt, Jr., R. C., & Pizagno, J. L. 1999, ApJ, 514, 544
Kobulnicky, H. A., & Kewley, L. J. 2004, ApJ, 617, 240
Kriek, M., van Dokkum, P. G., Franx, M., et al. 2008, ApJ, 677, 219
Kudritzki, R.-P., & Puls, J. 2000, ARA&A, 38, 613
Kulas, K. R., McLean, I. S., Shapley, A. E., et al. 2013, ApJ, 774, 130
Law, D. R., Steidel, C. C., Erb, D. K., et al. 2009, ApJ, 697, 2057
Law, D. R., Steidel, C. C., Shapley, A. E., et al. 2012, ApJ, 745, 85
Levesque, E. M., Leitherer, C., Ekstrom, S., Meynet, G., & Schaerer, D. 2012, ApJ, 751, 67
Liu, X., Shapley, A. E., Coil, A. L., Brinchmann, J., & Ma, C.-P. 2008, ApJ, 678, 758
Madau, P., Pozzetti, L., & Dickinson, M. 1998, ApJ, 498, 106
Maiolino, R., Nagao, T., Grazian, A., et al. 2008, A&A, 488, 463
Mannucci, F., Cresci, G., Maiolino, R., Marconi, A., & Gnerucci, A. 2010, MNRAS, 408, 2115
Massey, P., Puls, J., Pauldrach, A. W. A., et al. 2005, ApJ, 627, 477
Masters, D., McCarthy, P., Siana, B., et al. 2014, ApJ, 785, 153
McGaugh, S. S. 1991, ApJ, 380, 140
McLean, I. S., Steidel, C. C., Epps, H., et al. 2010, in Society of Photo-Optical Instrumentation Engineers (SPIE) Conference Series, Vol. 7735, Society of Photo-Optical Instrumentation Engineers (SPIE) Conference Series
McLean, I. S., Steidel, C. C., Epps, H. W., et al. 2012, in Society of Photo-Optical Instrumentation Engineers (SPIE) Conference Series, Vol. 8446, Society of Photo-Optical Instrumentation Engineers (SPIE) Conference Series
Mostardi, R. E., Shapley, A. E., Nestor, D. B., Steidel, C. C., & Reddy, N. A. 2013, ArXiv e-prints, arXiv:1306.1535
Moustakas, J., Zaritsky, D., Brown, M., et al. 2011, ArXiv e-prints, arXiv:1112.3300
Nestor, D. B., Shapley, A. E., Steidel, C. C., & Siana, B. 2011, ApJ, 736, 18
Newman, S. F., Buschkamp, P., Genzel, R., et al. 2013, ArXiv e-prints, arXiv:1306.6676
Pagel, B. E. J., Edmunds, M. G., Blackwell, D. E., Chun, M. S., & Smith, G. 1979, MNRAS, 189, 95

Pérez-Montero, E., & Contini, T. 2009, MNRAS, 398, 949
Pettini, M., Kellogg, M., Steidel, C. C., et al. 1998, ApJ, 508, 539
Pettini, M., & Pagel, B. E. J. 2004, MNRAS, 348, L59
Pettini, M., Shapley, A. E., Steidel, C. C., et al. 2001, ApJ, 554, 981
Pettini, M., Zych, B. J., Steidel, C. C., & Chaffee, F. H. 2008, MNRAS, 385, 2011
Pilyugin, L. S., Grebel, E. K., & Mattsson, L. 2012, MNRAS, 424, 2316
Price, S. H., Kriek, M., Brammer, G. B., et al. 2013, ArXiv e-prints, arXiv:1310.4177
Rakic, O., Schaye, J., Steidel, C. C., & Rudie, G. C. 2012, ApJ, 751, 94
Reddy, N., Dickinson, M., Elbaz, D., et al. 2012a, ApJ, 744, 154
Reddy, N. A., Erb, D. K., Pettini, M., Steidel, C. C., & Shapley, A. E. 2010, ApJ, 712, 1070
Reddy, N. A., Pettini, M., Steidel, C. C., et al. 2012b, ApJ, 754, 25
Reddy, N. A., & Steidel, C. C. 2004, ApJ, 603, L13
Reddy, N. A., Steidel, C. C., Pettini, M., et al. 2008, ApJS, 175, 48
Richard, J., Jones, T., Ellis, R., et al. 2011, MNRAS, 413, 643
Rigby, J. R., Wuyts, E., Gladders, M. D., Sharon, K., & Becker, G. D. 2011, ApJ, 732, 59
Rudie, G. C., Steidel, C. C., Trainor, R. F., et al. 2012, ApJ, 750, 67
Salpeter, E. E. 1955, ApJ, 121, 161
Sanders, R. L., Shapley, A. E., Kriek, M., et al. 2014, ArXiv e-prints, arXiv:1408.2521
Shapley, A. E., Coil, A. L., Ma, C.-P., & Bundy, K. 2005a, ApJ, 635, 1006
Shapley, A. E., Erb, D. K., Pettini, M., Steidel, C. C., & Adelberger, K. L. 2004, ApJ, 612, 108
Shapley, A. E., Steidel, C. C., Erb, D. K., et al. 2005b, ApJ, 626, 698
Shields, G. A., & Tinsley, B. M. 1976, ApJ, 203, 66
Shirazi, M., Brinchmann, J., & Rahmati, A. 2013, ArXiv e-prints, arXiv:1307.4758
Stasińska, G. 2005, A&A, 434, 507
Steidel, C. C., Adelberger, K. L., Shapley, A. E., et al. 2003, ApJ, 592, 728
Steidel, C. C., Erb, D. K., Shapley, A. E., et al. 2010, ApJ, 717, 289
Steidel, C. C., Hunt, M. P., Shapley, A. E., et al. 2002, ApJ, 576, 653
Steidel, C. C., Shapley, A. E., Pettini, M., et al. 2004, ApJ, 604, 534
Tacconi, L. J., Genzel, R., Neri, R., et al. 2010, Nature, 463, 781
Tacconi, L. J., Neri, R., Genzel, R., et al. 2013, ApJ, 768, 74
Teplitz, H. I., McLean, I. S., Becklin, E. E., et al. 2000, ApJ, 533, L65
Trainor, R. F., & Steidel, C. C. 2012, ApJ, 752, 39
Tremonti, C. A., Heckman, T. M., Kauffmann, G., et al. 2004, ApJ, 613, 898
Troncoso, P., Maiolino, R., Sommariva, V., et al. 2014, A&A, 563, A58
Turner, M. L., Schaye, J., Steidel, C. C., Rudie, G. C., & Strom, A. L. 2014, ArXiv e-prints, arXiv:1403.0942
van Zee, L., Salzer, J. J., & Haynes, M. P. 1998, ApJ, 497, L1
Veilleux, S., & Osterbrock, D. E. 1987, ApJS, 63, 295
Verdolini, S., Yeh, S. C. C., Krumholz, M. R., Matzner, C. D., & Tielens, A. G. G. M. 2013, ApJ, 769, 12
Vila Costas, M. B., & Edmunds, M. G. 1993, MNRAS, 265, 199
Villar-Martín, M., Cerviño, M., & González Delgado, R. M. 2004, MNRAS, 355, 1132
Wright, S. A., Larkin, J. E., Graham, J. R., & Ma, C.-P. 2010, ApJ, 711, 1291
Wuyts, E., Rigby, J. R., Sharon, K., & Gladders, M. D. 2012, ApJ, 755, 73
Wuyts, E., Kurk, J., Förster Schreiber, N. M., et al. 2014, ApJ, 789, L40
Yeh, S. C. C., Verdolini, S., Krumholz, M. R., Matzner, C. D., & Tielens, A. G. G. M. 2013, ApJ, 769, 11
Yuan, T.-T., & Kewley, L. J. 2009, ApJ, 699, L161
Zahid, H. J., Dima, G. I., Kudritzki, R.-P., et al. 2014, ApJ, 791, 130

TABLE 1
KBSS-MOSFIRE GALAXIES WITH BOTH [NII]/Hα AND [OIII]/Hβ MEASUREMENTS

Name	z_{neb}	log M$_*$ (M$_\odot$)	log([NII]/Hα)	log([OIII]/Hβ)	12+log(O/H) (N2)[b]	12+log(O/H) (O3N2)[c]	Notes
Q0100-BX118	2.1093	9.22	$-1.57^{+0.24}_{-0.15}$	$0.74^{+0.05}_{-0.05}$	$8.01^{+0.14}_{-0.09}$	$7.99^{+0.05}_{-0.08}$	1
Q0100-BX163	2.2985	10.32	$-0.88^{+0.16}_{-0.12}$	$0.22^{+0.11}_{-0.09}$	$8.40^{+0.09}_{-0.07}$	$8.38^{+0.05}_{-0.06}$	1a
Q0100-BX172	2.3118	...	$-0.79^{+0.05}_{-0.05}$	$0.97^{+0.01}_{-0.01}$	$8.45^{+0.03}_{-0.03}$	$8.17^{+0.02}_{-0.02}$	A1,1
Q0100-BX205	2.2912	9.88	$-1.00^{+0.10}_{-0.08}$	$0.66^{+0.03}_{-0.03}$	$8.33^{+0.06}_{-0.05}$	$8.20^{+0.03}_{-0.03}$	
Q0100-BX210	2.2769	10.10	$-0.79^{+0.16}_{-0.12}$	$0.49^{+0.05}_{-0.05}$	$8.45^{+0.09}_{-0.07}$	$8.32^{+0.04}_{-0.05}$	1
Q0100-BX224	2.1076	9.40	$-0.90^{+0.15}_{-0.11}$	$0.64^{+0.09}_{-0.08}$	$8.38^{+0.08}_{-0.06}$	$8.24^{+0.05}_{-0.05}$	1a
Q0100-BX277	2.1061	10.18	$-0.98^{+0.18}_{-0.13}$	$0.46^{+0.07}_{-0.06}$	$8.34^{+0.10}_{-0.07}$	$8.27^{+0.05}_{-0.06}$	1
Q0100-BX88	2.5241	9.60	$-0.83^{+0.27}_{-0.17}$	$0.31^{+0.09}_{-0.08}$	$8.43^{+0.16}_{-0.09}$	$8.37^{+0.06}_{-0.09}$	1
Q0100-BX90	2.2850	9.92	$-0.96^{+0.13}_{-0.10}$	$0.76^{+0.07}_{-0.06}$	$8.35^{+0.08}_{-0.06}$	$8.18^{+0.04}_{-0.05}$	1
Q0100-BX95	2.2097	10.27	$-0.75^{+0.08}_{-0.07}$	$0.31^{+0.09}_{-0.08}$	$8.47^{+0.05}_{-0.04}$	$8.39^{+0.04}_{-0.04}$	
Q0100-MD19	2.1078	10.27	$-0.45^{+0.11}_{-0.09}$	$-0.16^{+0.14}_{-0.10}$	$8.64^{+0.07}_{-0.05}$	$8.64^{+0.05}_{-0.05}$	1a
Q0100-RK17	2.1076	11.44	$-0.39^{+0.02}_{-0.02}$	$0.34^{+0.07}_{-0.06}$	$8.68^{+0.01}_{-0.01}$	$8.50^{+0.02}_{-0.02}$	
Q0100-RK21	2.0624	10.51	$-0.34^{+0.10}_{-0.08}$	$0.60^{+0.17}_{-0.12}$	$8.70^{+0.06}_{-0.05}$	$8.43^{+0.06}_{-0.05}$	
Q0105-BX132	2.2115	10.75	$-0.62^{+0.10}_{-0.08}$	$0.25^{+0.06}_{-0.06}$	$8.55^{+0.06}_{-0.05}$	$8.45^{+0.03}_{-0.04}$	1
Q0105-BX147	2.3857	9.41	$-0.77^{+0.13}_{-0.10}$	$0.60^{+0.04}_{-0.03}$	$8.46^{+0.08}_{-0.06}$	$8.29^{+0.03}_{-0.04}$	1
Q0105-BX186	2.2003	10.57	$-0.44^{+0.07}_{-0.06}$	$0.36^{+0.13}_{-0.10}$	$8.65^{+0.04}_{-0.04}$	$8.47^{+0.05}_{-0.04}$	1a
Q0105-BX57	2.2589	9.86	$-0.89^{+0.05}_{-0.05}$	$0.55^{+0.07}_{-0.06}$	$8.40^{+0.03}_{-0.03}$	$8.27^{+0.03}_{-0.03}$	1
Q0105-BX58	2.5351	...	$-0.16^{+0.08}_{-0.07}$	$0.77^{+0.11}_{-0.09}$	$8.81^{+0.05}_{-0.04}$	$8.43^{+0.04}_{-0.04}$	A1,1
Q0105-BX77	2.2930	10.01	$-0.91^{+0.19}_{-0.13}$	$0.75^{+0.03}_{-0.03}$	$8.38^{+0.11}_{-0.08}$	$8.20^{+0.04}_{-0.06}$	1a
Q0105-BX79	2.1229	10.52	$-0.40^{+0.06}_{-0.05}$	$0.52^{+0.09}_{-0.08}$	$8.67^{+0.03}_{-0.03}$	$8.44^{+0.03}_{-0.03}$	1a
Q0105-MD27	2.0623	10.36	$-0.29^{+0.11}_{-0.09}$	$0.44^{+0.12}_{-0.09}$	$8.74^{+0.06}_{-0.05}$	$8.50^{+0.05}_{-0.05}$	1a
Q0142-BX122	2.4177	9.53	$-0.99^{+0.15}_{-0.11}$	$0.41^{+0.02}_{-0.02}$	$8.33^{+0.08}_{-0.06}$	$8.28^{+0.04}_{-0.05}$	1
Q0142-BX169	2.2824	10.20	$-0.82^{+0.24}_{-0.16}$	$0.79^{+0.18}_{-0.13}$	$8.43^{+0.14}_{-0.09}$	$8.22^{+0.08}_{-0.09}$	1
Q0142-BX188	2.0602	9.84	$-0.72^{+0.10}_{-0.08}$	$0.64^{+0.09}_{-0.08}$	$8.49^{+0.06}_{-0.05}$	$8.30^{+0.04}_{-0.04}$	1a
Q0142-BX195	2.3804	...	$-0.49^{+0.09}_{-0.08}$	$0.94^{+0.15}_{-0.11}$	$8.62^{+0.05}_{-0.04}$	$8.27^{+0.06}_{-0.05}$	A1,1
Q0142-BX196	2.4918	9.55	$-0.68^{+0.20}_{-0.14}$	$0.58^{+0.06}_{-0.05}$	$8.51^{+0.11}_{-0.08}$	$8.33^{+0.05}_{-0.07}$	1
Q0142-BX214	2.3865	9.70	$-1.09^{+0.15}_{-0.11}$	$0.59^{+0.02}_{-0.02}$	$8.28^{+0.09}_{-0.06}$	$8.19^{+0.04}_{-0.05}$	1
Q0142-BX242	2.2812	9.68	$-0.87^{+0.10}_{-0.08}$	$0.52^{+0.03}_{-0.03}$	$8.40^{+0.06}_{-0.05}$	$8.29^{+0.03}_{-0.03}$	1
Q0142-BX40	2.3924	10.84	$-0.36^{+0.23}_{-0.15}$	$0.29^{+0.06}_{-0.05}$	$8.70^{+0.13}_{-0.08}$	$8.52^{+0.05}_{-0.07}$	1a
Q0142-BX75	2.4175	9.94	$-0.80^{+0.20}_{-0.14}$	$0.70^{+0.02}_{-0.02}$	$8.44^{+0.11}_{-0.08}$	$8.25^{+0.04}_{-0.06}$	1
Q0142-BX81	2.5026	9.45	$-0.90^{+0.12}_{-0.10}$	$0.57^{+0.02}_{-0.02}$	$8.38^{+0.07}_{-0.05}$	$8.26^{+0.03}_{-0.04}$	1
Q0142-MD20	2.5007	9.57	$-0.59^{+0.11}_{-0.09}$	$0.39^{+0.03}_{-0.03}$	$8.56^{+0.06}_{-0.05}$	$8.42^{+0.03}_{-0.04}$	1a
Q0207-BX150	2.1147	10.37	$-0.73^{+0.08}_{-0.07}$	$0.39^{+0.13}_{-0.10}$	$8.49^{+0.05}_{-0.04}$	$8.37^{+0.05}_{-0.04}$	1a
Q0207-BX155	2.1536	8.83	$-0.65^{+0.28}_{-0.17}$	$0.11^{+0.16}_{-0.12}$	$8.53^{+0.16}_{-0.10}$	$8.49^{+0.07}_{-0.10}$	1
Q0207-BX285	2.1504	9.77	$-0.96^{+0.21}_{-0.14}$	$0.48^{+0.11}_{-0.09}$	$8.35^{+0.12}_{-0.08}$	$8.27^{+0.06}_{-0.07}$	1
Q0207-BX37	2.0901	9.81	$-0.68^{+0.10}_{-0.08}$	$0.38^{+0.07}_{-0.06}$	$8.51^{+0.06}_{-0.05}$	$8.39^{+0.03}_{-0.04}$	1
Q0207-BX65	2.1920	10.19	$-0.72^{+0.15}_{-0.11}$	$0.40^{+0.15}_{-0.11}$	$8.49^{+0.08}_{-0.06}$	$8.37^{+0.06}_{-0.06}$	
Q0207-BX67	2.1954	9.77	$-1.16^{+0.11}_{-0.09}$	$0.46^{+0.09}_{-0.07}$	$8.24^{+0.06}_{-0.05}$	$8.21^{+0.04}_{-0.04}$	1
Q0207-BX74	2.1889	9.02	$-1.46^{+0.11}_{-0.09}$	$0.90^{+0.05}_{-0.05}$	$8.07^{+0.06}_{-0.05}$	$7.97^{+0.03}_{-0.04}$	1
Q0207-BX87	2.1924	10.04	$-1.28^{+0.28}_{-0.17}$	$0.83^{+0.05}_{-0.05}$	$8.17^{+0.16}_{-0.10}$	$8.05^{+0.06}_{-0.09}$	1
Q0207-MD39	2.5252	9.78	$-0.90^{+0.24}_{-0.15}$	$0.58^{+0.08}_{-0.07}$	$8.39^{+0.14}_{-0.09}$	$8.25^{+0.06}_{-0.08}$	1
Q0449-BX128	2.4604	10.06	$-1.10^{+0.20}_{-0.14}$	$0.63^{+0.02}_{-0.02}$	$8.27^{+0.11}_{-0.08}$	$8.18^{+0.04}_{-0.06}$	1
Q0449-BX40	2.4008	10.52	$-0.52^{+0.06}_{-0.06}$	$0.09^{+0.06}_{-0.05}$	$8.60^{+0.04}_{-0.03}$	$8.54^{+0.03}_{-0.03}$	1
Q0449-BX68	2.4972	9.75	$-0.68^{+0.15}_{-0.11}$	$0.72^{+0.04}_{-0.03}$	$8.51^{+0.09}_{-0.06}$	$8.28^{+0.04}_{-0.05}$	1
Q0449-BX70	2.4775	9.86	$-0.75^{+0.25}_{-0.16}$	$0.56^{+0.08}_{-0.07}$	$8.47^{+0.14}_{-0.09}$	$8.31^{+0.06}_{-0.08}$	1
Q0449-BX84	2.2971	9.76	$-0.83^{+0.16}_{-0.11}$	$0.73^{+0.07}_{-0.06}$	$8.43^{+0.09}_{-0.07}$	$8.23^{+0.04}_{-0.05}$	1
Q0449-BX92	2.4021	10.54	$-0.47^{+0.21}_{-0.14}$	$0.65^{+0.10}_{-0.08}$	$8.63^{+0.12}_{-0.08}$	$8.37^{+0.06}_{-0.07}$	1
Q0449-M10	2.3863	10.72	$-0.58^{+0.09}_{-0.08}$	$0.39^{+0.05}_{-0.05}$	$8.57^{+0.05}_{-0.04}$	$8.42^{+0.03}_{-0.03}$	1
Q0821-BX101	2.4462	10.87	$-0.11^{+0.03}_{-0.03}$	$0.79^{+0.11}_{-0.09}$	$8.84^{+0.02}_{-0.02}$	$8.44^{+0.04}_{-0.03}$	A2
Q0821-BX102	2.4151	9.91	$-1.62^{+0.21}_{-0.14}$	$0.79^{+0.01}_{-0.01}$	$7.97^{+0.12}_{-0.08}$	$7.96^{+0.04}_{-0.07}$	1
Q0821-BX207	2.4133	9.59	$-1.20^{+0.15}_{-0.11}$	$0.58^{+0.01}_{-0.01}$	$8.22^{+0.09}_{-0.06}$	$8.16^{+0.04}_{-0.05}$	1
Q0821-BX45	2.1800	10.66	$-1.08^{+0.03}_{-0.03}$	$0.64^{+0.02}_{-0.02}$	$8.28^{+0.02}_{-0.02}$	$8.18^{+0.01}_{-0.01}$	1a
Q0821-BX47	2.4612	9.25	$-0.89^{+0.14}_{-0.10}$	$0.85^{+0.03}_{-0.03}$	$8.39^{+0.08}_{-0.06}$	$8.17^{+0.04}_{-0.05}$	1
Q0821-BX72	2.3511	11.20	$-0.53^{+0.12}_{-0.09}$	$0.44^{+0.16}_{-0.12}$	$8.60^{+0.07}_{-0.05}$	$8.42^{+0.06}_{-0.05}$	
Q0821-BX77	2.2942	9.61	$-0.97^{+0.18}_{-0.12}$	$0.65^{+0.03}_{-0.03}$	$8.35^{+0.10}_{-0.07}$	$8.21^{+0.04}_{-0.06}$	1
Q0821-BX80	2.4448	10.25	$-0.77^{+0.09}_{-0.07}$	$0.53^{+0.04}_{-0.04}$	$8.46^{+0.05}_{-0.04}$	$8.32^{+0.03}_{-0.03}$	1a
Q0821-D10	2.5178	9.98	$-0.93^{+0.22}_{-0.15}$	$0.53^{+0.04}_{-0.03}$	$8.37^{+0.13}_{-0.08}$	$8.26^{+0.05}_{-0.07}$	1
Q0821-D8	2.5675	...	$-0.36^{+0.09}_{-0.08}$	$0.93^{+0.04}_{-0.04}$	$8.69^{+0.05}_{-0.04}$	$8.32^{+0.03}_{-0.03}$	A1,1
Q0821-MD38	2.0918	10.49	$-0.56^{+0.03}_{-0.03}$	$0.20^{+0.07}_{-0.06}$	$8.58^{+0.02}_{-0.02}$	$8.49^{+0.02}_{-0.02}$	
Q0821-RK27	2.4483	10.08	$-0.72^{+0.20}_{-0.14}$	$0.34^{+0.10}_{-0.08}$	$8.49^{+0.12}_{-0.08}$	$8.39^{+0.05}_{-0.07}$	
Q0821-RK29	2.4681	10.71	$-0.78^{+0.07}_{-0.06}$	$0.46^{+0.02}_{-0.02}$	$8.46^{+0.04}_{-0.04}$	$8.33^{+0.02}_{-0.02}$	

TABLE 1
KBSS-MOSFIRE GALAXIES WITH BOTH [NII]/Hα AND [OIII]/Hβ MEASUREMENTS (*cont.*)

Name	z_{neb}	log M_* ($M_\odot$)	log([NII]/Hα)	log([OIII]/Hβ)	12+log(O/H) (N2)[b]	12+log(O/H) (O3N2)[c]	Notes
Q1009-BX146	2.2681	10.29	$-0.69^{+0.04}_{-0.04}$	$0.25^{+0.05}_{-0.05}$	$8.51^{+0.02}_{-0.02}$	$8.43^{+0.02}_{-0.02}$	1
Q1009-BX215	2.5056	10.26	$-0.69^{+0.08}_{-0.07}$	$0.28^{+0.04}_{-0.03}$	$8.51^{+0.04}_{-0.04}$	$8.42^{+0.02}_{-0.03}$	1,6
Q1009-BX218	2.1090	10.38	$-0.96^{+0.12}_{-0.09}$	$0.51^{+0.11}_{-0.09}$	$8.35^{+0.07}_{-0.05}$	$8.26^{+0.05}_{-0.05}$	1
Q1009-MD36	2.5048	10.70	$-0.64^{+0.08}_{-0.06}$	$0.18^{+0.05}_{-0.05}$	$8.54^{+0.04}_{-0.04}$	$8.47^{+0.03}_{-0.03}$	1
Q1009-MD39	2.1425	11.04	$-0.41^{+0.06}_{-0.05}$	$0.01^{+0.17}_{-0.12}$	$8.67^{+0.03}_{-0.03}$	$8.60^{+0.06}_{-0.04}$	1a
Q1217-BX102	2.1936	9.75	$-0.57^{+0.09}_{-0.07}$	$0.42^{+0.06}_{-0.05}$	$8.57^{+0.05}_{-0.04}$	$8.41^{+0.03}_{-0.03}$	1
Q1217-BX164	2.3310	9.72	$-0.77^{+0.12}_{-0.10}$	$0.63^{+0.09}_{-0.07}$	$8.46^{+0.07}_{-0.05}$	$8.28^{+0.04}_{-0.05}$	1
Q1217-BX193	2.2164	9.86	$-1.07^{+0.15}_{-0.11}$	$0.61^{+0.03}_{-0.03}$	$8.29^{+0.08}_{-0.06}$	$8.19^{+0.04}_{-0.05}$	1
Q1217-BX95	2.4244	10.23	$-1.22^{+0.11}_{-0.09}$	$0.76^{+0.01}_{-0.01}$	$8.21^{+0.06}_{-0.05}$	$8.10^{+0.03}_{-0.04}$	1
Q1217-MD13	2.3826	10.48	$-1.20^{+0.20}_{-0.14}$	$0.60^{+0.09}_{-0.08}$	$8.22^{+0.11}_{-0.08}$	$8.15^{+0.05}_{-0.07}$	1
Q1217-MD15	2.1272	10.22	$-0.78^{+0.10}_{-0.08}$	$0.45^{+0.11}_{-0.09}$	$8.46^{+0.06}_{-0.05}$	$8.34^{+0.04}_{-0.04}$	1
Q1442-BX108	2.4280	9.69	$-1.04^{+0.08}_{-0.07}$	$0.48^{+0.01}_{-0.01}$	$8.31^{+0.04}_{-0.04}$	$8.24^{+0.02}_{-0.02}$	1
Q1442-BX116	2.0463	9.74	$-1.05^{+0.27}_{-0.17}$	$0.55^{+0.05}_{-0.05}$	$8.30^{+0.16}_{-0.09}$	$8.22^{+0.06}_{-0.09}$	1
Q1442-BX133	2.1053	9.68	$-0.98^{+0.24}_{-0.15}$	$0.57^{+0.11}_{-0.09}$	$8.34^{+0.14}_{-0.09}$	$8.24^{+0.06}_{-0.08}$	1
Q1442-BX160	2.4418	9.55	$-1.10^{+0.08}_{-0.07}$	$0.66^{+0.01}_{-0.01}$	$8.27^{+0.05}_{-0.04}$	$8.17^{+0.02}_{-0.03}$	1
Q1442-BX172	2.4496	10.08	$-0.95^{+0.19}_{-0.13}$	$0.37^{+0.04}_{-0.04}$	$8.36^{+0.11}_{-0.08}$	$8.31^{+0.04}_{-0.06}$	1
Q1442-BX235	2.4443	10.60	$-0.70^{+0.05}_{-0.05}$	$0.53^{+0.02}_{-0.02}$	$8.50^{+0.03}_{-0.03}$	$8.34^{+0.02}_{-0.02}$	1
Q1442-BX270	2.3578	9.52	$-0.98^{+0.10}_{-0.08}$	$0.74^{+0.01}_{-0.01}$	$8.34^{+0.06}_{-0.05}$	$8.18^{+0.03}_{-0.03}$	
Q1442-BX277	2.3125	10.01	$-0.87^{+0.11}_{-0.09}$	$0.63^{+0.03}_{-0.03}$	$8.41^{+0.06}_{-0.05}$	$8.25^{+0.03}_{-0.04}$	1
Q1442-BX350	2.4422	10.11	$-0.90^{+0.20}_{-0.14}$	$0.72^{+0.04}_{-0.04}$	$8.39^{+0.11}_{-0.08}$	$8.21^{+0.05}_{-0.07}$	1
Q1442-BX351	2.4518	10.13	$-0.97^{+0.14}_{-0.11}$	$0.62^{+0.03}_{-0.03}$	$8.34^{+0.08}_{-0.06}$	$8.22^{+0.04}_{-0.05}$	1
Q1442-BX69	2.0888	10.53	$-0.73^{+0.12}_{-0.09}$	$0.69^{+0.03}_{-0.03}$	$8.48^{+0.07}_{-0.05}$	$8.28^{+0.03}_{-0.04}$	1
Q1442-BX69b	2.1489	10.13	$-0.47^{+0.04}_{-0.04}$	$0.19^{+0.03}_{-0.03}$	$8.63^{+0.02}_{-0.02}$	$8.52^{+0.02}_{-0.02}$	
Q1442-C18	2.3166	10.40	$-0.83^{+0.13}_{-0.10}$	$0.19^{+0.16}_{-0.11}$	$8.43^{+0.07}_{-0.06}$	$8.40^{+0.06}_{-0.06}$	1
Q1442-MD13	2.4528	10.56	$-0.90^{+0.09}_{-0.07}$	$0.72^{+0.01}_{-0.01}$	$8.39^{+0.05}_{-0.04}$	$8.21^{+0.02}_{-0.03}$	1a
Q1442-MD53	2.2926	10.96	$-0.41^{+0.05}_{-0.04}$	$0.47^{+0.10}_{-0.08}$	$8.67^{+0.03}_{-0.02}$	$8.45^{+0.03}_{-0.03}$	1
Q1442-MD57	2.4440	9.86	$-0.38^{+0.07}_{-0.06}$	$0.44^{+0.06}_{-0.05}$	$8.68^{+0.04}_{-0.03}$	$8.47^{+0.03}_{-0.03}$	
Q1549-BX101	2.3806	...	$-0.38^{+0.03}_{-0.03}$	$0.80^{+0.02}_{-0.02}$	$8.68^{+0.02}_{-0.01}$	$8.35^{+0.01}_{-0.01}$	A2
Q1549-BX127	2.5336	9.35	$-1.16^{+0.30}_{-0.18}$	$0.74^{+0.05}_{-0.05}$	$8.24^{+0.17}_{-0.10}$	$8.12^{+0.06}_{-0.10}$	1
Q1549-BX180	2.3870	9.32	$-1.18^{+0.09}_{-0.08}$	$0.61^{+0.01}_{-0.01}$	$8.23^{+0.05}_{-0.04}$	$8.15^{+0.03}_{-0.03}$	1
Q1549-BX197	2.4351	9.62	$-0.75^{+0.10}_{-0.08}$	$0.35^{+0.08}_{-0.07}$	$8.48^{+0.06}_{-0.05}$	$8.38^{+0.04}_{-0.04}$	1
Q1549-BX207	2.3802	9.65	$-0.93^{+0.06}_{-0.05}$	$0.54^{+0.02}_{-0.02}$	$8.37^{+0.03}_{-0.03}$	$8.26^{+0.02}_{-0.02}$	1
Q1549-BX221	2.3407	9.43	$-0.80^{+0.08}_{-0.07}$	$0.66^{+0.07}_{-0.06}$	$8.44^{+0.05}_{-0.04}$	$8.26^{+0.03}_{-0.03}$	1a
Q1549-BX223	2.3492	9.52	$-0.79^{+0.03}_{-0.03}$	$0.52^{+0.01}_{-0.01}$	$8.45^{+0.02}_{-0.02}$	$8.31^{+0.01}_{-0.01}$	1
Q1549-BX227	2.0573	10.69	$-0.92^{+0.16}_{-0.11}$	$0.52^{+0.09}_{-0.07}$	$8.37^{+0.09}_{-0.07}$	$8.27^{+0.05}_{-0.06}$	1
Q1549-BX240	2.0412	10.63	$-0.55^{+0.05}_{-0.05}$	$0.33^{+0.08}_{-0.07}$	$8.59^{+0.03}_{-0.03}$	$8.45^{+0.03}_{-0.03}$	1a
Q1549-BX45	2.0645	9.83	$-0.66^{+0.22}_{-0.15}$	$0.54^{+0.08}_{-0.07}$	$8.52^{+0.13}_{-0.08}$	$8.35^{+0.05}_{-0.07}$	1
Q1549-BX51	2.2895	9.72	$-1.14^{+0.18}_{-0.13}$	$0.54^{+0.05}_{-0.04}$	$8.25^{+0.10}_{-0.07}$	$8.19^{+0.04}_{-0.06}$	1,6
Q1603-BX101	2.3202	10.29	$-0.39^{+0.09}_{-0.07}$	$0.37^{+0.11}_{-0.09}$	$8.68^{+0.05}_{-0.04}$	$8.49^{+0.04}_{-0.04}$	
Q1603-BX106	2.2743	9.34	$-0.81^{+0.11}_{-0.09}$	$0.42^{+0.05}_{-0.04}$	$8.44^{+0.06}_{-0.05}$	$8.34^{+0.03}_{-0.04}$	
Q1603-BX173	2.5490	9.01	$-1.07^{+0.18}_{-0.13}$	$0.86^{+0.04}_{-0.04}$	$8.29^{+0.10}_{-0.07}$	$8.11^{+0.04}_{-0.06}$	1
Q1603-BX190	2.0216	10.01	$-0.81^{+0.07}_{-0.06}$	$0.33^{+0.05}_{-0.05}$	$8.44^{+0.04}_{-0.04}$	$8.37^{+0.03}_{-0.03}$	1
Q1603-BX191	2.5446	10.42	$-0.35^{+0.04}_{-0.04}$	$1.04^{+0.05}_{-0.05}$	$8.70^{+0.02}_{-0.02}$	$8.28^{+0.02}_{-0.02}$	A2
Q1603-BX255	2.4349	10.21	$-1.09^{+0.14}_{-0.11}$	$0.53^{+0.03}_{-0.03}$	$8.28^{+0.08}_{-0.06}$	$8.21^{+0.04}_{-0.05}$	1
Q1603-BX277	2.5499	9.91	$-0.92^{+0.08}_{-0.07}$	$0.66^{+0.02}_{-0.02}$	$8.38^{+0.04}_{-0.04}$	$8.23^{+0.02}_{-0.03}$	1
Q1603-BX294	2.4510	10.03	$-0.96^{+0.05}_{-0.05}$	$0.57^{+0.01}_{-0.01}$	$8.36^{+0.03}_{-0.03}$	$8.24^{+0.01}_{-0.02}$	1
Q1603-BX379	2.1768	10.11	$-0.61^{+0.04}_{-0.03}$	$0.21^{+0.04}_{-0.04}$	$8.55^{+0.02}_{-0.02}$	$8.47^{+0.02}_{-0.02}$	1
Q1603-MD26	2.5511	9.85	$-0.99^{+0.12}_{-0.09}$	$0.50^{+0.02}_{-0.02}$	$8.34^{+0.07}_{-0.05}$	$8.25^{+0.03}_{-0.04}$	1
Q1603-MD42	2.3806	9.99	$-0.70^{+0.07}_{-0.06}$	$0.51^{+0.06}_{-0.05}$	$8.50^{+0.04}_{-0.03}$	$8.34^{+0.03}_{-0.03}$	1
Q1603-MD45	2.3858	10.09	$-0.82^{+0.16}_{-0.12}$	$0.30^{+0.06}_{-0.05}$	$8.43^{+0.09}_{-0.07}$	$8.37^{+0.04}_{-0.05}$	1
Q1603-MD50	2.4326	10.70	$-0.63^{+0.06}_{-0.05}$	$0.49^{+0.10}_{-0.08}$	$8.54^{+0.04}_{-0.03}$	$8.37^{+0.04}_{-0.03}$	1
Q1603-MD85	2.4507	10.48	$-0.65^{+0.08}_{-0.07}$	$0.53^{+0.04}_{-0.04}$	$8.53^{+0.04}_{-0.04}$	$8.35^{+0.02}_{-0.03}$	1
Q1623-BX366	2.4204	10.12	$-0.66^{+0.10}_{-0.08}$	$0.31^{+0.08}_{-0.06}$	$8.52^{+0.06}_{-0.05}$	$8.42^{+0.04}_{-0.04}$	1,4,6
Q1623-BX428	2.0542	10.45	$-0.51^{+0.29}_{-0.17}$	$0.17^{+0.06}_{-0.05}$	$8.61^{+0.17}_{-0.10}$	$8.51^{+0.06}_{-0.10}$	1,2,4,6
Q1623-BX429	2.0159	9.94	$-0.94^{+0.04}_{-0.04}$	$0.31^{+0.06}_{-0.05}$	$8.36^{+0.02}_{-0.02}$	$8.33^{+0.02}_{-0.02}$	1,4,6
Q1623-BX447	2.1480	10.67	$-0.78^{+0.11}_{-0.09}$	$-0.06^{+0.06}_{-0.06}$	$8.45^{+0.06}_{-0.05}$	$8.50^{+0.03}_{-0.04}$	1,2,4,6,7
Q1623-BX449	2.4180	10.26	$-0.79^{+0.27}_{-0.17}$	$0.30^{+0.10}_{-0.08}$	$8.45^{+0.16}_{-0.09}$	$8.38^{+0.06}_{-0.09}$	2,4,6
Q1623-BX452	2.0584	10.57	$-0.47^{+0.06}_{-0.06}$	$0.07^{+0.06}_{-0.05}$	$8.63^{+0.04}_{-0.03}$	$8.56^{+0.03}_{-0.03}$	1,6
Q1623-BX453	2.1820	10.59	$-0.48^{+0.02}_{-0.01}$	$0.32^{+0.02}_{-0.02}$	$8.63^{+0.01}_{-0.01}$	$8.47^{+0.01}_{-0.01}$	1,4,5,6,10
Q1623-BX472	2.1141	10.46	$-0.93^{+0.12}_{-0.09}$	$0.39^{+0.04}_{-0.04}$	$8.37^{+0.07}_{-0.05}$	$8.31^{+0.03}_{-0.04}$	1,4,6

TABLE 1
KBSS-MOSFIRE GALAXIES WITH BOTH [NII]/Hα AND [OIII]/Hβ MEASUREMENTS (*cont.*)

Name	z_{neb}	log M_* ($M_\odot$)	log([NII]/Hα)	log([OIII]/Hβ)	12+log(O/H) (N2)[b]	12+log(O/H) (O3N2)[c]	Notes
Q1700-BX490	2.3958	10.05	$-0.98^{+0.03}_{-0.03}$	$0.73^{+0.01}_{-0.01}$	$8.34^{+0.02}_{-0.02}$	$8.18^{+0.01}_{-0.01}$	1,3,4,5,6
Q1700-BX505	2.3083	10.66	$-0.47^{+0.06}_{-0.05}$	$0.37^{+0.07}_{-0.06}$	$8.63^{+0.03}_{-0.03}$	$8.46^{+0.03}_{-0.03}$	1,3,4,6
Q1700-BX563	2.2910	10.33	$-0.94^{+0.05}_{-0.05}$	$0.67^{+0.02}_{-0.02}$	$8.37^{+0.03}_{-0.03}$	$8.21^{+0.02}_{-0.02}$	1,3
Q1700-BX585	2.3066	9.06	$-1.20^{+0.24}_{-0.15}$	$0.58^{+0.08}_{-0.07}$	$8.21^{+0.13}_{-0.09}$	$8.16^{+0.06}_{-0.08}$	1,3
Q1700-BX625	2.0752	9.80	$-1.18^{+0.15}_{-0.11}$	$0.66^{+0.04}_{-0.03}$	$8.23^{+0.08}_{-0.06}$	$8.14^{+0.04}_{-0.05}$	1,3
Q1700-BX649	2.2946	10.18	$-0.78^{+0.06}_{-0.05}$	$0.26^{+0.08}_{-0.06}$	$8.46^{+0.03}_{-0.03}$	$8.40^{+0.03}_{-0.03}$	1
Q1700-BX691	2.1891	10.89	$-0.71^{+0.05}_{-0.04}$	$0.12^{+0.09}_{-0.07}$	$8.49^{+0.03}_{-0.02}$	$8.46^{+0.03}_{-0.03}$	1,2,3,4
Q1700-BX708	2.3992	9.70	$-1.15^{+0.23}_{-0.15}$	$0.75^{+0.04}_{-0.04}$	$8.24^{+0.13}_{-0.09}$	$8.12^{+0.05}_{-0.08}$	1,4,6
Q1700-BX710	2.2946	10.52	$-0.90^{+0.03}_{-0.03}$	$0.59^{+0.02}_{-0.02}$	$8.39^{+0.02}_{-0.02}$	$8.26^{+0.01}_{-0.01}$	1,5
Q1700-BX711	2.2947	8.61	$-1.21^{+0.08}_{-0.07}$	$0.80^{+0.02}_{-0.02}$	$8.21^{+0.05}_{-0.04}$	$8.09^{+0.02}_{-0.03}$	1
Q1700-BX713	2.1381	9.64	$-1.03^{+0.20}_{-0.14}$	$0.48^{+0.06}_{-0.05}$	$8.32^{+0.11}_{-0.08}$	$8.25^{+0.05}_{-0.07}$	
Q1700-BX752	2.4001	10.60	$-0.57^{+0.05}_{-0.05}$	$0.16^{+0.04}_{-0.04}$	$8.57^{+0.03}_{-0.03}$	$8.50^{+0.02}_{-0.02}$	1a
Q1700-BX763	2.2919	10.11	$-0.85^{+0.07}_{-0.06}$	$0.57^{+0.03}_{-0.03}$	$8.41^{+0.04}_{-0.04}$	$8.28^{+0.02}_{-0.03}$	1,5,6
Q1700-BX879	2.3065	9.88	$-0.71^{+0.06}_{-0.06}$	$0.06^{+0.29}_{-0.17}$	$8.49^{+0.04}_{-0.03}$	$8.48^{+0.10}_{-0.06}$	1,3
Q1700-BX913	2.2905	10.24	$-0.83^{+0.09}_{-0.07}$	$0.57^{+0.06}_{-0.05}$	$8.43^{+0.05}_{-0.04}$	$8.28^{+0.03}_{-0.03}$	1,6
Q1700-BX917	2.3066	10.73	$-0.84^{+0.05}_{-0.04}$	$0.47^{+0.07}_{-0.06}$	$8.42^{+0.03}_{-0.02}$	$8.31^{+0.03}_{-0.02}$	1,3,4,6
Q1700-BX951	2.3053	10.49	$-0.67^{+0.07}_{-0.06}$	$0.22^{+0.06}_{-0.05}$	$8.52^{+0.04}_{-0.04}$	$8.45^{+0.03}_{-0.03}$	1
Q1700-BX984	2.2967	10.19	$-0.89^{+0.10}_{-0.08}$	$0.03^{+0.10}_{-0.08}$	$8.39^{+0.05}_{-0.04}$	$8.44^{+0.04}_{-0.04}$	1,3
Q1700-MD109	2.2936	9.88	$-0.97^{+0.23}_{-0.15}$	$0.45^{+0.07}_{-0.06}$	$8.35^{+0.13}_{-0.08}$	$8.28^{+0.05}_{-0.08}$	1,2,3,4,6
Q1700-MD69	2.2881	11.21	$-0.47^{+0.03}_{-0.03}$	$0.20^{+0.05}_{-0.04}$	$8.63^{+0.02}_{-0.02}$	$8.52^{+0.02}_{-0.02}$	1,3,4
Q1700-MD77	2.5078	9.47	$-1.13^{+0.28}_{-0.17}$	$0.78^{+0.06}_{-0.05}$	$8.26^{+0.16}_{-0.10}$	$8.12^{+0.06}_{-0.09}$	1a
Q2206-BX140	2.3517	10.00	$-0.91^{+0.19}_{-0.13}$	$0.66^{+0.07}_{-0.06}$	$8.38^{+0.11}_{-0.08}$	$8.23^{+0.05}_{-0.06}$	1
Q2206-BX145	2.2349	9.45	$-0.75^{+0.21}_{-0.14}$	$0.66^{+0.06}_{-0.05}$	$8.47^{+0.12}_{-0.08}$	$8.28^{+0.05}_{-0.07}$	1
Q2206-BX168	2.1966	9.70	$-1.06^{+0.13}_{-0.10}$	$0.50^{+0.27}_{-0.17}$	$8.30^{+0.08}_{-0.06}$	$8.23^{+0.09}_{-0.07}$	1
Q2206-BX189	2.0779	11.01	$-0.46^{+0.05}_{-0.05}$	$0.27^{+0.12}_{-0.09}$	$8.64^{+0.03}_{-0.03}$	$8.49^{+0.04}_{-0.03}$	1
Q2206-BX191	2.1575	10.50	$-1.12^{+0.15}_{-0.10}$	$0.72^{+0.11}_{-0.09}$	$8.26^{+0.07}_{-0.06}$	$8.14^{+0.05}_{-0.05}$	1a
Q2206-BX88	2.1806	10.29	$-0.89^{+0.07}_{-0.06}$	$0.67^{+0.05}_{-0.05}$	$8.39^{+0.04}_{-0.03}$	$8.23^{+0.03}_{-0.03}$	1
Q2343-BX182	2.2876	9.81	$-1.12^{+0.09}_{-0.07}$	$0.63^{+0.03}_{-0.03}$	$8.26^{+0.05}_{-0.04}$	$8.17^{+0.02}_{-0.03}$	1,4,6
Q2343-BX222	2.2872	10.63	$-0.56^{+0.06}_{-0.05}$	$0.40^{+0.12}_{-0.09}$	$8.58^{+0.03}_{-0.03}$	$8.43^{+0.04}_{-0.04}$	1
Q2343-BX231	2.4989	10.11	$-0.58^{+0.02}_{-0.02}$	$0.54^{+0.03}_{-0.03}$	$8.57^{+0.01}_{-0.01}$	$8.37^{+0.01}_{-0.01}$	1
Q2343-BX336	2.5445	10.12	$-0.86^{+0.06}_{-0.05}$	$0.53^{+0.01}_{-0.01}$	$8.41^{+0.04}_{-0.03}$	$8.28^{+0.02}_{-0.02}$	1,4,6
Q2343-BX348	2.4491	10.49	$-0.62^{+0.02}_{-0.02}$	$0.41^{+0.01}_{-0.01}$	$8.54^{+0.01}_{-0.01}$	$8.40^{+0.01}_{-0.01}$	1
Q2343-BX389	2.1711	10.97	$-0.75^{+0.04}_{-0.04}$	$0.43^{+0.06}_{-0.05}$	$8.47^{+0.02}_{-0.02}$	$8.35^{+0.02}_{-0.02}$	1,6,7
Q2343-BX418	2.3054	8.87	$-1.28^{+0.08}_{-0.07}$	$0.81^{+0.02}_{-0.02}$	$8.17^{+0.05}_{-0.04}$	$8.06^{+0.02}_{-0.03}$	1,4,5,6,8
Q2343-BX442	2.1752	11.12	$-0.52^{+0.03}_{-0.03}$	$-0.08^{+0.08}_{-0.07}$	$8.60^{+0.02}_{-0.02}$	$8.59^{+0.03}_{-0.02}$	1,4,6,9
Q2343-BX445	2.5445	9.69	$-0.84^{+0.06}_{-0.05}$	$0.68^{+0.01}_{-0.01}$	$8.42^{+0.04}_{-0.03}$	$8.24^{+0.02}_{-0.02}$	1
Q2343-BX460	2.3945	9.18	$-1.37^{+0.17}_{-0.12}$	$0.81^{+0.03}_{-0.02}$	$8.12^{+0.09}_{-0.07}$	$8.03^{+0.04}_{-0.05}$	1
Q2343-BX473	2.5437	10.33	$-1.18^{+0.14}_{-0.11}$	$0.70^{+0.02}_{-0.01}$	$8.23^{+0.08}_{-0.06}$	$8.13^{+0.03}_{-0.05}$	1
Q2343-BX480	2.2316	10.17	$-1.03^{+0.12}_{-0.09}$	$0.34^{+0.05}_{-0.05}$	$8.31^{+0.07}_{-0.05}$	$8.29^{+0.03}_{-0.04}$	1,4,6
Q2343-BX484	2.1874	10.36	$-0.88^{+0.20}_{-0.14}$	$0.32^{+0.13}_{-0.10}$	$8.40^{+0.11}_{-0.08}$	$8.35^{+0.06}_{-0.07}$	1
Q2343-BX496	2.3934	9.29	$-1.16^{+0.12}_{-0.10}$	$0.70^{+0.06}_{-0.05}$	$8.24^{+0.07}_{-0.05}$	$8.13^{+0.04}_{-0.04}$	1a
Q2343-BX537	2.3394	9.59	$-1.19^{+0.18}_{-0.12}$	$0.62^{+0.06}_{-0.05}$	$8.22^{+0.10}_{-0.07}$	$8.15^{+0.04}_{-0.06}$	1,4,6
Q2343-BX587	2.2427	10.18	$-0.67^{+0.02}_{-0.02}$	$0.50^{+0.04}_{-0.04}$	$8.52^{+0.01}_{-0.01}$	$8.35^{+0.01}_{-0.01}$	1,4
Q2343-BX601	2.3768	10.47	$-0.89^{+0.05}_{-0.04}$	$0.40^{+0.03}_{-0.03}$	$8.39^{+0.03}_{-0.02}$	$8.32^{+0.02}_{-0.02}$	1,4,6
Q2343-D29	2.3866	9.83	$-0.65^{+0.05}_{-0.05}$	$0.34^{+0.03}_{-0.03}$	$8.53^{+0.03}_{-0.03}$	$8.41^{+0.02}_{-0.02}$	1
Q2343-D35	2.3986	10.82	$-0.43^{+0.05}_{-0.04}$	$0.04^{+0.05}_{-0.05}$	$8.66^{+0.03}_{-0.02}$	$8.58^{+0.02}_{-0.02}$	1a
Q2343-MD86	2.3976	9.41	$-1.02^{+0.25}_{-0.16}$	$0.56^{+0.03}_{-0.03}$	$8.32^{+0.14}_{-0.09}$	$8.22^{+0.05}_{-0.08}$	1

[a] Error bars are 1σ based on measurement uncertainties only.
[b] Oxygen abundance assuming the "N2" calibration of PP04.
[c] Oxygen abundance assuming the "O3N2' calibration of PP04.
[A1] Object identified as an AGN on the basis of both rest-UV (LRIS-B) and rest-optical (MOSFIRE) spectra.
[A2] Object identified as an AGN on the basis of near-IR (MOSFIRE) spectra.
[1] Objects having optical (rest-UV) spectra obtained using Keck/LRIS-B; galaxies whose LRIS-B spectra yielded spectroscopic redshifts are marked "1", while "1a" denotes objects that were attempted spectroscopically in the rest-UV without yielding a secure redshift.
References to other spectroscopic/photometric measurements: (2) Erb et al. (2003) (3) Shapley et al. (2005b) (4) Erb et al. (2006c) (5) Law et al. (2009) (6) Steidel et al. (2010) (7) Förster Schreiber et al. (2009) (8) Erb et al. (2010) (9) Law et al. (2012) (10) Shapley et al. (2004)

TABLE 2
KBSS-MOSFIRE GALAXIES WITH [OIII]/Hβ MEASUREMENTS AND [NII]/Hα LIMITS[a]

Name	z_{neb}	log M_* ($M_\odot$)	log([NII]/Hα)	log([OIII]/Hβ)	12+log(O/H) (N2)[b]	12+log(O/H) (O3N2)[c]	Notes
Q0100-BX167	2.2894	9.39	< -0.98	$0.47^{+0.06}_{-0.06}$	< 8.34	< 8.27	
Q0100-BX185	2.3659	9.53	< -0.82	$0.32^{+0.17}_{-0.12}$	< 8.43	< 8.37	
Q0100-BX187	2.2660	9.03	< -1.01	$0.80^{+0.08}_{-0.07}$	< 8.32	< 8.15	1
Q0100-BX57	2.2706	9.41	< -0.86	$0.70^{+0.05}_{-0.04}$	< 8.41	< 8.23	1
Q0105-BX163	2.2912	10.01	< -1.05	$0.72^{+0.03}_{-0.03}$	< 8.30	< 8.16	1a
Q0105-BX49	2.1144	9.33	< -0.97	$0.51^{+0.08}_{-0.07}$	< 8.35	< 8.26	1
Q0105-BX89	2.2278	9.84	< -1.38	$0.62^{+0.04}_{-0.03}$	< 8.11	< 8.09	1
Q0105-MD12	2.5053	9.55	< -1.04	$0.67^{+0.02}_{-0.02}$	< 8.31	< 8.18	1a
Q0142-BX138	2.4177	9.48	< -0.94	$0.70^{+0.03}_{-0.03}$	< 8.37	< 8.21	1
Q0142-BX182	2.3555	10.78	< -0.92	$0.71^{+0.25}_{-0.16}$	< 8.38	< 8.21	1
Q0142-BX186	2.3568	8.79	< -0.90	$1.06^{+0.09}_{-0.08}$	< 8.39	< 8.11	A1,1
Q0142-BX212	2.3781	9.81	< -0.81	$0.48^{+0.04}_{-0.03}$	< 8.44	< 8.32	1a
Q0207-BX119	2.0588	10.28	< -1.23	$0.54^{+0.02}_{-0.02}$	< 8.20	< 8.16	1
Q0207-BX144	2.1682	8.88	< -1.50	$0.78^{+0.03}_{-0.03}$	< 8.05	< 8.00	1
Q0207-BX211	2.5468	9.71	< -1.10	$0.46^{+0.10}_{-0.08}$	< 8.27	< 8.23	
Q0207-BX243	2.0385	9.61	< -0.90	$0.75^{+0.04}_{-0.04}$	< 8.39	< 8.20	1
Q0449-BX138	2.3934	9.86	< -0.83	$0.89^{+0.12}_{-0.10}$	< 8.43	< 8.18	1
Q0821-BX221	2.3958	9.76	< -1.40	$0.78^{+0.02}_{-0.02}$	< 8.10	< 8.03	1
Q0821-BX52	2.1767	10.56	< -1.08	$0.74^{+0.09}_{-0.08}$	< 8.29	< 8.15	
Q0821-BX61	2.3526	9.87	< -0.89	$0.61^{+0.13}_{-0.10}$	< 8.39	< 8.25	
Q0821-BX92	2.4163	9.21	< -1.02	$0.59^{+0.04}_{-0.04}$	< 8.32	< 8.22	1
Q0821-MD5	2.5367	9.88	< -0.95	$0.68^{+0.03}_{-0.03}$	< 8.36	< 8.21	1
Q1009-BX155	2.1448	9.74	< -1.23	$0.55^{+0.06}_{-0.06}$	< 8.20	< 8.16	1
Q1009-BX177	2.0949	9.09	< -1.25	$0.70^{+0.19}_{-0.13}$	< 8.19	< 8.11	1
Q1217-BX220	2.3225	9.79	< -1.44	$0.71^{+0.03}_{-0.03}$	< 8.08	< 8.04	1
Q1442-BX138	2.4336	9.62	< -1.19	$0.59^{+0.04}_{-0.04}$	< 8.22	< 8.16	1
Q1442-BX199	2.2938	9.29	< -1.13	$0.69^{+0.03}_{-0.03}$	< 8.25	< 8.15	1
Q1442-BX290	2.4318	9.69	< -1.19	$0.61^{+0.05}_{-0.04}$	< 8.22	< 8.15	1
Q1442-BX295	2.4514	9.35	< -1.04	$0.62^{+0.03}_{-0.03}$	< 8.31	< 8.20	
Q1442-BX305	2.5165	9.71	< -0.88	$0.79^{+0.04}_{-0.04}$	< 8.40	< 8.20	1
Q1442-BX346	2.4473	9.43	< -1.08	$0.72^{+0.08}_{-0.07}$	< 8.28	< 8.15	1
Q1549-BX102	2.1934	9.43	< -1.11	$0.72^{+0.02}_{-0.02}$	< 8.27	< 8.14	1
Q1549-BX121	2.4983	8.73	< -0.92	$0.59^{+0.10}_{-0.08}$	< 8.38	< 8.25	1
Q1549-BX170	2.3836	9.77	< -1.43	$0.73^{+0.04}_{-0.04}$	< 8.09	< 8.04	1
Q1549-MD18	2.5116	10.00	< -0.87	$0.76^{+0.21}_{-0.14}$	< 8.41	< 8.21	1
Q1603-BX389	2.4266	10.66	< -1.26	$0.61^{+0.02}_{-0.02}$	< 8.18	< 8.13	1
Q1603-BX55	2.3706	9.42	< -1.24	$0.66^{+0.03}_{-0.03}$	< 8.19	< 8.12	1
Q1603-MD16	2.5475	10.34	< -0.97	$0.43^{+0.20}_{-0.13}$	< 8.35	< 8.28	1
Q1623-BX431	2.1127	9.15	< -0.95	$0.54^{+0.04}_{-0.04}$	< 8.36	< 8.25	1
Q1623-BX432	2.1824	10.02	< -1.44	$0.67^{+0.03}_{-0.02}$	< 8.08	< 8.06	1,2,4,6
Q1623-BX469	2.5499	9.32	< -0.98	$0.58^{+0.05}_{-0.05}$	< 8.34	< 8.23	1
Q1623-MD127	2.4592	9.94	< -0.80	$0.43^{+0.05}_{-0.04}$	< 8.44	< 8.34	1
Q1700-BX609	2.5697	9.64	< -0.96	$0.50^{+0.09}_{-0.07}$	< 8.35	< 8.26	1,3
Q1700-BX717	2.4358	9.47	< -1.05	$0.62^{+0.13}_{-0.10}$	< 8.30	< 8.19	1,2,3,4,6
Q1700-BX772	2.3416	9.72	< -1.11	$0.65^{+0.10}_{-0.08}$	< 8.27	< 8.17	1,3
Q2206-BM64	2.1942	9.34	< -1.19	$0.73^{+0.05}_{-0.04}$	< 8.22	< 8.11	1
Q2206-BX128	2.3484	10.04	< -0.95	$0.48^{+0.10}_{-0.08}$	< 8.36	< 8.27	1a
Q2343-BX236	2.4341	10.50	< -0.81	$0.41^{+0.23}_{-0.15}$	< 8.44	< 8.34	1,4,6
Q2343-BX660	2.1742	8.97	< -1.61	$0.81^{+0.02}_{-0.02}$	< 7.99	< 7.96	1,4,5,6
Q2343-D34	2.4538	10.11	< -1.02	$0.67^{+0.04}_{-0.04}$	< 8.32	< 8.19	1
Q2343-MD37	2.4246	9.94	< -0.97	$0.56^{+0.04}_{-0.03}$	< 8.34	< 8.24	1

[a] Upper limits on log([NII]/Hα) are 2σ; error bars are otherwise 1σ based on measurement errors only.

[b] 2σ upper limit on oxygen abundance assuming the "N2" calibration of PP04.

[c] 2σ upper limit on oxygen abundance assuming the "O3N2' calibration of PP04.

[A1] Object identified as an AGN on the basis of both rest-UV (LRIS-B) and rest-optical (MOSFIRE) spectra.

[A2] Object identified as an AGN on the basis of near-IR (MOSFIRE) spectra.

[1] Objects with optical (rest-UV) spectra obtained using Keck/LRIS-B; galaxies whose LRIS-B spectra yielded spectroscopic redshifts are marked "1", while "1a" denotes objects that were observed in the rest-UV but did not yield a secure spectroscopic redshift.

References to other spectroscopic/photometric measurements: (2) Erb et al. (2003) (3) Shapley et al. (2005b) (4) Erb et al. (2006c) (5) Law et al. (2009) (6) Steidel et al. (2010) (7) Förster Schreiber et al. (2009) (8) Erb et al. (2010) (9) Law et al. (2012) (10) Shapley et al. (2004)

TABLE 3
KBSS-MOSFIRE GALAXIES WITH [NII]/Hα AND STELLAR MASS MEASUREMENTS

Name	z_{neb}	log M_* $M_\odot$	log([NII]/Hα)	12+log(O/H)[b] (N2 PP04)	Notes
Q0100-BX53	2.0009	9.87	$-1.19^{+0.17}_{-0.12}$	$8.22^{+0.10}_{-0.07}$	1a
Q0100-MD37	2.3899	11.18	$-0.39^{+0.08}_{-0.07}$	$8.68^{+0.05}_{-0.04}$	
Q0105-BX52	1.9717	10.64	$-0.50^{+0.09}_{-0.07}$	$8.62^{+0.05}_{-0.04}$	1
Q0105-BX93	2.0301	10.06	$-0.98^{+0.05}_{-0.04}$	$8.34^{+0.03}_{-0.02}$	1
Q0105-BX95	2.0304	10.38	$-0.72^{+0.04}_{-0.03}$	$8.49^{+0.02}_{-0.02}$	1,5
Q0142-BX116	2.1131	10.31	$-0.19^{+0.13}_{-0.10}$	$8.79^{+0.08}_{-0.06}$	1
Q0142-BX119	2.2237	10.84	$-0.68^{+0.11}_{-0.09}$	$8.51^{+0.06}_{-0.05}$	1
Q0142-BX120	2.2241	9.96	$-1.05^{+0.12}_{-0.10}$	$8.30^{+0.07}_{-0.05}$	
Q0142-BX241	2.2843	9.82	$-0.82^{+0.08}_{-0.07}$	$8.43^{+0.04}_{-0.04}$	1
Q0142-BX248	2.4980	9.64	$-0.76^{+0.19}_{-0.13}$	$8.47^{+0.11}_{-0.07}$	1
Q0142-BX61	2.0702	9.62	$-0.53^{+0.10}_{-0.08}$	$8.60^{+0.06}_{-0.05}$	1
Q0821-RK5	2.1831	11.80	$+0.02^{+0.05}_{-0.04}$	$8.91^{+0.03}_{-0.03}$	A2
Q1009-BX93	2.0450	9.44	$-0.74^{+0.19}_{-0.13}$	$8.48^{+0.11}_{-0.07}$	
Q1442-BX159	1.9957	9.97	$-0.76^{+0.08}_{-0.07}$	$8.47^{+0.05}_{-0.04}$	1
Q1442-BX317	2.0273	9.71	$-1.18^{+0.11}_{-0.09}$	$8.23^{+0.07}_{-0.05}$	1a
Q1549-BX42	2.2194	9.08	$-0.57^{+0.12}_{-0.09}$	$8.57^{+0.07}_{-0.05}$	1
Q1549-BX94	2.0074	10.49	$-0.72^{+0.10}_{-0.08}$	$8.49^{+0.06}_{-0.05}$	1
Q1603-BX127	2.5521	9.59	$-0.83^{+0.18}_{-0.13}$	$8.43^{+0.10}_{-0.07}$	1
Q1623-BX410	2.5395	10.49	$-0.57^{+0.11}_{-0.09}$	$8.57^{+0.06}_{-0.05}$	1
Q1700-BX475	2.4027	9.86	$-0.96^{+0.14}_{-0.11}$	$8.35^{+0.08}_{-0.06}$	1a
Q1700-BX535	2.6366	9.69	$-0.65^{+0.15}_{-0.11}$	$8.53^{+0.08}_{-0.06}$	1a,3
Q1700-BX684	2.2922	8.89	$-0.69^{+0.11}_{-0.09}$	$8.51^{+0.06}_{-0.05}$	
Q1700-BX801	2.0380	10.22	$-0.44^{+0.13}_{-0.10}$	$8.65^{+0.08}_{-0.06}$	1
Q1700-BX810	2.2923	10.08	$-0.87^{+0.13}_{-0.10}$	$8.41^{+0.08}_{-0.06}$	1,3
Q1700-BX909	2.2934	10.65	$-0.92^{+0.10}_{-0.08}$	$8.38^{+0.06}_{-0.05}$	1,6
Q1700-BX939	2.2971	9.75	$-0.97^{+0.11}_{-0.09}$	$8.35^{+0.06}_{-0.05}$	1,3
Q2206-BX102	2.2099	11.19	$-0.29^{+0.03}_{-0.03}$	$8.74^{+0.02}_{-0.02}$	1,6
Q2206-BX166	1.9742	9.90	$-0.95^{+0.16}_{-0.11}$	$8.36^{+0.09}_{-0.07}$	1
Q2206-BX169	2.0960	10.88	$-0.56^{+0.09}_{-0.07}$	$8.58^{+0.05}_{-0.04}$	
Q2206-BX68	2.0971	10.49	$-0.84^{+0.09}_{-0.07}$	$8.42^{+0.05}_{-0.04}$	
Q2343-BX390	2.2311	9.90	$-0.89^{+0.07}_{-0.06}$	$8.39^{+0.04}_{-0.04}$	1,4,6
Q2343-D25	2.1865	9.50	$-0.89^{+0.12}_{-0.09}$	$8.39^{+0.07}_{-0.05}$	1

[a] Error bars are 1σ based on measurement uncertainties only.
[b] Oxygen abundance assuming the "N2" calibration of PP04.
[A1] Object identified as an AGN on the basis of both rest-UV (LRIS-B) and rest-optical (MOSFIRE) spectra.
[A2] Object identified as an AGN on the basis of near-IR (MOSFIRE) spectra.
[1] Objects with optical (rest-UV) spectra obtained using Keck/LRIS-B; galaxies whose LRIS-B spectra yielded spectroscopic redshifts are marked "1", while "1a" denotes objects that were observed in the rest-UV but did not yield a secure spectroscopic redshift.
References to other spectroscopic/photometric measurements: (2) Erb et al. (2003) (3) Shapley et al. (2005b) (4) Erb et al. (2006c) (5) Law et al. (2009) (6) Steidel et al. (2010) (7) Förster Schreiber et al. (2009) (8) Erb et al. (2010) (9) Law et al. (2012) (10) Shapley et al. (2004)

TABLE 4
PROPERTIES OF "EXTREME" KBSS-MOSFIRE GALAXIES

Object	[OII] Ratio[a]	n_e[b]	[OIII] Ratio[c]	Hα/Hβ	T_e(K)	O32[d]	$[OIII]_{tot}/H\beta$ [e]	12+log(O/H)[f]
Q0207-BX74[g]	1.68 ± 0.11	1575^{+300}_{-200}	0.037 ± 0.005	3.46 ± 0.25	14300 ± 400	8.23 ± 0.41	10.06 ± 0.45	8.00 ± 0.05
Q2343-BX418	1.13 ± 0.05	580^{+80}_{-70}	0.023 ± 0.003	2.81 ± 0.20	12830 ± 500	9.66 ± 0.38	8.67 ± 0.42	8.08 ± 0.05
Q2343-BX660	0.93 ± 0.04	300^{+40}_{-40}	0.022 ± 0.004	2.77 ± 0.20	12650 ± 500	10.98 ± 0.50	9.58 ± 0.45	8.13 ± 0.06

[a] Intensity ratio [OII]λ3726/[OII]λ3729.
[b] Electron density in cm^{-3} determined from the intensity ratio of the [OII] doublet.
[c] Measured intensity ratio OIII](λ1661 + λ1666)/[OIII]λ5008.
[d] Ratio [OIII](λ4960 + λ5008)/[OII](λ3726 + λ3729).
[e] Ratio of [OIII](λ4960 + λ5008)/Hβ.
[f] Inferred oxygen abundance from the direct T_e method.
[g] Line intensity ratios (other than Hα/Hβ) corrected for nebular extinction assuming $E(B-V)_{neb} = 0.18$ and the Cardelli et al. (1989) attenuation relation.

TABLE 5
$z \sim 2.3$ BINNED MASS-METALLICITY RELATION (N2)

Bin Range $\log(M_*/M_\odot)$	Median $\log(M_*/M_\odot)$	N_{gal}	$12+\log(O/H)_{N2}$[a] (Mean)	$12+\log(O/H)_{N2}$[b] (Median)	$12+\log(O/H)_{N2}$[c] (Stack)
8.60 – 9.00	8.87	8	8.20 ± 0.10	8.21	$8.13^{+0.05}_{-0.06}$
9.00 – 9.50	9.34	35	8.23 ± 0.03	8.20	$8.25^{+0.03}_{-0.07}$
9.50 – 9.80	9.69	48	8.31 ± 0.03	8.33	$8.30^{+0.03}_{-0.02}$
9.80 – 10.00	9.87	34	8.35 ± 0.02	8.35	$8.36^{+0.04}_{-0.03}$
10.00 – 10.25	10.11	39	8.38 ± 0.02	8.39	$8.42^{+0.02}_{-0.04}$
10.25 – 10.50	10.37	32	8.47 ± 0.03	8.49	$8.49^{+0.03}_{-0.04}$
10.50 – 11.00	10.66	39	8.51 ± 0.03	8.54	$8.53^{+0.03}_{-0.02}$
11.00 – 11.60	11.19	8	8.65 ± 0.02	8.67	$8.67^{+0.09}_{-0.09}$

[a] Bi-weight mean of individual measurements in bins of M_*, determined using the PP04 N2 calibration; y-axis error bars are uncertainties in the weighted mean within each bin, while x-axis error bars reflect the range of M_* within each bin.
[b] Median inferred N2-based oxygen abundance in bin.
[c] Oxygen abundance inferred using PP04 N2, from spectral stacks within each bin of M_*; error bars reflect both formal measurement uncertainties and sample variance within each mass bin.

TABLE 6
$z \sim 2.3$ BINNED MASS-METALLICITY RELATION (O3N2)

Bin Range $\log(M_*/M_\odot)$	Median $\log(M_*/M_\odot)$	N_{gal}	$12+\log(O/H)_{O3N2}$[a] (Mean)	$12+\log(O/H)_{O3N2}$[b] (Median)	$12+\log(O/H)_{O3N2}$[c] (Stack)
8.60 – 9.00	8.87	8	8.10 ± 0.08	8.09	8.06 ± 0.03
9.00 – 9.50	9.34	35	8.14 ± 0.02	8.13	8.16 ± 0.02
9.50 – 9.80	9.69	48	8.21 ± 0.02	8.23	8.20 ± 0.01
9.80 – 10.00	9.87	34	8.23 ± 0.02	8.24	8.21 ± 0.01
10.00 – 10.25	10.11	39	8.27 ± 0.02	8.27	8.28 ± 0.01
10.25 – 10.50	10.37	32	8.35 ± 0.02	8.37	8.35 ± 0.01
10.50 – 11.00	10.66	39	8.37 ± 0.02	8.42	8.39 ± 0.01
11.00 – 11.60	11.19	8	8.52 ± 0.02	8.52	8.55 ± 0.03

[a] Bi-weight mean of individual measurements in bins of M_*, determined using the PP04 O3N2 calibration; y-axis error bars are uncertainties in the weighted mean within each bin, with x-axis error bars reflecting the range of M_* within each bin.
[b] Median inferred O3N2-based oxygen abundance in bin.
[c] Oxygen abundance inferred using PP04 O3N2, from spectral stacks within each bin of M_*; y-axis error bars reflect formal measurement uncertainties only.